

## SIMULATIONS OF SUPERCOLLIDER PHYSICS

**K.D. Lane<sup>1</sup>, F.E. Paige<sup>2</sup>, T. Skwarnicki<sup>3</sup>, and W.J. Womersley<sup>4</sup>**

<sup>1</sup> Physics Department, Boston University, Boston, MA 02215

<sup>2</sup> Physics Department, Brookhaven National Laboratory, Upton, NY 11973

<sup>3</sup> Physics Department, Southern Methodist University, Dallas, TX 75275

<sup>4</sup> Fermi National Accelerator Laboratory, Batavia, IL 60510

### ABSTRACT

The Standard Model of particle physics makes it possible to simulate complete events for physics signatures and their backgrounds in high energy collisions. Knowledge of how the produced particles interact with the materials in a detector makes it possible to simulate the response of any particular detector design to these events and so determine whether the detector could observe the signal. The combination of these techniques has played an important role in the design of new detectors, particularly those for hadron supercolliders where the high rates and small signal cross sections make the experiments very difficult. The technique is reviewed here and illustrated using the simulations of the GEM detector proposed for the Superconducting Super Collider. Although the simulations and results described here are somewhat detector-specific, we believe that they can serve as a useful model for this component of detector design for future hadron supercolliders.

## 1. INTRODUCTION

The “Standard Model” of particle physics describes strong, electromagnetic, and weak interactions in terms of an  $SU(3) \otimes SU(2) \otimes U(1)$  gauge theory. The theoretical elements of the model have been in place for more than 20 years.<sup>1,2</sup> Over that period a series of experimental results — including the discoveries of charm,<sup>3</sup> of the  $\tau$ -lepton and the  $b$  quark,<sup>4</sup> and of the predicted  $W^\pm$  and  $Z^0$  bosons<sup>5</sup> — have provided increasing evidence of the correctness of the Standard Model at present energy scales. More recently, the Standard Model has withstood extremely stringent quantitative experimental tests.<sup>6</sup> Thus it is now accepted that it provides a good description of particle physics down to the shortest distances yet probed, about  $10^{-16}$  cm.

In the Standard Model the basic constituents of matter are spin- $\frac{1}{2}$  quarks and leptons. There are six types or “flavors” of each. Under the  $SU(2) \otimes U(1)$  group of electroweak interactions, the left-handed fields are in three quark and lepton doublets; the right-handed ones are in singlets:

$$\text{Leptons : } \begin{pmatrix} \nu_e \\ e \end{pmatrix} \quad \begin{pmatrix} \nu_\mu \\ \mu \end{pmatrix} \quad \begin{pmatrix} \nu_\tau \\ \tau \end{pmatrix} \quad (1.1a)$$

$$\text{Quarks : } \begin{pmatrix} u \\ d' \end{pmatrix} \quad \begin{pmatrix} c \\ s' \end{pmatrix} \quad \begin{pmatrix} t \\ b' \end{pmatrix} \quad (1.1b)$$

Under the  $SU(3)$  group of strong interactions, which for historical reasons is known as color, the quarks are triplets and the leptons are singlets. The quarks and leptons can also be organized into three generations identical except for mass. There is mixing between the generations of quarks; the primed lower elements in Eq. (1.1b) denote linear combinations of the mass eigenstates. All the fermions definitely have been found except for the top quark and the tau-neutrino. Direct evidence for the top quark with mass  $m_t = 174 \pm 10^{+13}_{-12}$  GeV has recently been reported.<sup>7</sup> There is strong indirect evidence for the tau-neutrino.<sup>8,9</sup> If the number of quark-lepton generations is equal to the number  $N_\nu$  of light neutrinos, then there are no more than these three. The evidence for this comes from precision measurements of the  $Z^0$  at LEP, which imply  $N_\nu = 2.99 \pm 0.04$  in the Standard Model.<sup>9</sup>

The interactions of the quarks and leptons are invariant under  $SU(3) \otimes SU(2) \otimes U(1)$  locally at each point in space-time. The requirement of local invariance implies that there is one spin-one gauge boson for each generator of the symmetry group, and it restricts their couplings so that the theory is renormalizable. This means that cross sections do not grow more rapidly than allowed by unitarity and that the form of the interactions is insensitive to possible physics at much higher mass scales. These gauge bosons are responsible for all known interactions except gravity, for which there is no fully satisfactory quantum theory. The eight generators of the  $SU(3)$  color group correspond to the eight massless gluons of Quantum Chromodynamics (QCD) that are responsible for strong interactions. Gauge invariance requires that these interact. These self-interactions produce a potential energy

which grows linearly with distance between isolated quarks or gluons, which are therefore permanently confined into the observed hadrons such as the proton. At short distances — large energies and momentum transfers — the same interactions make the QCD coupling weak, so that perturbation theory can be used to describe the production of heavy particles or large- $p_T$  interactions in hadronic collisions. Because a gauge theory restricts the form of the couplings and because calculations can be done in perturbation theory, the Standard Model can be used to predict cross sections even for new physics (provided, of course, that a model exists for the couplings of the new physics to standard model degrees of freedom).

The remaining four generators of  $SU(2) \otimes U(1)$  correspond to the massless photon and the massive  $W^\pm$  and  $Z^0$  bosons responsible for electroweak interactions. If a gauge symmetry is unbroken, then the gauge bosons and fermions associated with it must be massless. It is possible, however, to introduce new interactions that break the symmetry “spontaneously” while preserving the good high-energy behavior of the gauge theory. This is known as the “Higgs mechanism”.<sup>10</sup> In the Standard Model, both the  $W^\pm$  and  $Z^0$  bosons and the fermions get their masses from an elementary scalar field, which is a doublet under  $SU(2)$  and which acquires a vacuum expectation value, thus breaking the symmetry.

While there is strong experimental evidence supporting the gauge-theoretic part of the Standard Model, there is as yet no evidence for or against the Higgs mechanism for electroweak symmetry breaking. Nor is there data to indicate the mechanism by which finite and unequal fermion masses are generated (flavor symmetry breaking). Understanding how these masses are produced is the central problem in particle physics. Several scenarios have been proposed for electroweak and flavor symmetry breaking:<sup>11</sup>

- Standard Higgs models, containing one or more elementary Higgs boson multiplets. These are generally complex weak doublets. The minimal model has one doublet, with a single neutral boson  $H^0$ .
- Supersymmetry. In the minimal supersymmetric standard model there are two Higgs doublets, and every known particle has a superpartner.
- Models of dynamical electroweak and flavor symmetry breaking. The most studied proposal is technicolor-plus-extended-technicolor, with one doublet or one family of technifermions.
- Composite models, in which quarks and leptons are built of more fundamental constituents.

None of these proposals is fully satisfactory. In elementary Higgs boson models, whether supersymmetric or not, there is no plausible natural explanation of why electroweak symmetry breaking occurs and why it has the observed scale. In non-supersymmetric models, the Higgs boson’s mass,  $M_H$ , and its vacuum expectation value,  $v$ , are unstable against radiative corrections. There is no natural reason why these two

parameters should be very much less than the energy scale at which the essential physics changes, e.g., a unification scale or the Planck scale.<sup>12</sup> This instability does not arise in supersymmetric models, which is the motivation for supersymmetry at the electroweak scale.<sup>13,14</sup> Furthermore, elementary Higgs boson models are known to be “trivial”, i.e., they cannot make sense as interacting field theories with the cutoff taken to infinity.<sup>15</sup> This means that they must be regarded as effective theories, meaningful only below some cutoff  $\Lambda$ . Obviously,  $\Lambda$  must be somewhat greater than  $M_H$  for the effective theory to make sense. For a modest separation of these energies,  $M_H < \text{few} \times \Lambda$ , both perturbative and lattice gauge calculations give  $M_H \lesssim 650 \text{ GeV}$  in the minimal one-doublet model.<sup>16</sup> Finally, elementary Higgs models provide no clue to the meaning of flavor symmetry and the origin of its breaking. The flavor-symmetry breaking Yukawa couplings of the Higgs boson to fermions are arbitrary free parameters.

Despite these apparent problems, the standard Higgs boson,  $H^0$ , charged Higgses,  $H^\pm$ , and the supersymmetric partners of all the known particles may exist and must be sought. However, if something like the standard  $H^0$  is found and is heavier than about 700 GeV, experiments must have the capacity to discover the additional, unspecified new physics that surely exists in the same energy region, of order 1 TeV. One of the basic considerations driving the high collision energy of the SSC was the possibility that such physics exists.

Dynamical theories of electroweak and flavor symmetries — technicolor and extended technicolor — address these shortcomings of the elementary Higgs boson models.<sup>17</sup> However, they do so at the price of introducing flavor-changing neutral currents that are too large, and pseudo-Goldstone bosons (technipions) that are too light.<sup>18</sup> Further, it is difficult to build realistic models with QCD-like dynamics that are consistent with the precision tests of the electroweak interactions. These difficulties have been mitigated, but only by invoking a new form of strong technicolor dynamics.<sup>19,20</sup> Realistic models of composite quarks and leptons are similarly difficult to construct.<sup>21</sup> While no compelling models of dynamical electroweak and flavor symmetry breaking exist, there are nevertheless model-independent phenomenological programs for searching for them.<sup>11</sup>

While the origin of electroweak symmetry breaking is unknown, the mass scale for the new physics responsible for it is set by the vacuum expectation value of the Standard Model Higgs boson:

$$v = 2^{-\frac{1}{4}} G_F^{-\frac{1}{2}} = 246 \text{ GeV} .$$

The cross section for *any* new physics at this scale is set by dimensional analysis and coupling strengths to be  $\sigma \sim 1 \text{ nb} - 1 \text{ fb}$ . So long as the nature of this new physics remains unknown, the most promising way by far to explore this mass and cross section scale is with a  $pp$  (or  $p\bar{p}$ ) supercollider. That is because such a machine functions as a collider of broad-band beams of quarks and gluons (thus allowing coupling to both color and electroweak quantum numbers) and because these beams have the highest energy and

luminosity technically feasible today. Clearly, it would have been easier to carry out the high-mass searches at higher center of mass energy and a luminosity of  $\mathcal{L} \sim 10^{33} \text{ cm}^{-2} \text{ s}^{-1}$  rather than  $10^{34} \text{ cm}^{-2} \text{ s}^{-1}$ . Nevertheless, for the foreseeable future, the capabilities of the CERN Large Hadron Collider (LHC),  $\sqrt{s} = 14 \text{ TeV}$  and  $\mathcal{L} = 10^{34} \text{ cm}^{-2} \text{ s}^{-1}$ , make it the best instrument for discovering the origin of electroweak symmetry breaking.

Hadron supercolliders such as the SSC or LHC present a difficult experimental problem: the interesting cross sections are very small compared to the total cross section of order 100 mb and small even compared to the dijet cross section at a comparable mass. Thus, careful study is needed to determine whether a given experimental design can detect the signatures of models for new physics. Because these signatures always manifest themselves as quarks and gluons (jets), charged leptons and neutrinos (missing transverse energy,  $\cancel{E}_T$ ), the Standard Model allows simulation of events both for the new physics and for its backgrounds in a reliable and predictive way. Given a detector design and known facts about particle-matter interactions, the response of the detector to these events can also be simulated. Finally, the simulated data can be reconstructed and analyzed just as for a real experiment to determine whether one could observe a signal.

These in-depth simulations are necessitated by the long lead times and large amounts of money involved in constructing a supercollider detector. They have been made possible by the convergence of a reliable theoretical framework (the Standard Model) with rapid increases in available computing power. The simulations are an essential component of the design process, providing feedback on the design's strengths and weaknesses. In this way, the simulations have played and continue to play an important role in the design of detectors for the SSC and LHC.

This article reviews the simulations carried out by the GEM (Gammas, Electrons, and Muons) Collaboration for its detector<sup>22</sup> at the SSC. Section 2 describes the tools available for simulation of interactions and of the behavior of the resulting particles in a detector. Section 3 briefly reviews the design proposed for the GEM detector at the time of Technical Review. It is essential to have a detailed engineering design to obtain realistic results, and the details of results presented here are, strictly speaking, valid principally for this design. However, any well-developed design is likely to have comparable strengths and problems, so the methods used for GEM and the results obtained should be more generally useful. Section 4 describes the tools developed for the simulation of the GEM detector. The principal development was a fast all-detector parameterization, called **gemfast**, that allowed simulation of very large numbers of events in a manageable amount of time. This was supplemented by the most detailed possible simulations of the muon system and calorimetry in those cases that the fast simulation was insufficient to model important details and where the importance of the physics to GEM's design was believed to warrant the considerable extra effort. In section 5, the bulk of this article, we describe the results obtained for a variety of representative processes. These were chosen to impose stringent tests on *all*

areas of the GEM detector's design as well as for their intrinsic physics interest. Finally, Section 6 summarizes the results and conclusions. In publishing this document, it is our hope that others will see it as describing a useful model of detector simulation. We believe that that this model can be improved. We are also convinced of the validity of the simulation philosophy that culminated in **gemfast**. This gave GEM the capacity to simulate rapidly a very wide variety of physics and background processes and to use the results of these simulations to provide input for crucial design improvements. Without **gemfast**, we would have had to compromise either the breadth or the plausibility of our studies.

## 2. SIMULATION TOOLS IN HIGH ENERGY PHYSICS

Since the Standard Model is a gauge theory, the coupling of any new physics to known particles is determined by the  $SU(3) \otimes SU(2) \otimes U(1)$  representations of the new particles. Furthermore, since the  $SU(3)$  coupling becomes small at large momentum transfer and the  $SU(2)$  and  $U(1)$  couplings are intrinsically small, the cross sections for the production of new particles can be calculated in perturbation theory provided that the new physics does not involve nonperturbative dynamics. Even if the new dynamics is nonperturbative, its coupling to ordinary matter remains perturbative, and useful predictions can still be made, e.g., for strong  $WW$  scattering.<sup>23</sup> All the Standard Model background cross sections can likewise be calculated using perturbation theory.

For testing a detector design, it is not sufficient to calculate cross sections; it is necessary to generate complete events; event generators are briefly reviewed in Section 2.1 below. It is also necessary to simulate the interactions of each of the particles from these events with the detector. One of the most generally useful programs for doing this is GEANT,<sup>24</sup> which contains tools for describing the geometry of the detector and for propagating particles through it taking into account all the possible interactions. CALOR89,<sup>25</sup> is less general but contains a better description of low-energy neutrons and so is better suited to precision calculations of the response of hadron calorimeters. These simulation tools are reviewed in Section 2.2 below.

While GEANT and CALOR89 are very powerful, they are too slow to simulate the large number of events needed to determine the backgrounds for new physics signatures in hadronic collisions. Hence it is necessary to construct fast, parameterized simulations based on GEANT or CALOR89 results for single particles and on test beam data. A sophisticated parameterized simulation of the GEM detector, **gemfast**, is the basis of most of the physics results herein. It is described in Section 4 below.

### 2.1. Review of Event Generation

HERWIG,<sup>26</sup> ISAJET,<sup>27</sup> and PYTHIA<sup>28</sup> are all programs widely used in particle physics to generate complete events for a variety of processes. While these programs differ in many important details, they share a common general approach, which is outlined here.

The first step in producing a complete event is to generate an initial hard scattering process using its perturbative QCD or electroweak cross section. Because the QCD effective coupling  $\alpha_s(Q^2)$  becomes small at large momentum transfer  $Q^2$ , the cross section  $\hat{\sigma}$  for any hard process involving quarks and gluons can be calculated in perturbation theory. Then the  $pp$  cross section is given by the convolution of  $\hat{\sigma}$  with the parton distributions  $f_i(x, Q^2)$ :

$$\sigma = \int dx_1 dx_2 \hat{\sigma}(\hat{s}, Q^2) \delta\left(x_1 x_2 - \frac{\hat{s}}{s}\right) f_i(x_1, Q^2) f_j(x_2, Q^2) . \quad (2.1)$$

Beyond the leading order in  $\alpha_s$ ,  $\hat{\sigma}$  in general contains infrared and collinear singularities. For inclusive cross sections, the infrared singularities cancel between real and virtual

graphs, and the collinear singularities can be absorbed consistently into the parton distributions  $f_i(x, Q^2)$ , producing their  $Q^2$  dependence. To lowest order, however,  $\hat{\sigma}$  is free of any singularities, so Eq. (2.1) can be used to generate an exclusive process using standard Monte Carlo techniques. That is, the program selects the four-vectors for the initial hard scattering.

While Eq. (2.1) is a good approximation for sufficiently inclusive cross sections, it is a poor approximation for the structure of events. The hard scattering process represented by  $\hat{\sigma}$  involves external quarks and gluons at least in the initial state and generally in the final state as well. These are massless and carry color charge, so they necessarily radiate gluons. Since the coupling in QCD is dimensionless, this radiation occurs on all  $Q^2$  scales from that of the initial hard scattering down to the confinement scale,  $\mathcal{O}(1 \text{ GeV}^2)$ . In particular, a massless quark or gluon can radiate a collinear massless gluon while conserving energy and momentum, leading to a so-called mass or collinear singularity. Because of these singularities, the higher order corrections are of order  $\alpha_s(Q^2) \log Q^2$ , and they cannot be neglected.

Fortunately, the collinear singularities take a simple form. Each additional radiation in which an external parton  $i$  produces  $j$  and  $k$  introduces into the cross section a factor

$$\frac{\alpha_s}{2\pi p_i^2} P_{i \rightarrow jk}(z) \quad (2.2)$$

where  $z = p_j/p_i$  is the momentum fraction carried by  $j$  and  $P_{i \rightarrow jk}$  is one of the well-known Altarelli-Parisi functions.<sup>29</sup> The dominant contribution comes from  $p_{j,k}^2 \ll p_i^2 \ll Q^2$ , so each radiation is approximately independent. Because of this and because the cross sections and not the amplitudes factorize, the quantum mechanical radiation in the collinear limit can be treated as a classical Markov branching process. The radiation of soft gluons also factorizes, just as it does for QED. This makes it possible to write a Monte Carlo algorithm, known as the branching approximation,<sup>26,27,28</sup> that correctly generates all the  $\alpha_s(Q^2) \log Q^2$  corrections to all orders in QCD perturbation theory. Each branching leads to partons with smaller  $p_i^2$ . Since the Monte Carlo algorithm uses exact, non-collinear kinematics, it also generates a fair approximation to non-collinear radiation, i.e. to multijet final states.

For sufficiently small  $p_i^2$  perturbation theory becomes invalid, and one must resort to a model to convert partons into hadrons. Both ISAJET and PYTHIA use fragmentation models based on low-energy data for this. HERWIG carries perturbation theory down to  $p_i^2 = \mathcal{O}(1 \text{ GeV}^2)$  and uses mainly two-body phase space for the final hadronization. It is also necessary to model the hadronization of the spectator partons, which carry most of the total energy; there is no reliable theory for this. Fortunately, while the hadronization model is important for the details, perturbation theory controls the main features.

An alternative to the branching approximation is to use explicit higher-order matrix elements. This approach produces a better approximation to cross sections for events

with several distinct jets, but it is difficult to combine with parton showers to produce realistic events without double counting. VECBOS<sup>30</sup> contains the exact tree-level cross sections for  $W + n$  jets with  $n \leq 4$ , and has played an important role in searches for the top quark. PAPANENO<sup>31</sup> contains a wide range of processes and has been used in some of the analyses presented here.

## 2.2. Review of GEANT and CALOR89

GEANT is a system of detector-description and simulation tools written largely at CERN. The first version, written in 1974, was a bare framework which emphasized tracking of a few particles per event through a relatively simple detector. GEANT has been continuously developed since then to handle much more complex detector systems, many hundreds of particles per interaction, and greater detail in the physics simulated. Because of its flexibility, good support on many hardware platforms, and years of verification against data, GEANT has become a *de facto* standard within high energy physics and is used very extensively.

GEANT performs the following functions:

- **Define particle and material parameters.** GEANT has internal databases of particle masses and lifetimes, properties of common materials, and interaction cross sections. The user is able to define additional materials, and create mixtures or compounds.
- **Geometry definition.** The user must create a geometrical model of the detector. GEANT will then handle the tracking of particles through this model and their interactions within it. GEANT 3.15 provides a palette of 14 standard shapes for the user which can be sized, positioned and rotated as desired. The detector model is a hierarchical tree in which each volume is contained within a ‘mother’, and each ‘mother’ contains one or more ‘daughters.’
- **Compute physics processes.** GEANT accepts lists of particles and vertices produced by event generators. It contains routines to handle the decays of unstable particles, and the interactions of particles with the detector. The physics package computes the probability of occurrence of a process by sampling the total cross section and generates the final state after interaction. It also handles continuous or quasi-continuous processes such as energy loss. The processes currently implemented for electrons and photons are: multiple Coulomb scattering, ionization and delta ray production, bremsstrahlung, positron annihilation,  $e^+e^-$  pair production, Compton scattering, photoelectric effect, photofission of heavy elements, and Rayleigh scattering. For muons, decays in flight, multiple scattering, ionization and delta ray production, bremsstrahlung, direct pair production and nuclear interactions are implemented. For hadrons, decays in flight, multiple scattering, ionization and delta ray production, and hadronic interactions are included. The hadronic interactions are handled

by parameterizations of experimental data incorporated in the packages GHEISHA,<sup>32</sup> HADRIN/NUCRIN<sup>33</sup> and FLUKA.<sup>34</sup>

- **Track particles through the detector.** Particles from the primary interaction, and those generated within the detector, are tracked through the detector model. Tracking proceeds in steps; during each step, the particle may decay or interact; otherwise, it loses energy through ionization and continues to the next step. Particles whose kinetic energy falls below a cutoff value are stopped and their remaining energy dumped.
- **Simulation of detector response.** The detector response is modeled in two stages. Firstly the particles are tracked through the sensitive detector elements; then, after the whole event has been tracked, digitization routines (provided by the user) are called to model the response of the detector to the particles. This two-step process enables nonlinear effects (such as detectors able to respond only to the passage of one particle) to be properly modeled.
- **Drawing.** GEANT includes a drawing package to produce graphical output showing the detector model and the trajectories of particles through it. Tools are provided for the user to add markers for the locations of energy loss, hit detector elements, etc. The drawing package can also produce graphical representations of the hierarchical tree of volumes or of the internal data structures of the program.

Although GEANT is indispensable for general detector simulation, we have also made use of the CALOR89<sup>25</sup> package for calorimeter simulations. We have used CALOR89 both directly, and through an interface with GEANT.<sup>35</sup> CALOR89 provides a more detailed low-energy treatment of hadronic processes, especially neutron transport, which is of interest in the prediction of hadronic calorimeter resolutions. It uses HETC with FLUKA<sup>34</sup> for general hadronic transport, MORSE<sup>36</sup> for neutrons with energy below 20 MeV, and EGS<sup>37</sup> for electromagnetic particles. CALOR89 contains its own geometry, tracking and physics packages similar in concept to those of GEANT.

### 3. THE GEM DETECTOR

The GEM collaboration was formed in 1991 to develop a major detector for the SSC. The physics objectives of GEM reflected the motivation for the SSC itself: to study high transverse momentum physics — exemplified by the search for Higgs bosons — and to search for new physics beyond the Standard Model. The GEM detector design was presented in a Technical Design Report (TDR),<sup>22</sup> and the simulations described in this paper are based on that design (See Figure 1). The detector was designed as a general purpose device emphasizing clean identification and high resolution measurement of gammas, electrons, and muons, hence the name, GEM. High priority also was given in the design to accurate measurement of jets and missing transverse energy. The architecture and the detector technologies chosen were intended to provide good performance even at the highest luminosities that were contemplated for the SSC. The design of the GEM detector was based on the following principles:

- Very precise electromagnetic calorimetry without a magnet coil in front of it. Together with the redundant pointing capabilities of the EM calorimeter and central tracker, this provides the best measurements of photon and electron energies and allows the reconstruction of the masses of narrow states with very high resolution.
- A precise muon spectrometer in a large superconducting solenoidal magnet, allowing measurement of the momenta of high energy muons over a large solid angle with a minimum of multiple scattering. The muon system is situated in a quiet environment, shielded by the thick calorimeter. Muon measurement does not rely on central tracking, thereby providing a robust stand-alone system for operation at the highest luminosities.
- Hermetic hadronic calorimetry for the measurement of jets and the reconstruction of missing energy.
- Central tracking in a magnetic field with sufficiently low occupancy to operate reliably at the highest luminosities anticipated at the SSC ( $10^{34} \text{ cm}^{-2} \text{ s}^{-1}$ ). The central tracker radius is 0.9 m, allowing for a compact calorimeter and a large muon tracking volume. It was assumed in simulations that the inner silicon tracking layers were removed at  $\mathcal{L} = 10^{34} \text{ cm}^{-2} \text{ s}^{-1}$ .

The performance specifications of the detector are given in Table 1. The reach of the GEM design for physics signals that were of of major interest to the SSC is summarized in Figure 2.

#### 3.1. Detector Design

The detailed optimization of the design was determined by the physics requirements, the practical ability to meet the necessary performance specifications, and cost/schedule constraints. Attention was also paid to detector integration issues such as radiation shielding and the interaction between the beamline and the inner radius of the detector. It was

Scanned detector figure is too large for electronic distribution.

FIG. 1: Perspective view of the GEM detector.

also intended that GEM should be complementary to the SDC detector, which used a large tracker; GEM emphasized calorimetric measurement of gammas and electrons, a precise and robust muon system, and unique capabilities at high luminosity.

Detailed descriptions of the detector subsystems, including technical features, implementation and integration issues, and studies of expected performance are given in the Technical Design Report.<sup>22</sup> We describe briefly some of the key features of each major subsystem below.

### 3.1.1. Magnet

A very large superconducting solenoid surrounded the detector elements, with a nominal field of 0.8 T, an inner diameter of 18 m, and a length of 31 m. The magnet provided a nearly uniform axial field in the region of the central tracker, allowing measurements of the momenta and signs of charged particles and helping with electron identification. In the volume of detector outside the calorimeters, the magnet provided a 0.8 T field for muon momentum measurements. The coil was in two halves, one on each side of the central detector support (which carried the calorimeter and central tracker). In the forward region, conical iron poles were employed to shape the field. These introduced a radial component to the forward field, improving the resolution of the muon system in the forward direction.

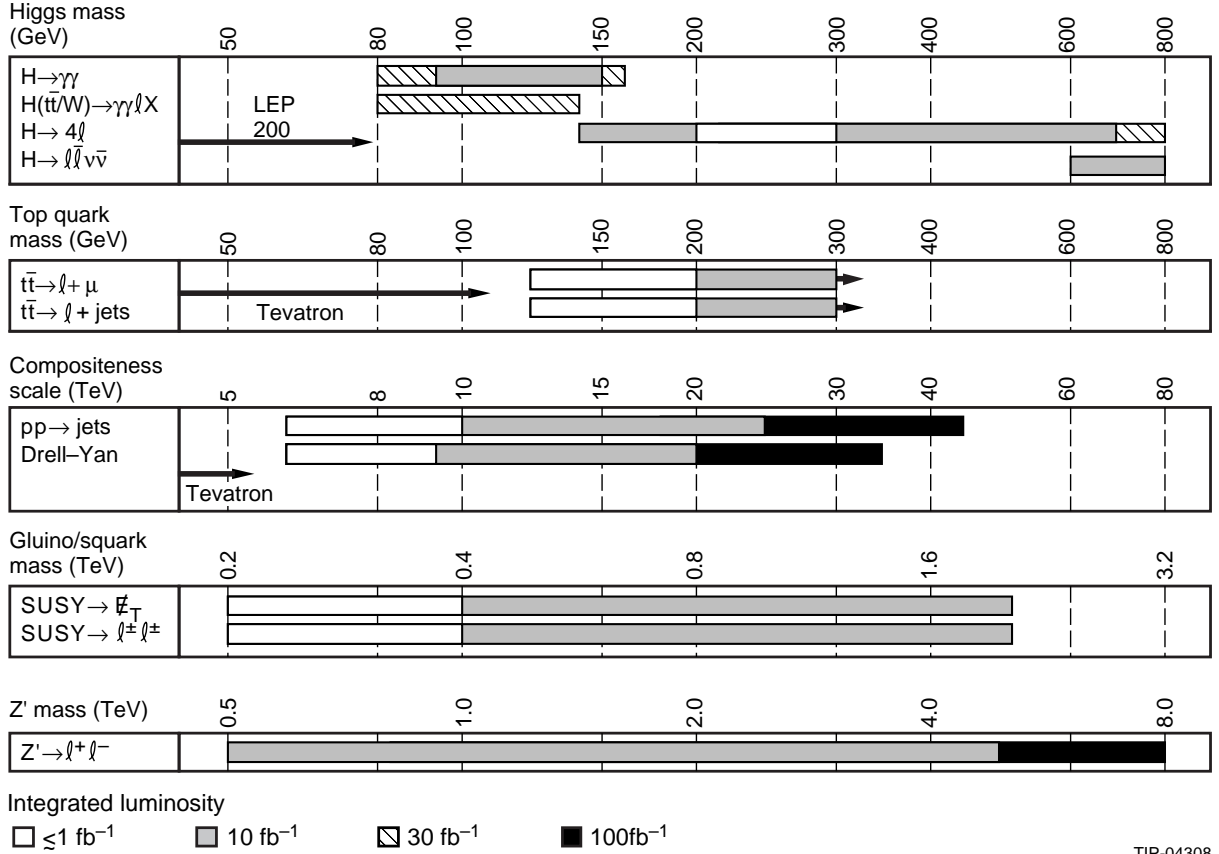
Table 1: Top-level specifications for the GEM detector.

Magnet	
Central field	0.8 T
Inner diameter	18 m
Length	31 m
Muon system	
Coverage	$0.1 <  \eta  < 2.5$
$\Delta p_T/p_T$ at $ \eta  = 0$ , $p_T = 500$ GeV	5%
$\Delta p_T/p_T$ at $ \eta  = 2.5$ , $p_T = 500$ GeV	12%
Charge separation ( $\eta = 0$ )	$p \leq 6.5$ TeV at 95% C.L.
Electromagnetic calorimeter	
Coverage	$ \eta  < 3$
Energy resolution	$6\text{--}8\%/\sqrt{E} \oplus 0.4\%$
Position resolution	$4.4 \text{ mm}/\sqrt{E}$
Pointing resolution	$40\text{--}50 \text{ mrad}/\sqrt{E} + 0.5 \text{ mrad}$
Hadronic calorimeter	
Coverage	$ \eta  < 5.5$
Jet resolution	$60\%/\sqrt{E} \oplus 4\%$
Tracker	
Coverage	$ \eta  < 2.5$
Charge separation at 95% C.L. ( $\eta = 0$ )	$p \leq 600$ GeV
Momentum resolution	
at high momenta (measurement limited)	$\Delta p/p^2 = 1.2 \times 10^{-3} \text{ GeV}^{-1}$
at low momenta (multiple scattering limited)	$\Delta p/p = 3.5\%$

### 3.1.2. Muon System

Muons were identified by their penetration through the calorimeter. Muon momentum was measured using the sagitta determined by three superlayers of chambers between the calorimeter and the magnet; see Fig. 3. Cathode strip chambers (CSC's) were chosen, based on the need to obtain the required spatial resolution, determination of the  $z$  coordinate, triggering, and occupancy, and the desire to use a single technology in both the endcaps and barrel. The resolution in the sagitta measurement varies as  $BL^2$ , where  $B$  is the magnetic field strength and  $L$  is the lever arm of the measurement. Through the use of a large lever arm and a moderate field, a precise momentum measurement was obtained:  $\Delta p_T/p_T = 5\%$  ( $12\%$ ) at  $\eta = 0$  ( $2.5$ ) for  $p_T = 500$  GeV.

The momentum resolution was limited at high momenta by the spatial measurement errors (both inherent and due to misalignment), and at low momenta by the multiple scattering in the middle superlayer of chambers and energy-loss fluctuations in the calorimeter. To be able to sign-select muons at very high momentum (e.g., from  $Z'$  decay



TIP-04308

FIG. 2: The physics reach of GEM.

at the highest mass,  $\sim 8\text{--}10$  TeV, that was accessible at the SSC) demanded single layer resolutions of  $75 \mu\text{m}$  and alignment between superlayers of  $25 \mu\text{m}$ . To avoid degrading the low-momentum muons which contribute to the signal for  $H^0 \rightarrow ZZ^* \rightarrow 4\mu$ , the middle muon chamber superlayer must be less than 10% of a radiation length in thickness.

In order to be sufficiently robust to operate at the highest luminosities ( $\mathcal{L} = 10^{34} \text{ cm}^{-2} \text{ s}^{-1}$ ) attainable at the SSC, the muon system was shielded by a thick ( $\geq 11\lambda$  at  $\eta = 0$ , increasing in the forward direction), nearly hermetic, calorimeter. The calorimeter thickness was chosen to keep the rate from punchthrough hadrons significantly below that from in-flight decay muons. In addition, a geometry for the forward calorimeter was chosen that minimizes the background.

A feature of the muon system was the use of a 0.2 m open space between the calorimeter and the first muon superlayer. This clear space allowed charged particles from electromagnetic showers initiated by high-momentum muons to be bent out of the muon path, leading to increased reconstruction efficiency.

### 3.1.3. Calorimeter

The general layout of the GEM calorimeter is shown in Fig. 4. In order to identify and

Scanned detector figure is too large for electronic distribution.

FIG. 3: Quarter view of the GEM detector showing the muon system, including shielding.

measure electrons and photons, a precision noble-liquid electromagnetic calorimeter was used, employing krypton in the barrel and argon in the endcap. This technology was chosen because of its ability to achieve the required resolution, longitudinal segmentation and pointing ability, its intrinsic radiation resistance, its ease of calibration, and the extensive experience that has been acquired with large liquid-argon systems. An accordion geometry was used to provide good hermeticity and allow for faster readout than parallel-plate calorimetry because of lower inductance and capacitance.

Behind the EM calorimeter was a hermetic hadronic calorimeter used both to measure jet energies and, in conjunction with the forward calorimeter, to measure  $\cancel{E}_T$ . The barrel hadron calorimeter was a hybrid system that performed the energy measurement primarily in a noble-liquid calorimeter (in the first  $\sim 6\lambda$ ), followed by a relatively inexpensive copper/scintillator calorimeter which provided energy measurement for late-developing showers and the necessary shielding for the muon system. In the end cap an all-liquid design was used.

In the forward region, additional calorimeters measured high-momentum particles near the beam pipe. Together with the barrel and endcap calorimeters, these forward calorimeters determined the sensitivity to  $\cancel{E}_T$ . In order to detect new particles such as massive gluinos and squarks, the forward calorimeter must cover the region  $|\eta| \lesssim 5.5$ , be sufficiently

Scanned detector figure is too large for electronic distribution.

FIG. 4: Quarter view of the GEM detector showing the calorimeters.

dense to contain hadronic showers, be sufficiently fast to cope with the high particle flux in this region, and be radiation hard. The design had a first section consisting of a liquid-argon tube calorimeter, followed by a liquid-scintillator-capillary and tungsten calorimeter. The calorimeter was optimized to obtain good spatial information in the first section and adequate shower containment in the second section.

#### 3.1.4. Central Tracker

The central tracker was 1.8 m in diameter by 3.5 m long, surrounding the interaction point. The tracker size was determined by the needs to obtain sufficient  $\pi^0$  rejection by shower shape analysis, to minimize the calorimeter cost, to optimize the tracker resolution, and to preserve sign-selection ability to high momenta. The layout of the tracker system is shown in Fig. 5.

The tracker supported the goal of measuring gammas, electrons, and muons at high  $p_T$ , at high luminosity, up to  $\mathcal{L} = 10^{34} \text{ cm}^{-2} \text{ s}^{-1}$ . The tracker provided good separation of gammas and electrons by finding a charged track, and measured the electron sign up to 600 GeV. The former is essential to the search for  $H^0 \rightarrow \gamma\gamma$  and to background rejection in  $Z' \rightarrow e^+e^-$ ; the latter, for the gluino search using the signature of same-sign leptons. Another important role for the tracker was to measure the position of the primary vertex. Physics involving  $b$ ,  $t$ , and  $\tau$  decays requires full pattern recognition capability, including

Scanned detector figure is too large for electronic distribution.

FIG. 5: The GEM central tracker.

secondary vertex finding and tracking at low momenta.

The design used two technologies. For the inner section of the tracker, silicon microstrips were used, giving the required fine segmentation and radiation resistance. For the outer section, interpolating pad chambers (IPC's) were chosen for their low occupancy, their ability to provide near three-dimensional space points, their high-luminosity capability, and their demonstrated operational resolution of  $50 \mu\text{m}$ .

### 3.1.5. Electronics/Data Acquisition

Triggering and data acquisition in GEM followed a three-level strategy to provide a system without deadtime that provided as much information as possible at each trigger level. It was designed for luminosities up to  $10^{33} \text{ cm}^{-2} \text{ s}^{-1}$ , with provision for operation at higher luminosities with modest upgrades. The architecture consisted of a synchronous and pipelined Level 1, an asynchronous Level 2 (possibly with special purpose hardware), and a Level 3 processor ranch. Full granularity data was available at Levels 2 and 3. Level 1 was designed to handle up to 60 MHz input rate, with an output rate of 10 kHz. Level 2 was designed to handle an average input rate up to 100 kHz, with an output rate of 300 Hz. Finally, Level 3 accepted 3 kHz, with an output rate of 100 Hz.

## 4. MODELING THE GEM DETECTOR

In principle, the full detector simulation programs GEANT and CALOR89 could be used to compute GEM's response to the signal and background for any process. However, these programs are very slow for complex events at high energy. It is impractical to use them to simulate the more than  $10^6$  events often needed to determine a rare signal's background arising from a combination of relatively likely processes. Consequently, two kinds of simulation were done for GEM. Detailed simulations, based on GEANT, of each of the individual detector systems have been performed for single particles or for limited numbers of complete events.<sup>38</sup> The results of these detailed studies have been parameterized and incorporated in `gemfast`, the fast simulation program for GEM that was used for determining the performance of the detector for physics processes. For example, parameterizations were made of energy and momentum resolutions and of muon reconstruction efficiency in the presence of other particles in the event of interest. Most of the results presented in this article are based on `gemfast`. Where necessary, hybrid simulations of `gemfast` and full GEANT have been used. For example, in the study of  $H^0 \rightarrow \gamma\gamma$ , detailed electromagnetic shower shape studies for real photons and jets faking photons were carried out with GEANT. Apart from examples such as this, `gemfast` describes the performance of GEM quite accurately.

The key to a fast detector simulation is to use a very simple geometry and to parameterize the response of each detector component in a simple way. The geometry used in `gemfast` is a set of concentric cylinders, one each for the central tracker (CT), electromagnetic calorimeter (EC), hadronic calorimeter (HC), scintillator calorimeter (SC), forward calorimeter (FC), and muon system (MU). The geometry is shown in Fig. 6. The radiation and absorption lengths in the cylinders representing the calorimeters are varied with  $\eta$  so as to match the true design. Particles are tracked through each successive volume on straight lines for neutral particles or on helices in a uniform magnetic field,  $B = 0.8$  T, for charged ones. Since the MU resolution is parameterized, particles need not be tracked through the nonuniform field in the muon system.

Once a particle enters a given detector system, its energy resolution, angular resolution, and detection efficiency are calculated using parameterizations of the single particle response. This simple, single-particle approach is not adequate for the central tracker reconstruction efficiency, which is sensitive to the presence of other tracks in the same event and to pileup, and which therefore has been investigated separately. Development of electromagnetic and hadronic showers in transverse and longitudinal directions, including fluctuations, is modeled and the individual tower energies are calculated. Unstable particles are allowed to decay anywhere in the detector using code adapted from the GEANT package. The Level 1 trigger response is also simulated.

### 4.1. Event Generation

The first step in simulating a process is to generate the events of interest. This is

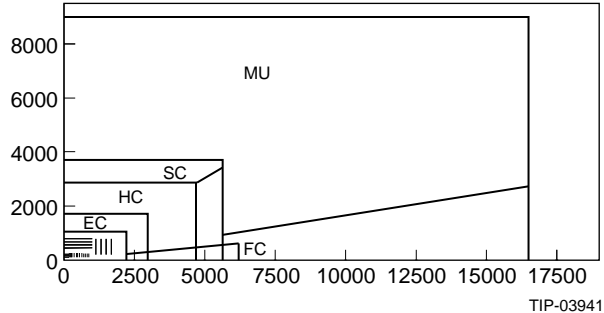


FIG. 6. Geometry used in **gemfast**. The detector is approximated by a set of concentric cylinders. Particles are tracked through the central tracker and calorimeters assuming a uniform magnetic field.

handled by **gemgen**,<sup>39</sup> which incorporates ISAJET,<sup>27</sup> PYTHIA,<sup>28</sup> and a single particle gun. The single particle gun generates a single particle at a given  $p_T$ ,  $\eta$ , and  $\phi$  or a single quark or gluon fragmented with PYTHIA.

The event generators are interfaced to the detector simulation in a way that allows adding a signal event and a Poisson-distributed number of minimum bias events in the same bunch crossing. The same or different generators can be used for each sample. The vertex position of each event is generated according to the expected width,  $\sigma_z = 5$  cm. The same approach could be used to describe pileup from out-of-time bunches. However, this is impractical because of the computing time required to generate minimum bias events over the tails on the sensitive time of the detector. Instead, out-of-time pileup events have been generated separately, the detector response to them has been parameterized, and the resulting noise or inefficiency taken into account for each of the detector systems.

## 4.2. Central Tracker

The single particle momentum and vertex position resolutions of the central tracker were calculated using a full GEANT simulation including the effects of the magnetic field, detector geometry, chamber positions and resolutions, material distribution including supports and cables, geometrical acceptance, detector efficiency, and distribution of the interaction vertex. The effect of out-of-time pileup was included as an additional inefficiency due to the detector deadtime. Both the silicon strips and the IPCs are used at a luminosity of  $10^{33} \text{ cm}^{-2}\text{s}^{-1}$ ; the silicon detector was assumed to be removed for  $10^{34} \text{ cm}^{-2}\text{s}^{-1}$ . Figures 7 and 8 show the resulting parameterization of the mean muon or pion resolution vs.  $p_T$  and  $\eta$  used in **gemfast** for  $10^{33} \text{ cm}^{-2}\text{s}^{-1}$  and  $10^{34} \text{ cm}^{-2}\text{s}^{-1}$ , respectively, assuming a vertex constraint. The impact parameter resolution for tracks is also parameterized, allowing modeling of vertex reconstruction on an event-by-event basis.

The reconstruction efficiency for isolated tracks exceeds 97% over the whole range of pseudorapidity  $|\eta| < 2.5$ . This is based on requiring at least ten good hits on a high- $p_T$  track. The number of hits is calculated in **gemfast** using the positions of the chambers and

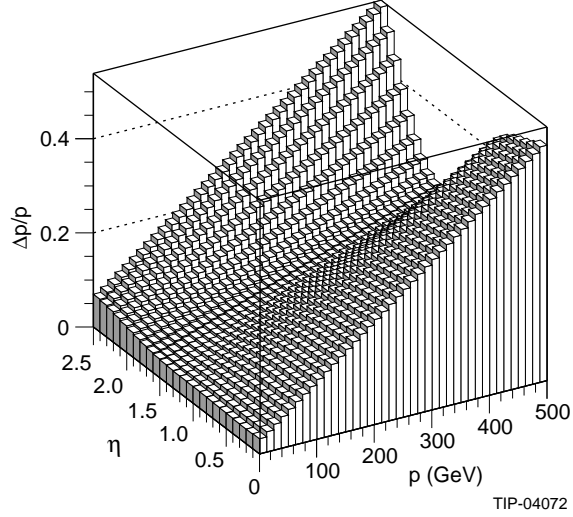


FIG. 7. Parameterization of vertex-constrained central tracker resolution in `gemfast` for muons or charged hadrons vs.  $p_T$  and  $\eta$  for  $\mathcal{L} = 10^{33} \text{ cm}^{-2} \text{ s}^{-1}$ . Both the silicon tracker and the interpolating pad chambers are used.

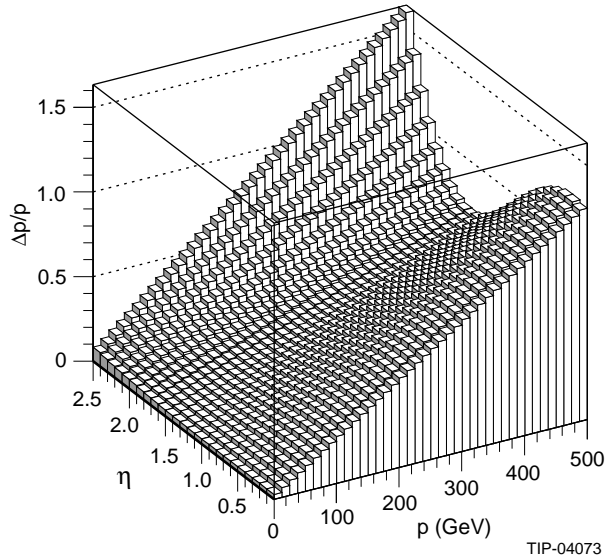


FIG. 8. Parameterization of vertex-constrained central tracker resolution in `gemfast` for muons or charged hadrons vs.  $p_T$  and  $\eta$  for  $\mathcal{L} = 10^{34} \text{ cm}^{-2} \text{ s}^{-1}$ . The silicon tracker is assumed to be removed.

the actual origin of the track. It is difficult to parameterize the reconstruction efficiency for non-isolated tracks, so the simulations described here use only tracks which have  $p_T > 1$  GeV and which are isolated at the generator level in a  $\Delta\eta \times \Delta\phi$  region corresponding to three pads in the IPCs.

The momentum resolution for electrons has been treated separately, taking into account the emission of bremsstrahlung photons caused by the material in the tracker. (The

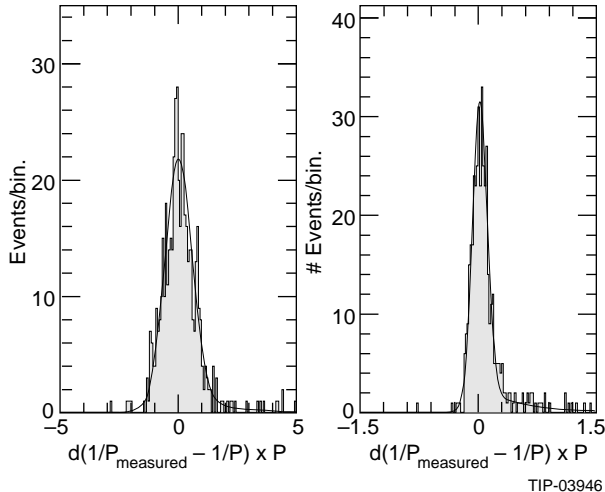


FIG. 9. Calculated momentum resolution function for electrons in the central tracker at  $p_T = 525$  GeV for  $0 < |\eta| < 0.2$  (left plot), and  $p_T = 10$  GeV for  $2.2 \leq \eta \leq 2.4$  (right plot). The histogram shows the GEANT simulation, and the smooth curve is the parameterization used in `gemfast`.

photons are assumed to be emitted nearly parallel to the electron and to hit the same calorimeter cell, so that the calorimeter energy resolution is not degraded.) Figure 9 shows the electron momentum resolutions at a particular value of  $p_T$  and  $\eta$  from the full GEANT simulation and from the corresponding parameterization used in `gemfast`. The parameterization fits the GEANT data well, including the bremsstrahlung tails. These are important for electron sign determination, which can be done up to  $p_T \lesssim 600$  GeV.

Material in the central tracker is parameterized as a function of  $\eta$  and  $\phi$  after each layer of the silicon or IPCs, and this is used to convert photons at appropriate space points. Secondary  $e^+e^-$  pairs are generated using code adapted from GEANT.

### 4.3. Calorimeter

The parameterized response of the central calorimeter, which covers  $|\eta| < 3$ , includes shower profiles and energy resolutions. Longitudinal and transverse electromagnetic and hadronic shower profiles are generated using GFLASH 1.3, which was originally developed to describe the H1 liquid argon calorimeter.<sup>40</sup> It has been modified to work with the `gemfast` geometry. GFLASH incorporates correlated fluctuations of shower profile parameters, hadronic shower fluctuations into early  $\pi^0$ 's, transverse profile variations with depth, and shower development along the true direction of incidence as determined by tracking through the central tracker region. It gives a good description of the shapes of both electromagnetic and hadronic showers in uniform regions of the calorimeter, as illustrated in Figure 10. GFLASH is used to distribute shower energies among calorimeter towers. The electromagnetic, liquid-hadronic, and scintillator tail-catcher towers are modeled separately, but further longitudinal segmentation is neglected for faster execution.

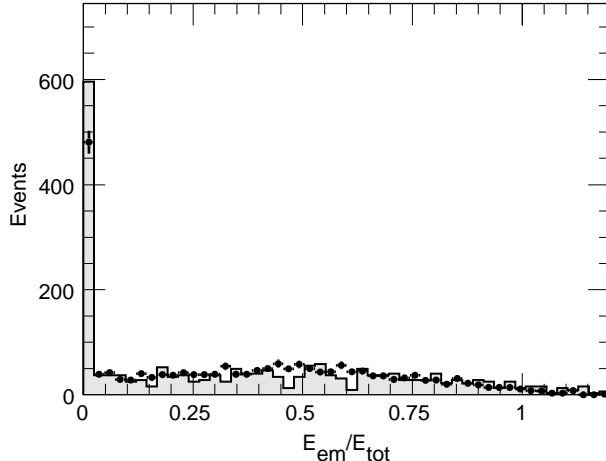


FIG. 10. Ratio of electromagnetic to total energy for 100 GeV pions. The histogram shows the result of a full GEANT simulation, and the points show the GFLASH-based parameterization used in `gemfast`.

The segmentation of the calorimeter is varied realistically with  $\eta$ . The simulated endcap segmentation is in  $\eta$ - $\phi$  rather than in  $x$ - $y$ , but this should have no effect on physics performance. The EC and HC segmentations are  $\Delta\eta \times \Delta\phi = 0.026 \times 0.026$  and  $0.08 \times 0.08$  in the middle of the barrel. Since the segmentation is approximately constant in units of radiation or absorption lengths, it is about a factor of six coarser at the small-angle edge of the endcap than in the middle of the barrel.

The energy resolution of the electromagnetic calorimeter has been calculated using a GEANT simulation including an extremely detailed geometry and very low cutoffs. A similar simulation gave good agreement with test beam data for the non-projective accordion. The resolution has been parameterized in the form

$$\frac{\Delta E}{E} = \frac{a(\eta)}{\sqrt{E}} \oplus b(\eta), \quad (4.1)$$

with the parameters tuned to give the correct resolution as a function of  $E$  and  $\eta$  for the  $5 \times 5$  sum of towers used to obtain optimal resolution for isolated electrons and photons. Typically, the stochastic term ( $a$ ) is about 6% in the barrel and about 8% in the endcap, and the constant  $b$ -term is about 0.4%. Pileup and noise are not included in the energy resolution but are added separately.

The pointing resolution of the electromagnetic calorimeter for photons was calculated using the same detailed GEANT simulation. It is parameterized as

$$\Delta\theta = \frac{a_\theta(\eta)}{\sqrt{E}} + b_\theta(\eta), \quad (4.2)$$

for low to moderate energies, where  $a_\theta$  is about 40 mrad in the barrel and 50 mrad in the endcap and  $b_\theta(\eta)$  is about 0.5 mrad. At the highest energies, for which the shower is no longer fully contained in the EM calorimeter,  $\Delta\theta \approx 2$  mrad.

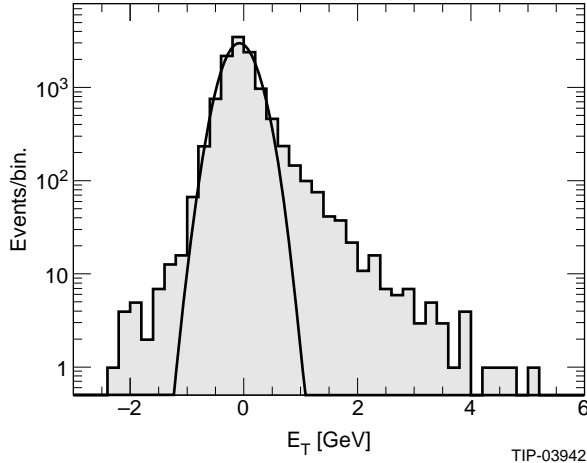


FIG. 11. The histogram shows the distribution of pileup, including out-of-time events, in `gemfast` for a  $0.16 \times 0.16$  electromagnetic trigger tower.

Thermal noise is added to each tower depending on  $\eta$ . In-time pileup events are added explicitly. To determine the effects of out-of-time pileup, a Poisson-distributed number of minimum bias events is generated for each of the 50 preceding and 20 following bunch crossings and simulated with `gemfast`. The calorimeter response for each bunch crossing is weighted with a response function that takes into account the intrinsic calorimeter response and the shaping circuit in the electronics, using shaping times of 40 ns for the electromagnetic calorimeter and 100 ns for the hadronic calorimeter. The sum for each cell is calculated to provide a snapshot of the response to pileup. This ensures that all the longitudinal and transverse correlations among cells, caused either by individual shower shapes or by jets, are preserved. One of these snapshots is then superimposed on the response from the signal and in-time pileup events. As can be seen from Fig. 11, this approach gives larger fluctuations and a smaller half-width than the equivalent Gaussian noise.<sup>41</sup> For the analyses described here a sample of  $10^4$  such snapshots has typically been used.

The GEM calorimeter design has an intrinsic  $e/h \neq 1$ , so reconstructing a jet energy as a simple sum of the observed energies in the various layers would give a large constant term in the resolution. This effect can be reduced by using an iterative weighting procedure.<sup>42,43</sup> To save execution time this weighting is not implemented in `gemfast`. Instead, the sampling and constant terms in the single hadron resolution have been tuned so that the jet energy resolution from `gemfast` matches that from the detailed GEANT simulations including the weighting. The resulting resolution for isolated jets is

$$\left. \frac{\Delta E}{E} \right|_{\text{jet}} = \frac{0.6}{\sqrt{E}} \oplus 0.04. \quad (4.3)$$

For many cases the effects of the clustering algorithm used to define jets are comparable to those of energy resolution.

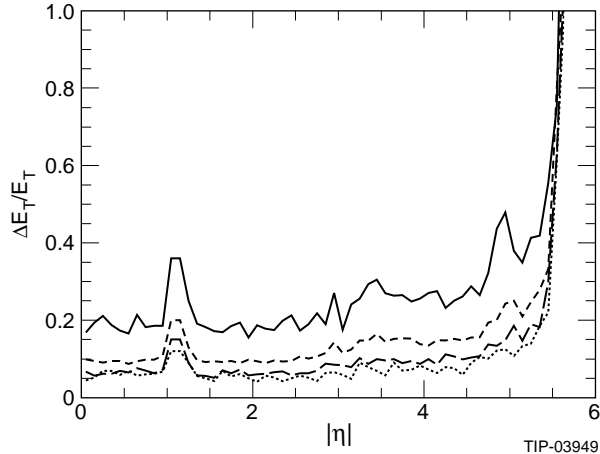


FIG. 12. Calorimetric  $E_T$  resolutions for hadrons vs.  $\eta$  for  $E = 10$  GeV (solid line), 50 GeV (dashed line), 200 GeV (dotted line), and 500 GeV (dash-dotted line) used in `gemfast` for the calculation of  $\cancel{E}_T$ . Most of the fluctuations are caused by limited statistics in the GEANT simulation.

The forward calorimeter covers  $3 < |\eta| < 5.5$ , with full measurement capability to  $|\eta| \approx 5.0$ . It has been used in the physics studies described here only to determine the missing energy,  $\cancel{E}_T$ . For this, detailed simulation of the response of individual cells is not needed. Rather, the energy and direction of each particle hitting the forward calorimeter is smeared according to a parameterization derived from a GEANT simulation. The simulation includes all the effects of dead material and shower spreading across calorimeter boundaries. The resulting  $E_T$  resolution as parameterized in `gemfast` is shown in Fig. 12. The statistics in this simulation were not sufficient to study potential nongaussian tails. These are modeled in `gemfast` by adding a second Gaussian with a small amplitude and a larger width. Test beam data for single hadrons from 50 to 100 GeV in the DØ liquid argon calorimeter show a tail composed of roughly 1% of the events with a standard deviation two to three times larger than the Gaussian calorimeter resolution.<sup>44</sup> This tail is slightly larger than that seen for 1 TeV jets in GEANT studies of jet resolution using energy-dependent weighting. A similar tail has been assumed for GEM.

#### 4.4. Muon System

The muon momentum resolution has been calculated by a full GEANT simulation including a detailed model of the detector and its support structures. The calculation includes chamber resolutions and alignment errors, the calculated shape of the magnetic field, the number of CSC planes in the measurement, and multiple scattering from the chambers and their supports. It is described at length elsewhere.<sup>45</sup> The resulting parameterization of the resolution is shown in Fig. 13. The jumps in the curves come from the transitions between various sets of chambers in the barrel and endcap. The flattening in the resolution at  $\eta \simeq 2.5$  is the effect of the forward field shapers.

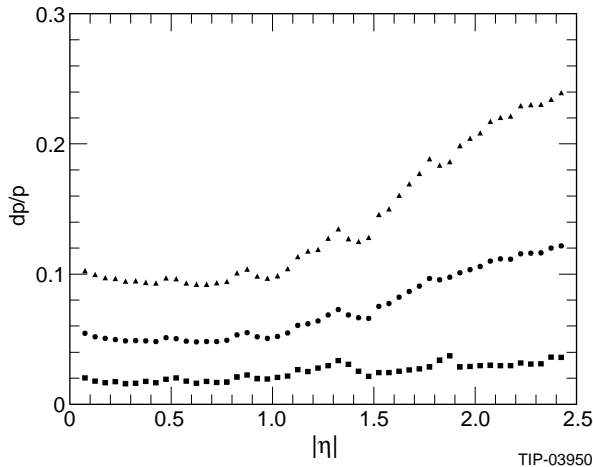


FIG. 13. Parameterization of muon resolution vs.  $\eta$  for  $p_T = 100$  GeV (squares), 500 GeV (circles), and 1 TeV (triangles) in **gemfast**.

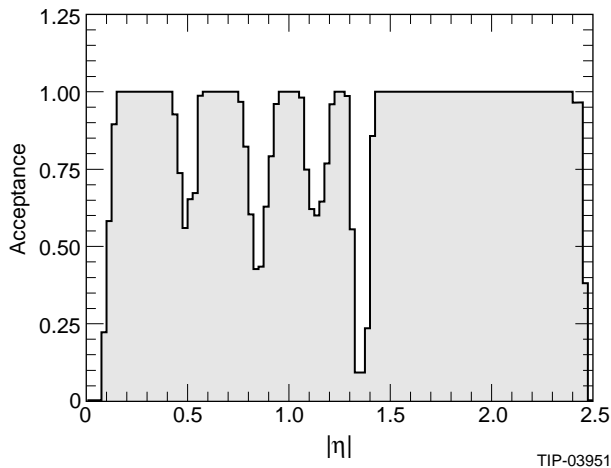


FIG. 14. Parameterization of muon acceptance vs.  $\eta$  in **gemfast**. Because of binning of the GEANT data, the gaps in the barrel are wider than in reality but have nonzero acceptance. The average acceptance is correct.

The geometrical acceptance for muons has been calculated similarly, requiring that the muon pass through at least three chambers in each superlayer. (This is overly conservative,<sup>45</sup> since fairly good muon resolution can be obtained from two superlayers at low  $p_T$  or from two superlayers plus the vertex at high  $p_T$ .) The three-superlayer acceptance is shown in Fig. 14 and is essentially independent of muon energy. The coverage of the region  $|\eta| < 2.46$  is 83%. The losses due to the spoiling of hits by  $\delta$  rays and other electromagnetic interactions have also been simulated by GEANT, parameterized as a function of muon energy, and included in **gemfast**.

The muon energy loss in the calorimeter has been calculated, including all the processes modeled in GEANT, and has been parameterized with a simple analytic function. The full calculation and the parameterization are shown in Fig. 15. The lost energy is added to the

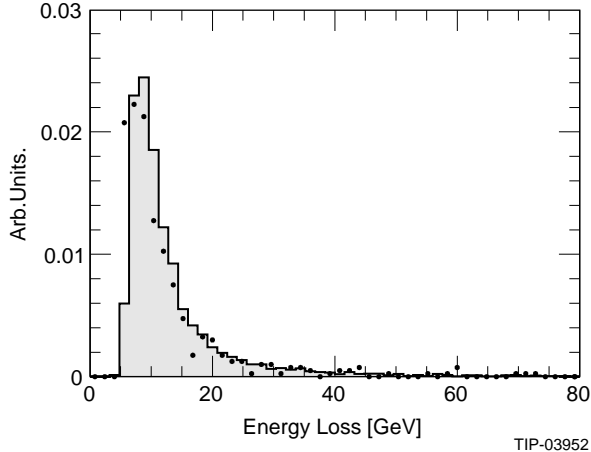


FIG. 15. Muon energy loss in calorimeter for  $E_\mu = 500$  GeV (solid curve) and `gemfast` parameterization (dots). Note that the tail at large energy loss is fit well by the parameterization.

appropriate cells of the calorimeter so that energy losses large compared to the noise can be reconstructed in `gemfast`. The best resolution is obtained by using the measured energy if it is greater than a factor  $k \sim 1.5$  times the most probable value, and the truncated mean value otherwise.

#### 4.5. Trigger Simulation

The Level 1 trigger efficiency is simulated in `gemfast` and included in the analyses described below. The Level 2 and Level 3 triggers are assumed to be included, to a first approximation, in the cuts made in the analysis.

An initial set of trigger thresholds is shown in Table 2. The  $E_x$  triggers include an isolation cut on the surrounding towers and on the hadronic energy behind the cluster. The  $J_x$  triggers sum the electromagnetic and hadronic sections in towers reasonably matched to the size of a QCD jet. The  $M_x$  thresholds are nominal values at which the acceptance is 84% and include the coarse resolution of the trigger roads. The missing energy simulation uses the full sum of the calorimeter. While the highest thresholds in Table 2 have acceptable rates by themselves, the lower thresholds can only be used either with prescaling or in combinations.

Twelve combinations of the primitives listed in Table 2 appear to be sufficient to select all the physics processes so far considered for GEM; they give a total Level 1 trigger rate less than the design goal of 100 kHz. In particular they provide triggers with good efficiency for low-mass Higgs bosons and the other (relatively) low-mass processes listed in Table 3. The most difficult trigger is that for inclusive  $H \rightarrow \gamma\gamma$  at the low end of the mass range. Some low- $p_T$  processes such as jets have such large cross sections that they must be prescaled. No attempt has been made to implement an efficient trigger on the inclusive- $b$  cross section to study  $b$ -physics, although this might be of interest during the

Table 2. Primitives used in the GEM trigger. The highest threshold can be used alone; the rest can be used in conjunction with other triggers.

Name	Definition	Thresholds
$E_x$	EM cluster with $E_T > x$ GeV in $0.16 \times 0.16$ , isolated in both EM and HAD calorimeters.	$E_8, E_{16}, E_{50}, E_{80}$
$M_x$	Muon with $p_T > x$ GeV.	$M_{10}, M_{20}, M_{30}, M_{40}$
$J_x$	Jet cluster with $E_T > x$ GeV in $0.48 \times 0.48$ .	$J_{16}, J_{50}, J_{80}, J_{200}$
$\cancel{E}_x$	Missing energy $\cancel{E}_T > x$ GeV summing whole calorimeter.	$\cancel{E}_{50}, \cancel{E}_{100}$

Table 3. Trigger efficiencies for a variety of processes using the triggers shown in Table 2 with standard logical notation. The triggers listed are the principal ones among those studied, but the efficiency is for the sum of all combinations. The efficiency for  $H \rightarrow \ell^+\ell^-\ell^+\ell^-$  at 140 GeV could be increased about 5% by adding an  $E_{16} \wedge M_{10}$  trigger. The last four processes are useful mainly for calibration.

Process	Mass	Trigger	Efficiency
$H \rightarrow \gamma\gamma$	80 GeV	$2E_{16} \vee E_{50}$	78.7%
$H \rightarrow \gamma\gamma$	140 GeV	$2E_{16} \vee E_{50}$	94.7%
$t\bar{t}H \rightarrow \gamma\gamma\ell X$	80 GeV	$2E_{16}$	94.4%
$H \rightarrow \ell^+\ell^-\ell^+\ell^-$	140 GeV	$2M_{10} \vee 2E_{16}$	81.8%
$H \rightarrow \ell^+\ell^-\ell^+\ell^-$	400 GeV	$2M_{10} \vee 2E_{16}$	99.8%
$H \rightarrow \ell^+\ell^-jj$	800 GeV	$2M_{10} \vee 2E_{16}$	99.9%
$t\bar{t} \rightarrow \ell\nu bX$	140 GeV	$E_{50} \vee M_{30}$	75.3%
$\tilde{g}\tilde{g}$	500 GeV	$3J_{80} \wedge \cancel{E}_{100}$	99.9%
$W \rightarrow e\nu$	—	$E_{16} \wedge \cancel{E}_{50}$	15.8%
$W \rightarrow \mu\nu$	—	$M_{10} \wedge \cancel{E}_{50}$	48.7%
$Z \rightarrow ee$	—	$2E_{16}$	80.3%
$Z \rightarrow \mu\mu$	—	$2M_{10}$	86.9%

low-luminosity initial period. Level 1 triggers on the higher mass processes which have been considered are generally easier than those listed in Table 3.

## 5. STUDIES OF PHYSICS PROCESSES

### 5.1. Selection of Processes

We have studied the performance of the GEM detector for a variety of physics processes chosen both because they probe the capabilities of important components of the detector and because of their intrinsic physics interest:

- Section 5.2 presents an in-depth study of the search for the Higgs boson of the Standard Model. The signals, backgrounds and discovery potential for  $M_H = 80 - 800$  GeV are discussed. Depending on the Higgs mass, the modes studied are  $H^0 \rightarrow \gamma\gamma$ ;  $H^0(t\bar{t}/W) \rightarrow \ell^\pm\gamma\gamma X$ ;  $H^0 \rightarrow ZZ^{(*)} \rightarrow 4$  charged leptons;  $H^0 \rightarrow ZZ \rightarrow \ell^+\ell^-\bar{\nu}\nu$ ; and  $H^0 \rightarrow ZZ \rightarrow \ell^+\ell^-$  jet jet.
- Flavor physics involving top-quarks is discussed in Section 5.3. We describe the mass measurement of a heavy top-quark in the standard decay mode  $t \rightarrow W^+b$  using two methods:  $t \rightarrow$  isolated  $\ell^+$  plus non-isolated  $\mu^-$ , and  $t \rightarrow 3$  jets. We also discuss the discovery of a charged Higgs boson in the nonstandard decay mode  $t \rightarrow H^+b$ , followed by  $H^+ \rightarrow \tau^+\nu_\tau$ .
- Jet physics is studied in Section 5.4. We discuss the determination of the jet energy scale, using as a physics context the search for quark substructure in high- $E_T$  jets. Other jet studies are discussed in Sections 5.2 ( $H^0 \rightarrow Z^0Z^0 \rightarrow \ell^+\ell^-$  jet jet) and 5.3 ( $t \rightarrow W^+b \rightarrow 3$  jets).
- Supersymmetry is discussed in Section 5.5 as an example of missing transverse energy signatures for new physics. The  $\cancel{E}_T$  distribution is calculated for GEM, including the effects of transition regions and dead material. The  $\cancel{E}_T$  signature is studied for a range of gluino and squark masses. In addition, the like-sign dilepton signature for gluino production is investigated.
- Section 5.6 is devoted to studies of high-mass-scale physics at ultrahigh luminosity (for the SSC),  $\mathcal{L} \simeq 10^{34} \text{ cm}^{-2} \text{ s}^{-1}$ . These physics studies include precision investigations of the properties of a very massive  $Z'$  boson in its  $e^+e^-$  and  $\mu^+\mu^-$  decay channels, and the character of quark-lepton substructure contact interactions via the process  $\bar{q}q \rightarrow \mu^+\mu^-$ .

For all these processes, the performance of the GEM design has been determined realistically. This is an important step in optimizing the design. Results are given below for a variety of integrated luminosities:  $10 \text{ fb}^{-1}$  and  $30 \text{ fb}^{-1}$ , corresponding to one and three years of operation at the design luminosity of  $10^{33} \text{ cm}^{-2} \text{ s}^{-1}$ ; and  $100 \text{ fb}^{-1}$ , corresponding to one year at a peak luminosity of  $10^{34} \text{ cm}^{-2} \text{ s}^{-1}$ .

As noted above, the upper limit on the top-quark mass was 95 GeV at the time most of the work described here was done. Except in Section 5.3, a top mass of 140 GeV was used in the simulations. If a top mass of 175 GeV were used, this would sometimes increase

signals (as in gluon fusion of a standard Higgs boson) and/or backgrounds and sometimes decrease them. Overall, we do not think that a significant quantitative change would result from using the higher mass.

## 5.2. Standard Model Higgs Physics

Here we describe searches for the minimal Standard Model Higgs boson with the GEM detector in the mass range between 80 and 800 GeV. This covers the interval between lower limits from LEP (which have excluded the mass range below  $\sim 60$  GeV,<sup>49</sup> and should reach 80–90 GeV at LEP 200;<sup>50</sup> and the triviality bounds discussed above.<sup>15</sup> The details of these Higgs boson search studies are presented in Ref. 51. Higgs bosons in extensions of the standard model such as the minimal supersymmetric model<sup>52</sup> generally have similar signatures, albeit with different cross sections.

The dominant decay modes of the standard model Higgs boson are  $W^+W^-$  and  $ZZ$  for  $M_H > 2M_W$  and heavy fermion pairs for  $M_H < 2M_W$ . The latter, and the dominant decays of  $W$ 's and  $Z$ 's into jets, all have large backgrounds, so it is necessary to rely on rare decays. The cleanest channel is  $H \rightarrow ZZ/ZZ^* \rightarrow \ell^+\ell^-\ell^+\ell^-$  ( $\ell = e, \mu$ ), which has four isolated high- $p_T$  leptons in the final state. This channel has an inadequate rate at the lowest and highest ends of the mass range. Hence, the search may be divided into three mass regions:

- A Higgs boson of “intermediate” mass ( $80 \text{ GeV} < M_H < 2M_Z$ ) will be searched for through its decays  $H \rightarrow \gamma\gamma$  and  $H \rightarrow ZZ^* \rightarrow \ell^+\ell^-\ell^+\ell^-$ . Both direct  $H \rightarrow \gamma\gamma$  and lepton-associated production ( $t\bar{t}/W$ ) $H \rightarrow \gamma\gamma\ell X$  will be used.
- A heavy Higgs ( $2M_Z < M_H < 600 \text{ GeV}$ ) will be searched for through the channel  $H \rightarrow ZZ \rightarrow \ell^+\ell^-\ell^+\ell^-$ .
- A very heavy Higgs ( $M_H \approx 800 \text{ GeV}$ ) will also be searched for in  $\ell^+\ell^-\ell^+\ell^-$  and in the channels  $H \rightarrow ZZ \rightarrow \ell^+\ell^-\nu\nu$  and  $H \rightarrow ZZ \rightarrow \ell^+\ell^-jj$ .

The Monte Carlo event generator used in this study was PYTHIA 5.6 and JETSET 7.3.<sup>28</sup> The top quark mass was assumed to be 140 GeV. The study was carried out for the SSC design luminosity  $\mathcal{L} = 10^{33} \text{ cm}^{-2}\text{s}^{-1}$ .

Table 4 summarizes the significance with which GEM could discover the Higgs through the channels listed above. This demonstrates the sensitivity of the GEM detector at greater than the  $5\sigma$  level for the whole range of Higgs masses considered. The signal can be seen with an integrated luminosity of  $10 \text{ fb}^{-1}$ , except for  $M_H < 100 \text{ GeV}$  where 20 to  $30 \text{ fb}^{-1}$  are needed.

The most difficult part of the Higgs spectrum is the low end (between 80 and 100 GeV) and the region between the  $WW$  and  $ZZ$  thresholds, 170–180 GeV. GEM is sensitive to a Higgs with  $M_H$  below 100 GeV in both the two-photon and in the two-photon plus lepton

Table 4: Sensitivity of the GEM detector to standard model Higgs boson signals.

$M_H$ (GeV)	$\int \mathcal{L} dt$ (fb $^{-1}$ )	$\gamma\gamma$	$\gamma\gamma\ell$	$\ell^+\ell^-\ell^+\ell^-$	$\ell^+\ell^-jj$	$\ell^+\ell^-\nu\nu$	Combined
80	30	3.9 $\sigma$	4.5 $\sigma$				6.3 $\sigma$
90	30	4.9 $\sigma$	4.9 $\sigma$				7.2 $\sigma$
100	10	4.6 $\sigma$	2.9 $\sigma$				5.8 $\sigma$
120	10	7.8 $\sigma$	2.7 $\sigma$				8.5 $\sigma$
140	10	9.0 $\sigma$	2.3 $\sigma$	11 $\sigma$			15 $\sigma$
150	10	7.3 $\sigma$		13 $\sigma$			15 $\sigma$
160	10	3.2 $\sigma$		8.1 $\sigma$			8.9 $\sigma$
170	10			5.7 $\sigma$			5.7 $\sigma$
180	10			10 $\sigma$			10 $\sigma$
200	10			38 $\sigma$			38 $\sigma$
400	10			28 $\sigma$			28 $\sigma$
600	10			9.7 $\sigma$			9.7 $\sigma$
800	10			4.2 $\sigma^*$	1.0 $\sigma^*$	4.2 $\sigma^*$	6.6 $\sigma^*$

\* Estimated systematic errors.

channels. This would allow the confirmation of a Higgs signal in two decay channels necessary for a credible discovery claim in this mass region.

Over the entire Higgs mass range the dominant production mechanism at the SSC is gluon fusion, although vector-boson fusion is also important. The Higgs can also be produced associated with a vector boson or a top quark pair ( $t\bar{t}$ ) which provides an isolated lepton tag.

In the standard model, a Higgs boson with mass  $M_H > 2M_Z$  has a width which grows like  $M_H^3$ , but it remains fairly narrow for  $M_H < 600$  GeV. Figure 16 shows the lowest order Higgs production cross section multiplied by specific decay branching ratios for the five modes studied in this section. These cross sections were calculated using PYTHIA 5.6 with the EHLQ-1 parton distribution functions and a top quark mass of 140 GeV. Calculations of these cross sections using the more modern HMRS<sup>53</sup> and CTEQ<sup>54</sup> distributions differ from EHLQ-1 by less than 20%.<sup>55</sup> Higher order QCD corrections are not included in Fig. 16.

The physics signatures of Higgs decays all involve identification of isolated photons, electrons and muons. Since the Higgs cross sections are small and the potential backgrounds are large, this identification requires particular care. First, an isolation cut is applied, removing most of the jet background. Then, a detailed identification algorithm is used. The isolation cut for selecting electron and photon candidates was done using

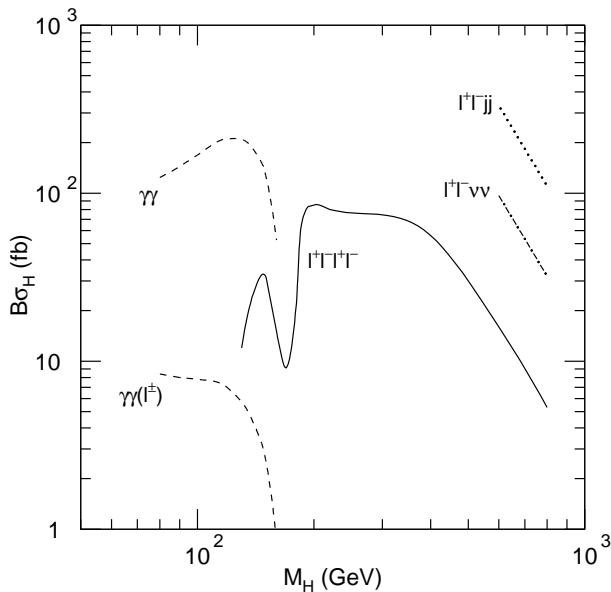


FIG. 16: Lowest order Higgs cross sections into observable modes vs. mass.

`gemfast` and requiring

$$\sum_R E_T - E_T^{\gamma/e} < E_T^{\text{mean}} + E_T^{\text{cut}}, \quad (5.1)$$

where the sum is over calorimeter towers in a cone of radius  $R$ . Generally,  $R = 0.45$  was used for two-body final states and  $R = 0.30 - 0.35$  for four bodies. The transverse energy  $E_T^{\gamma/e}$  of the  $\gamma$  or  $e$  candidate was found by summing the energy deposited in  $5 \times 5$  cells in the electromagnetic calorimeter;  $E_T^{\text{mean}}$  is the mean transverse energy from pileup and noise; and  $E_T^{\text{cut}}$  is the isolation threshold imposed.

The  $E_T^{\text{cut}}$  value was determined from the distribution of the thermal and pile-up noise<sup>56</sup> as described in Section 4.3. A Gaussian fit to the total noise in an  $\eta - \phi$  cone of radius  $R = 0.45$  gives a width of 3.4 GeV. This is reduced to 1.7 GeV if only those cells with  $|E_T| > 0.5$  GeV are summed. Doing this shifts the  $E_T^{\text{mean}}$  from 0.22 to 1.5 GeV, and reduces the signal loss from 13% to 7.6% for  $E_T^{\text{cut}} = 4$  GeV, the value used here.

For photons, there must be no reconstructed charged track in the  $5 \times 5$  cells. The central tracker can reject 95% of the electrons while keeping 96% of the photons. For electrons, there must be exactly one charged track in the central  $3 \times 3$  cells. Also, the energy and shower position measured in the EM calorimeter must match the momentum and track position measured in the central tracker. The background to  $H \rightarrow \gamma\gamma$  from misidentified  $Z \rightarrow e^+e^-$  is potentially large for  $M_H \approx M_Z$  and is discussed below.

A more complete understanding of the capability of GEM to identify isolated photon and electron candidates based on their shower shape requires a detailed GEANT simula-

tion. A sufficiently detailed geometry was available for only three  $11 \times 11$  cell regions of the barrel.<sup>57</sup> Therefore, the photons hitting the  $5 \times 5$  cluster were rotated to the nearest of these regions, and the full simulation was run. Shower shape cuts (including lateral and longitudinal shower distributions), information from the narrow  $\theta$  strips of the first segment of the EM calorimeter, and energy in the hadronic calorimeter are combined in a likelihood function and used to select single electromagnetic showers. Typically this rejects 75% of the remaining jet background while keeping 90% of the single photons. The probability of a QCD jet faking an isolated electron,  $\mathcal{R}(e/\text{jet})$ , was determined to be approximately  $10^{-5}$  by using detailed GEANT simulation.<sup>57,58</sup> For channels needing very good resolution, such as  $H \rightarrow \gamma\gamma$  and  $H \rightarrow ZZ^* \rightarrow e^+e^-e^+e^-$ , photons and electrons were required not to be in the region of degraded resolution between the barrel and the endcap,  $1.01 < |\eta| < 1.16$ . The overall photon identification efficiency, including this geometrical loss and other cuts, is between 80% and 85%. The electron identification efficiency is 85% – 90%. For signals such as  $H \rightarrow ZZ \rightarrow e^+e^-e^+e^-$  for  $M_H > 2M_Z$ , one electron was allowed to hit this transition region.

Muons were simulated using **gemfast**. They are relatively free of jet background and so require less stringent identification cuts. An isolation cut was made,

$$\sum_R E_T - \Delta E < E_T^{\text{mean}} + E_T^{\text{cut}}, \quad (5.2)$$

where  $\Delta E$  is the energy loss of a muon in the calorimeter, calculated as explained in Section 4.4. This eliminates muons from  $b$  and  $c$  decay, secondary decay muons in jets and punchthrough. The isolation cone radius was taken to be 0.35 for intermediate mass Higgs searches and 0.3 for heavier masses. The angle and momentum of the track measured in the muon system is then matched to that in the central tracker. The muon identification efficiency is around 80% for muons within  $|\eta| < 2.5$ , which includes factors of 85% from the geometrical acceptance and 95% from the muon track reconstruction and identification efficiency.<sup>45</sup>

Significance is used to indicate how well a Higgs signal can be identified in the presence of background. As in Gaussian statistics, a probability of  $1 - 1.35 \times 10^{-3}$  is expressed as a significance of  $3\sigma$ ,  $1 - 2.85 \times 10^{-5}$  is expressed as  $5\sigma$ , and so on. In this section, a  $5\sigma$  significance is generally regarded as the minimum for discovery.

### 5.2.1. $H \rightarrow \gamma\gamma$ Search for $80 \text{ GeV} < M_H < 160 \text{ GeV}$

Precision electromagnetic energy resolution is essential for the  $H \rightarrow \gamma\gamma$  search because of the small production cross section (60 to 200 fb), the narrow decay width (3 to 100 MeV) of the Higgs boson between 80 and 160 GeV, and the large QCD  $\gamma\gamma$  background. There is a potentially much larger background from QCD jets fragmenting into electromagnetic particles, which can be reduced using isolation cuts and a shower shape analysis made

possible by the fine segmentation of the calorimeter. In PYTHIA, jets can radiate prompt photons as an option. This is properly regarded as an approximation to part of the higher order QCD corrections to the  $\gamma\gamma$  background. Since these corrections are explicitly known for both the Higgs signal and the  $q\bar{q} \rightarrow \gamma\gamma$  background, the prompt photon radiation has been turned off, and the PYTHIA signal and background cross sections have been scaled to the higher order results.

Events were selected using the following cuts:

1.  $|\eta^\gamma| < 2.5$  and  $p_T^\gamma > 20$  GeV.
2. Photon isolation cut with  $R = 0.45$  and  $E_T^{\text{cut}} = 4$  GeV, and veto on  $1.01 < |\eta| < 1.16$ .
3. Photon identification based on detailed shower shape.
4. Electron rejection, as described below.
5.  $|\cos\theta^*| < 0.7$ , where  $\theta^*$  is the polar angle of photon in the center of mass system of two photons.

Cut 1 simply ensures that the photons are in the overall acceptance of the detector and are triggered on. Cuts 2 and 3 reduce the large potential backgrounds from misidentified QCD  $\gamma$ -jet and jet-jet events well below the  $\gamma\gamma$  continuum. Cut 4, which is only important for  $M_H \approx M_Z$ , removes the background from misidentified electrons. Finally, cut 5 reduces the real and fake  $\gamma\gamma$  backgrounds. This leaves the  $H \rightarrow \gamma\gamma$  signal as a narrow bump in the  $M_{\gamma\gamma}$  distribution.

The significance of a  $H \rightarrow \gamma\gamma$  mass peak is directly related to the  $\gamma\gamma$  mass resolution  $\Delta M_{\gamma\gamma}$ . This is given by

$$\frac{\Delta M_{\gamma\gamma}}{M_{\gamma\gamma}} = \frac{1}{2} \left[ \left( \frac{\Delta E_1}{E_1} \right)^2 + \left( \frac{\Delta E_2}{E_2} \right)^2 + \left( \Delta\theta \cot \frac{\theta}{2} \right)^2 \right]^{1/2}, \quad (5.3)$$

where  $E_1$  and  $E_2$  are the energies of the two photons and  $\theta$  is the opening angle between them. It is clear from this equation that uncertainties in both energy and direction measurement would degrade the Higgs mass resolution. The energy resolution is determined by the EM calorimeter. The angular resolution is determined both by the position resolution in the EM calorimeter and by the precision of the vertex determination. GEM's calorimeter position resolution,  $\Delta x = 4.4 \text{ mm}/\sqrt{E}$ , has a negligible effect on the mass resolution.<sup>58</sup> The vertex position for a single event is well determined by the central tracker. The only issue, therefore, is how well the correct vertex can be selected in the presence of an average of 1.6 additional minimum bias events at the standard SSC luminosity plus events from previous bunch crossings.

Two approaches to determining the correct vertex are possible. The first is to use the difference in event topology resulting from the fact that Higgs production is a harder process than most of the minimum bias events and hence radiates more gluons. This leads

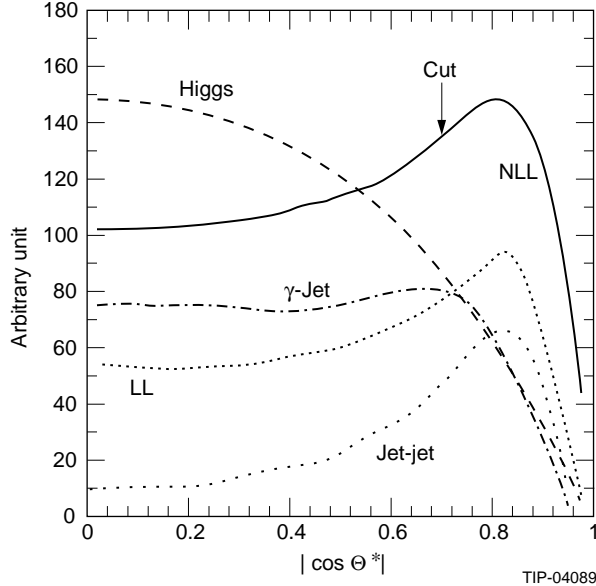


FIG. 17.  $|\cos\theta^*|$  distribution for an 80 GeV Higgs, NLL direct photon background,  $\gamma$ -jet and jet-jet background. The cut used in this analysis is  $|\cos\theta^*| < 0.7$ .

to a higher multiplicity and a higher average  $p_T$ . Selecting the vertex with the highest  $p_T$ -weighted charged multiplicity gives the correct Higgs vertex with 95% probability at the standard SSC luminosity. An independent approach is to use the pointing provided by the longitudinal segmentation of the calorimeter; using this pointing alone without any information from the central tracker degrades the mass resolution by only 20%. Using the pointing and then selecting the closest central tracker vertex gives a vertex within 5 mm 87% of the time at standard luminosity. This degrades to about 65% at  $3 \times 10^{33} \text{ cm}^{-2} \text{ s}^{-1}$ . A combination of these two methods improves the vertex-finding efficiency to 97%.<sup>51</sup> A vertex finding efficiency of 95% was assumed for this analysis.

The overall  $M_{\gamma\gamma}$  resolution varies slowly from 0.66 GeV at  $M_{\gamma\gamma} = 80 \text{ GeV}$  to 0.99 GeV at  $M_{\gamma\gamma} = 160 \text{ GeV}$ . Over the same range the Higgs natural width varies from 0.003 GeV to 0.097 GeV.

The  $H \rightarrow \gamma\gamma$  signal and the  $q\bar{q} \rightarrow \gamma\gamma$  and  $gg \rightarrow \gamma\gamma$  backgrounds were generated with PYTHIA. The next-to-leading-log (NLL) corrections both to the signal<sup>59</sup> and to the  $q\bar{q} \rightarrow \gamma\gamma$  background<sup>60</sup> have been calculated. They enhance the signal cross section by a factor  $K \approx 1.5$  and the background by a somewhat larger factor. The PYTHIA cross sections have been rescaled to these NLL results.

After cuts 1 to 4, the cut on  $\cos\theta^*$  provides an additional rejection of both direct photon and jet backgrounds and thus improves the significance. Figure 17 shows the  $\cos\theta^*$  distribution for an 80 GeV Higgs, NLL direct photon background and the  $\gamma$ -jet and jet-jet backgrounds. The improvement in significance is optimized by a cut  $|\cos\theta^*| < 0.7$ , for which an improvement of 15% is obtained.

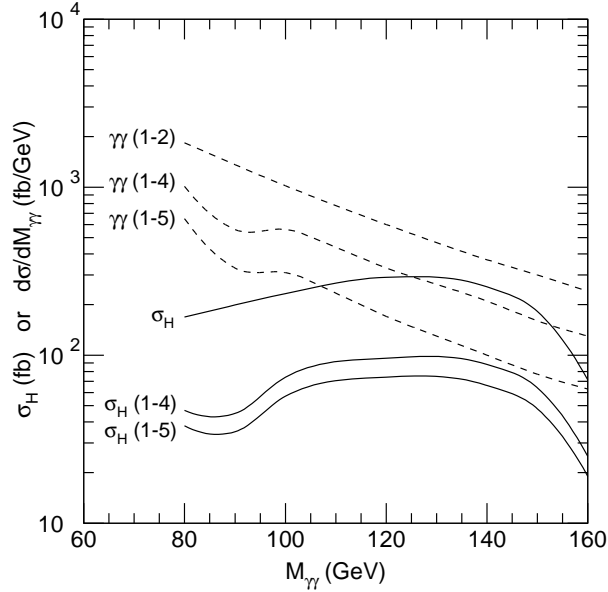


FIG. 18. Cross sections for  $H \rightarrow \gamma\gamma$  signal and  $\gamma\gamma$  background as functions of  $M_{\gamma\gamma}$ . The mass resolution is 0.66–1.0 GeV.

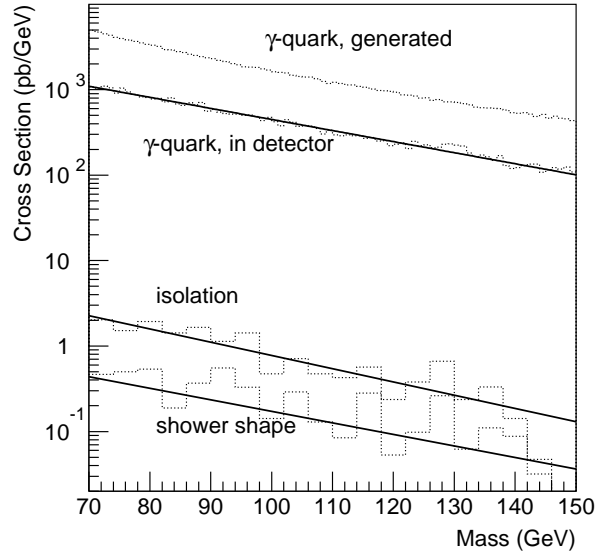


FIG. 19. Cross section for  $\gamma$ -quark jet background as a function of  $M_{\gamma\gamma}$ , showing the rejection obtained by the cuts described in the text.

Figure 18 shows the Higgs production cross section ( $\sigma_H$ ) and the cross sections after cuts 1–4 and 1–5. It also shows the rate of direct photon background after cuts 1–2, 1–4, and 1–5. The trigger efficiency for events passing all selection cuts is 98.8%. This is included in all signal and background rates. The signals are small compared to the background but still statistically significant.

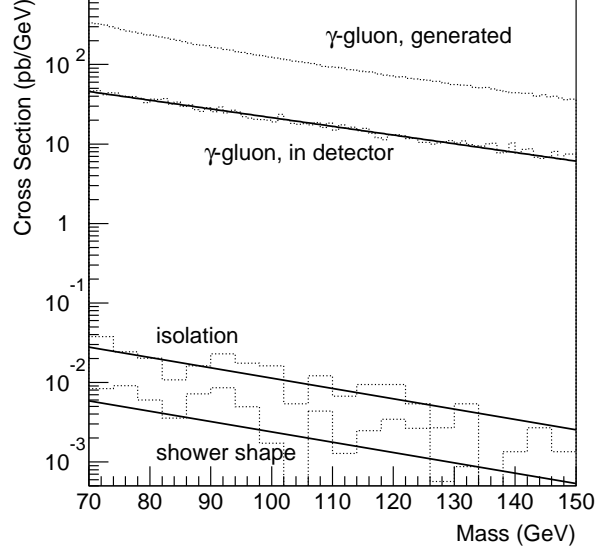


FIG. 20: Same as Fig. 19 but for  $\gamma$ -gluon jet background.

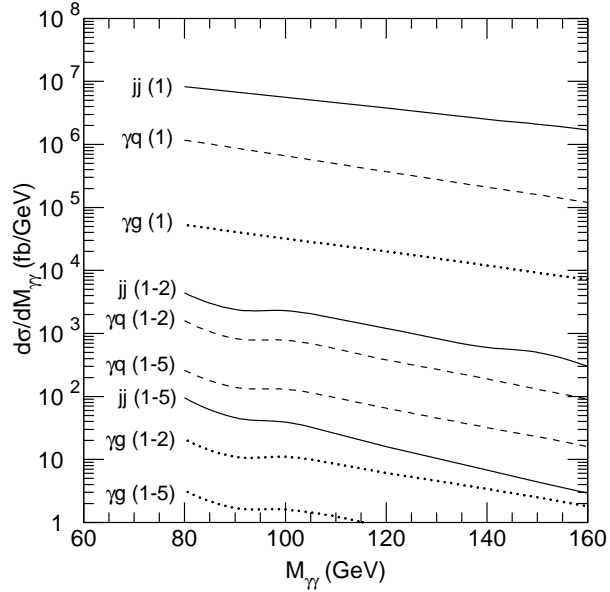


FIG. 21: Jet Background Rates for  $H \rightarrow \gamma\gamma$  after various cuts defined in the text.

QCD jets produce photons from  $\pi^0$  and  $\eta$  decays. These sometimes appear isolated and give additional backgrounds to  $H \rightarrow \gamma\gamma$ . Both  $\gamma$ -jet events giving  $\gamma$ “ $\gamma$ ” and jet-jet events producing “ $\gamma\gamma$ ” must be considered. Thus, the jet background to  $H \rightarrow \gamma\gamma$  is

$$\sigma_{\gamma\gamma} = \sigma_{\gamma\text{-jet}} \mathcal{R}(\gamma/\text{jet}) + \sigma_{2\text{-jet}} \mathcal{R}^2(\gamma/\text{jet}), \quad (5.4)$$

where  $\mathcal{R}(\gamma/\text{jet})$  is the probability for a jet to fake a photon.

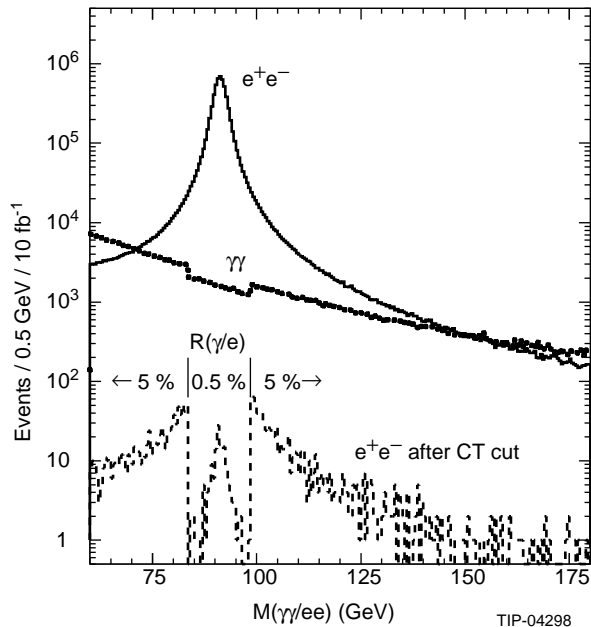


FIG. 22. Drell-Yan  $e^+e^-$  cross section after event selection cuts (dashed) and lowest order direct  $\gamma\gamma$  cross section (solid). The dots show the rate of fake photon pairs from Drell-Yan electron pairs using  $\mathcal{R}(\gamma/e) = 0.005$  near the  $Z$  and 0.05 elsewhere.

The probability  $\mathcal{R}(\gamma/\text{jet})$  was determined using a combination of **gemfast** for selecting isolated events and GEANT for simulating the shower shape cut. QED bremsstrahlung is not included, since it is properly included in the higher order QCD cross sections. Since  $\mathcal{R}(\gamma/\text{jet})$  is different for quark and gluon jets,<sup>58</sup> separate samples of about  $10^6$  events each for  $\gamma q$  and  $\gamma g$  were used to study jet rejection as a function of  $M_{\gamma\gamma}$ . Figures 19 and 20 show the cross sections for the  $\gamma$ -jet background for both quark and gluon jets as a function of  $M_{\gamma\gamma}$ . The shower shape analysis made possible by the fine sampling of the GEM calorimeter improves the rejection by about a factor of 4 per photon over isolation alone. Since the jet-jet cross section is about  $10^8$  times the  $\gamma\gamma$  one, it is not possible to generate enough jet-jet events to simulate the background directly. Instead,  $gg$ ,  $qg$  and  $qq$  events were generated at the parton level, and the probabilities of jets faking photons taken from these figures were used to calculate the background.

Figure 21 shows the cross sections for the jet backgrounds after cut 1 at the parton level (including a  $K$ -factor of 1.5), after cuts 1–2, 1–3 and after all cuts 1–5. The  $\gamma$ -gluon background is reduced to a negligible level compared to the NLL direct photon background. The 2 jet background (which is dominated by gluon jets) is reduced to around 15% of the NLL direct photon background at 80 GeV. The  $\gamma q$  background, however, remains 40% of the NLL direct photon background there. Since a factor of two increase in all the jet backgrounds reduces the significance by only 16%, GEM’s searches in the  $H \rightarrow \gamma\gamma$  channel are not very sensitive to the QCD jet rejection.

Drell-Yan  $e^+e^-$  pairs can give a background for  $H \rightarrow \gamma\gamma$  if the central tracker fails

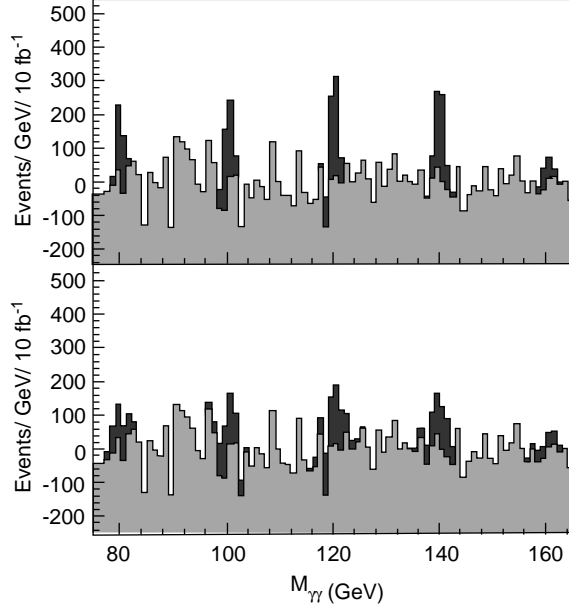


FIG. 23. Higgs mass peaks over subtracted background, obtained with  $10 \text{ fb}^{-1}$ , for  $H \rightarrow \gamma\gamma$  searches with  $M_H = 80, 100, 120, 140$  and  $160 \text{ GeV}$ . Part (a) corresponds to  $a = 6/8.5\%$  in the barrel/endcaps and  $b = 0.4\%$ , and part (b) to  $a = 14/17\%$  in the barrel/endcaps and  $b = 1\%$ . The GEM photon identification algorithm is used in both cases; see Section 5.1

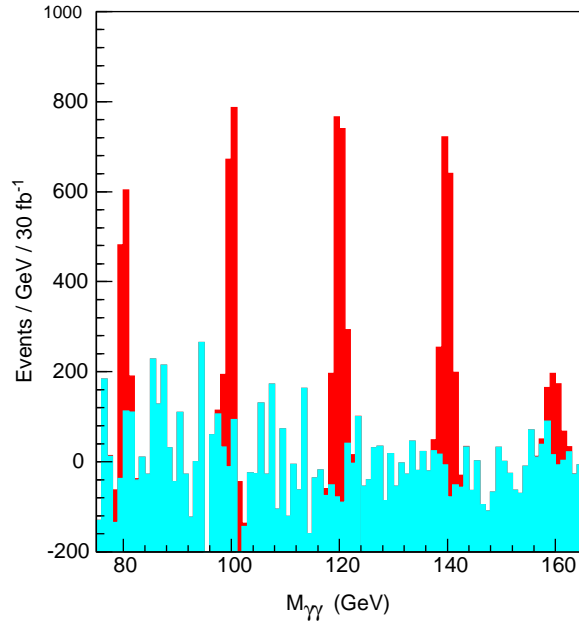


FIG. 24. Higgs mass peaks over subtracted background, obtained with  $30 \text{ fb}^{-1}$ , for  $H \rightarrow \gamma\gamma$  searches with  $M_H = 80, 100, 120, 140$  and  $160 \text{ GeV}$  for the GEM detector.

to identify both charged tracks. Figure 22 shows the invariant mass distribution of Drell-Yan  $e^+e^-$  after event selection cuts and the lowest order direct photon background. The Drell-Yan cross section is about 300 times larger than the direct photon background at

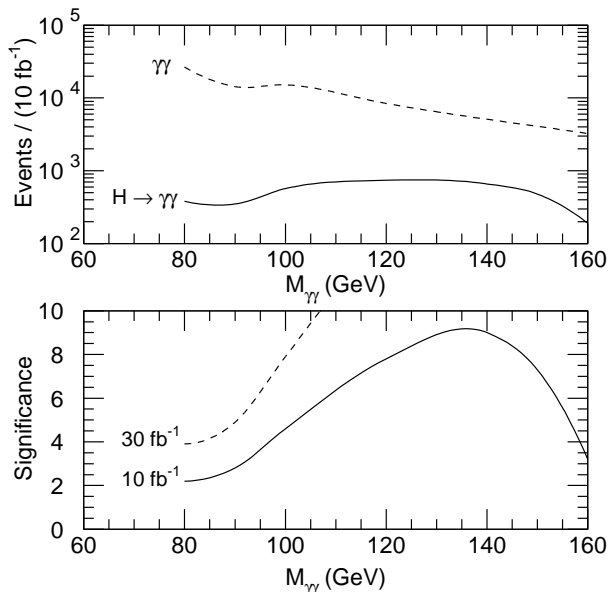


FIG. 25: Number of events and significance for  $H \rightarrow \gamma\gamma$  including all acceptances.

the  $Z$ -mass peak, but comparable elsewhere. A GEANT simulation was performed for the central tracker to estimate the rate of electrons faking photons,  $\mathcal{R}(\gamma/e)$ . If one simply looks for hits in the central tracker forming a line, the photon acceptance is found to be 83% for  $\mathcal{R}(\gamma/e) = 0.005$  and 96% for  $\mathcal{R}(\gamma/e) = 0.05$ . If one restricts the track to lie in a road defined by the pointing resolution of the calorimeter, then the photon acceptance improves to 86% for  $\mathcal{R}(\gamma/e) = 0.002$ . If one uses the vertex found to further restrict the road, then a photon acceptance of 91% can be achieved with the same rejection. In what follows, we use only the first method, since it allows adequate rejection at all masses, as indicated in Fig. 22.

Figure 23 shows the reconstructed  $H \rightarrow \gamma\gamma$  mass peaks after subtracting the background, for an integrated luminosity of  $10 \text{ fb}^{-1}$ , and  $M_H = 80, 100, 120, 140$  and  $160 \text{ GeV}$ . Figure 24 shows the corresponding peaks after  $30 \text{ fb}^{-1}$ . Figure 25 shows the number of signal and background events after all cuts, and the resulting signal significance using a  $\pm 2\Delta M_H$  mass bin. With  $10 \text{ fb}^{-1}$ , GEM could discover a Higgs boson, using this mode alone, for  $110 \lesssim M_H \lesssim 150 \text{ GeV}$ . With  $30 \text{ fb}^{-1}$ , using this mode alone, it could extend the discovery reach down to about  $90 \text{ GeV}$  and up to  $160 \text{ GeV}$ . While the heavier masses can also be found in the  $ZZ^*$  mode, the  $\gamma\gamma$  branching ratio is important to distinguish the minimal Standard Model Higgs boson from nonminimal ones.

### 5.2.2. $H(t\bar{t}/W) \rightarrow \gamma\gamma\ell X$ Searches for $80 \text{ GeV} < M_H < 140 \text{ GeV}$

The processes  $Ht\bar{t} \rightarrow \gamma\gamma\ell X$  and  $HW \rightarrow \gamma\gamma\ell X$  are complementary to the inclusive

$H \rightarrow \gamma\gamma$ , providing essential confirmation.<sup>61</sup> As shown in Fig. 18, the signal cross section for the sum of these two channels is of the order of few fb, but the isolated lepton tag and photon identification cuts leads to smaller backgrounds, so that the signal-to-background ratio is large. In these associated production channels, most of the effects of detector resolutions on the reconstructed mass resolution discussed previously remain applicable. With a charged lepton in the final state, however, the central tracker is able to determine the Higgs vertex unambiguously.

The main backgrounds to  $H(t\bar{t}/W) \rightarrow \gamma\gamma\ell X$  searches are:

1.  $t\bar{t}\gamma\gamma$  or  $b\bar{b}\gamma\gamma \rightarrow \ell\gamma\gamma$ .
2.  $q\bar{q}' \rightarrow W\gamma\gamma \rightarrow \ell\gamma\gamma$ , where both photons are radiated from quarks.
3.  $q\bar{q}' \rightarrow W\gamma \rightarrow \ell\gamma\gamma$ , where one photon is radiated from the outgoing charged lepton.
4.  $q\bar{q}/gg \rightarrow Z\gamma \rightarrow \ell^+\ell^-\gamma\gamma$ , where the second photon is radiated from the outgoing charged lepton.
5.  $q\bar{q}/gg \rightarrow Z\gamma \rightarrow e\text{“}\gamma\text{”}\gamma$ , where the fake photon is from misidentification of the electron.
6.  $t\bar{t} \rightarrow \text{“}\gamma\gamma\text{”}\ell X$ , where both photons are fakes arising from jet fragmentation.

Since all the higher order QCD corrections to the signal and backgrounds have not been computed, leading order cross sections are used for this entire analysis. While  $t\bar{t}$  is initially very much larger, all the backgrounds turn out to be comparable after the cuts described below.

Not all of these background processes are included in PYTHIA, so they were calculated using a combination of generators. For processes 1 and 2, the initial hard scattering was generated using PAPAGENO 3.6.<sup>31</sup> Initial and final state parton radiation, hadronization and decays were then generated using PYTHIA. All the final state photon radiation for processes 3, 4 and 5 was generated using PYTHIA with the QED radiation option turned on. Since the process  $gg \rightarrow Z\gamma$  is not available in either PYTHIA or PAPAGENO,  $q\bar{q} \rightarrow Z\gamma$  was increased by 20%.<sup>62</sup> The  $t\bar{t}$  background (process 6) was generated with PYTHIA with QED radiation turned on. The study was carried out with  $2.6 \times 10^6$  events. Only 3 events survived all cuts; none of them contained two radiated photons. The  $b\bar{b}\gamma\gamma$  background was also simulated, and it is small compared to the  $t\bar{t}$  background after isolation cuts.

The following cuts were made to reject the backgrounds:

1.  $|\eta_\ell| < 2.5$  and  $p_T^\ell > 20$  GeV.
2.  $|\eta_\gamma| < 2.5$  and  $p_T^\gamma > 20$  GeV.
3. Photon and lepton isolation with  $E_T^{\text{cut}} = 5$  GeV and  $R = 0.45$  and  $0.3$  for photon and lepton respectively.
4. Photon and lepton identification by shower shape and track matching.

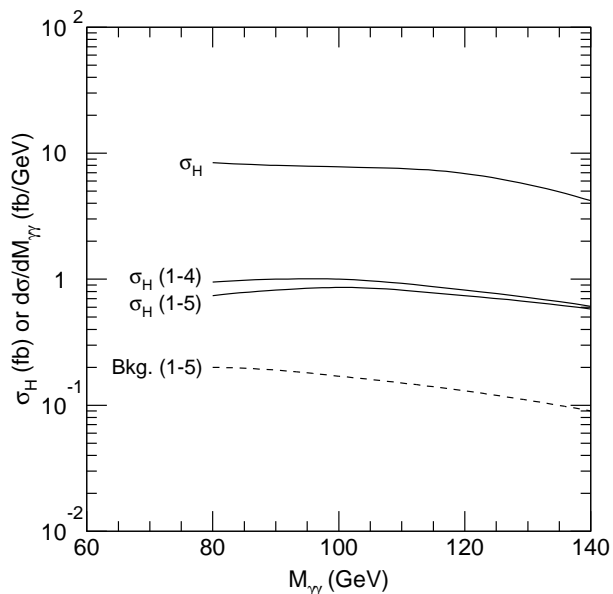


FIG. 26. Signal and background for  $H(tt/W) \rightarrow \gamma\gamma\ell X$  after the cuts described in the text.

5.  $p_T^{\gamma\gamma} > 40 \text{ GeV}$ .

The first two cuts ensured that the lepton and photons could be detected. Cuts 3 and 4 identify the photons and lepton and reject jet backgrounds. Finally, cut 5 was found to reject the backgrounds, especially  $t\bar{t}$  listed above. It reduces the background by a factor of 2 to 3 while losing only 20% of the signal. The trigger efficiency for events passing these selection cuts is 99%.

Figure 26 shows the Higgs production cross section ( $\sigma_H$ ) and the cross sections after event selection cuts 1–4 and 1–5 together with the total background rate after all cuts as a function of mass. The largest backgrounds are the fake  $\gamma\gamma$  pairs from  $t\bar{t}$  production and the QED radiation  $Z\gamma \rightarrow \ell^+\ell^-\gamma\gamma$ . A  $Z$ -mass veto improves the rejection of the latter background, but it does not improve the significance.

Figure 27 shows the  $\gamma\gamma$  invariant mass spectrum collected in  $30 \text{ fb}^{-1}$  with Higgs signals of 80, 100, 120 and 140 GeV superimposed on the sum of all backgrounds. Figure 28 shows the significance for the  $H(tt/W) \rightarrow \gamma\gamma\ell X$  search with integrated luminosity of 10 and  $30 \text{ fb}^{-1}$ . Although the numbers of signal and background events are small, this process provides higher significance than the inclusive  $H \rightarrow \gamma\gamma$  at very low masses. The combination of this channel and the inclusive  $H \rightarrow \gamma\gamma$  provides a more robust search for low mass Higgs bosons than either one alone.

### 5.2.3. $H \rightarrow ZZ^* \rightarrow \ell^+\ell^-\ell^+\ell^-$ Searches for $140 \text{ GeV} < M_H < 2M_Z$

The  $H \rightarrow ZZ^{(*)} \rightarrow \ell^+\ell^-\ell^+\ell^-$  decay provides the cleanest Higgs signal. Because of the

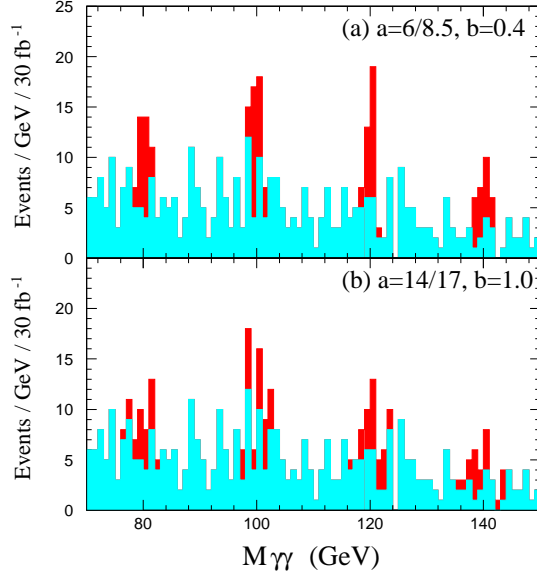


FIG. 27. Two-photon mass peaks for  $H(t\bar{t}/W) \rightarrow \ell\gamma\gamma X$  (black area) over sum of all backgrounds (gray area), for an integrated luminosity of  $30 \text{ fb}^{-1}$  and  $M_H = 80, 100, 120$  and  $140 \text{ GeV}$ .

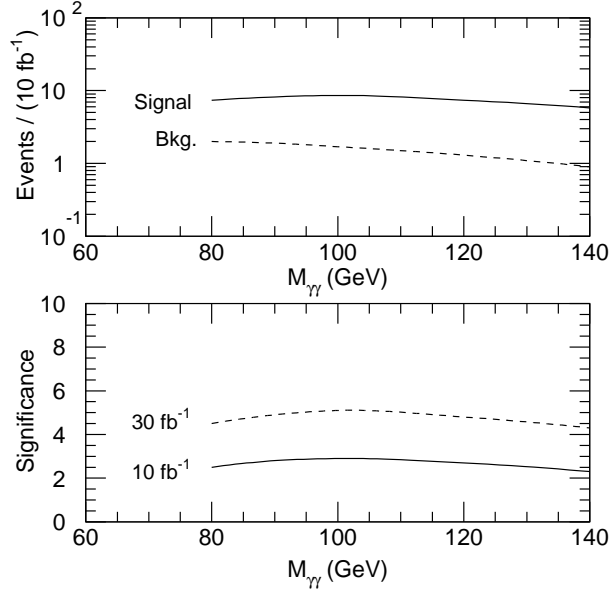


FIG. 28. Number of events and significance for  $H(t\bar{t}/W) \rightarrow \ell\gamma\gamma X$  for various masses and integrated luminosities. Signal and background are integrated over  $\pm 2\Delta M_H$ .

four isolated leptons in the final state, most of the QCD background can be rejected by an

isolation cut. For a Higgs mass larger than  $2M_Z$ , both  $\ell^+\ell^-$  pairs have an invariant mass of  $M_Z$ , so a mass constraint can also be used to reject background. If the Higgs mass is less than  $2M_Z$ , one (or both)  $Z$ -bosons are off the mass shell. In either case, good mass resolution is important for rejecting backgrounds.

The background processes considered are:

1.  $ZZ/ZZ^* \rightarrow \ell^+\ell^-\ell^+\ell^-$ .
2.  $Q\bar{Q}Z \rightarrow \ell^+\ell^-\ell^+\ell^- + X$ , where  $Q = b$  or  $t$ .
3.  $t\bar{t} \rightarrow W^+bW^-\bar{b}$ , in which the two  $W$ -bosons decay semileptonically and the  $b$ -jets give isolated leptons.

The  $ZZ/ZZ^* \rightarrow \ell^+\ell^-\ell^+\ell^-$  background is irreducible. Since the cross section of  $gg \rightarrow ZZ^*$  is not yet available in either PYTHIA or ISAJET, its contribution was accounted for by multiplying the contribution of  $q\bar{q} \rightarrow ZZ^*$  by 1.65.<sup>62</sup>

The following cuts were used to reject the other backgrounds:

1.  $|\eta^\ell| < 2.5$  and  $p_T^\ell > 10$  GeV. For electrons, the region  $1.01 < |\eta| < 1.16$  was excluded.
2. Lepton isolation with  $R = 0.35$  and  $E_T^{\text{cut}} = 5$  GeV; see Section 5.1.
3. Lepton identification and track matching.
4.  $10 \text{ GeV} \leq M_{\ell\ell}^{(l)} \leq 100 \text{ GeV}$  and  $70 \text{ GeV} \leq M_{\ell\ell}^{(h)} \leq 100 \text{ GeV}$  to suppress the continuum background, where  $M_{\ell\ell}^{(l)}$  and  $M_{\ell\ell}^{(h)}$  are the low and high invariant masses of two  $\ell^+\ell^-$  pairs.

The isolation,  $p_T$ , and mass cuts help reject the heavy flavor background. The trigger efficiency for events passing these selection cuts is higher than 98% for the four-electron mode and 99% for the other two modes.

Table 5 shows the cross section after event selections ( $\sigma_{\text{accep}}$ ) and the corresponding background rate for the various  $H \rightarrow \ell^+\ell^-\ell^+\ell^-$  channels. The integrated luminosity is  $10 \text{ fb}^{-1}$ . While the mass resolution is excellent in the four-electron channel, it is not as good in the muon channels because of multiple scattering of the relatively low-energy muons in the second muon chamber superlayer. (This is an instance in which simulations directly influenced the detector. Changes were made to the muon system design following the TDR work to increase its acceptance and resolution for this four-muon process.) The significance for all channels combined is also listed in Table 5. Using all the four-lepton channels, GEM can discover a Higgs boson in this mass range with an integrated luminosity of  $10 \text{ fb}^{-1}$ . The most difficult mass is 170 GeV where the signal is only  $5.7\sigma$ . Figure 29 shows the  $e^+e^-e^+e^-$ ,  $\mu^+\mu^-\mu^+\mu^-$ , and  $\ell^+\ell^-\ell^+\ell^-$  invariant mass spectra collected in  $30 \text{ fb}^{-1}$  for  $M_H = 140, 150, 160, 170$  and  $180$  GeV superimposed on the sum of all backgrounds. The increased integrated luminosity makes even the peak at 170 GeV unambiguous.

Table 5. Signal and Background for  $H \rightarrow ZZ^* \rightarrow \mu^+\mu^-\mu^+\mu^-$  and  $H \rightarrow ZZ^* \rightarrow \ell^+\ell^-\ell^+\ell^-$  for an integrated luminosity of  $10 \text{ fb}^{-1}$ . The signal cross section after cuts is  $\sigma_{\text{accep}}$ .

$M_H$ (GeV)	140	150	160	170	180
$H \rightarrow e^+e^-e^+e^-$					
$\Delta M_H$ (GeV)	1.05	1.06	1.13	1.23	1.33
$\sigma_{\text{accep}}$	1.2	1.7	.86	.62	1.6
Background (fb/GeV)	.025	.025	.025	.025	.040
$H \rightarrow \mu^+\mu^-\mu^+\mu^-$					
$\Delta M_H$ (GeV)	1.59	1.62	1.73	1.84	2.22
$\sigma_{\text{accep}}$ (fb)	.81	1.1	.56	.36	.92
Background (fb/GeV)	.016	.016	.016	.016	.026
$H \rightarrow e^+e^-\mu^+\mu^-$					
$\Delta M_H$	1.36	1.46	1.56	1.71	1.77
$\sigma_{\text{accep}}$ (fb)	1.9	2.6	1.4	0.89	2.4
Background (fb/GeV)	.038	.038	.038	.038	.062
$H \rightarrow \ell^+\ell^-\ell^+\ell^-$					
Significance	11	13	8.1	5.7	10

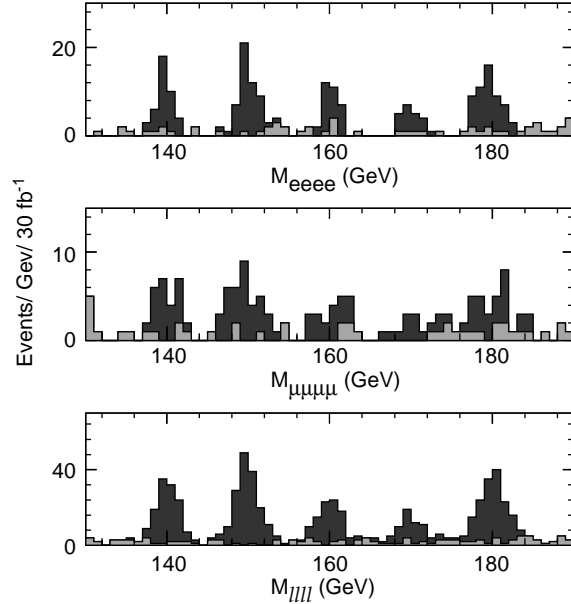


FIG. 29. Higgs mass peaks for  $H \rightarrow ZZ^* \rightarrow \ell^+\ell^-\ell^+\ell^-$  over the sum of all backgrounds plotted for an integrated luminosity of  $30 \text{ fb}^{-1}$ , and  $M_H = 140, 150, 160$  and  $170 \text{ GeV}$ . (a) Four electrons. (b) Four muons. (c) All leptons.

#### 5.2.4. $H \rightarrow ZZ \rightarrow \ell^+\ell^-\ell^+\ell^-$ Searches for $2M_Z < M_H < 800 \text{ GeV}$

Table 6. Signal and background for  $H \rightarrow ZZ \rightarrow \ell^+\ell^-\ell^+\ell^-$  for an integrated luminosity of  $10 \text{ fb}^{-1}$ .

$M_H$ (GeV)	200	400	600	800
Signal (fb)				
$\sigma_H$	85	56	16	5.3
Mass Bin (GeV)	$\pm 4.7$	350–450	500–800	600–1200
$\sigma_{\text{accep}}$	21	14	4.3	1.5
Background (fb)				
$ZZ$	3.0	2.3	1.0	.6
Significance				
Significance	38	28	9.7	4.7

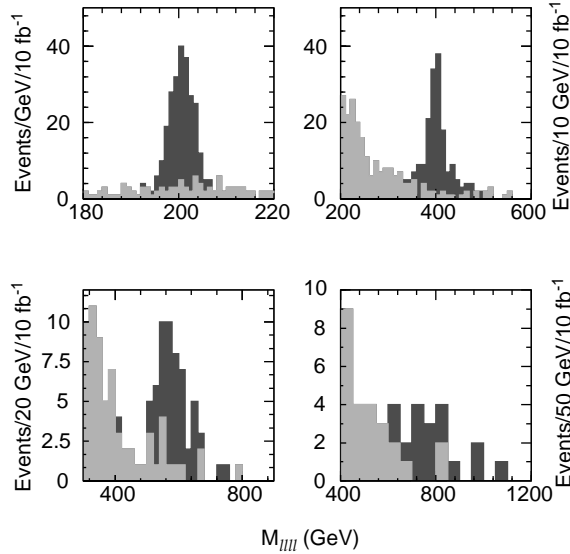


FIG. 30. Higgs mass peaks and background for  $H \rightarrow ZZ \rightarrow \ell^+\ell^-\ell^+\ell^-$  for an integrated luminosity of  $10 \text{ fb}^{-1}$ . (a)  $M_H = 200 \text{ GeV}$ , (b)  $400 \text{ GeV}$ . (c)  $600 \text{ GeV}$ . (d)  $800 \text{ GeV}$ .

For a heavy Higgs decaying into  $\ell^+\ell^-\ell^+\ell^-$ , PYTHIA was used to generate the signal and the  $ZZ$  background. All other backgrounds are negligible. The event selection cuts were taken to be:

1.  $|\eta^\ell| < 2.5$  and  $p_T^\ell > 10 \text{ GeV}$ .
2. Lepton isolation with  $R = 0.3$  and  $E_T^{\text{cut}} = 5 \text{ GeV}$ .
3. Lepton identification and track matching.
4. At least one  $Z$  with  $p_T > \frac{1}{4} \sqrt{M_{ZZ}^2 - 4M_Z^2}$ .
5.  $|M_{\ell\ell} - M_Z| < 10 \text{ GeV}$  for both lepton pairs.

Cuts 1, 2, 3, and 5 are self-explanatory. If the transverse momentum of the  $ZZ$  system is neglected, then cut 4 requires  $\sin\theta^* > 0.5$  and so reduces the more peripheral  $q\bar{q} \rightarrow ZZ$  background. The trigger efficiency for events passing these selection cuts is higher than 99%.

Table 6 shows the production cross section ( $\sigma_H$ ) and the cross section after event selection cuts ( $\sigma_{\text{accep}}$ ) for  $M_H = 200, 400, 600$  and  $800$  GeV. (A Higgs mass of  $800$  GeV is somewhat greater than the “triviality” bound,<sup>15</sup> but we consider it because it is the greatest mass at which the Higgs still appears to give a distinct resonance. Such a mass is possible, but it will be accompanied by unspecified new physics at or below a few TeV.) The rate of the  $ZZ$  background and the combined significance are also listed for an integrated luminosity of  $10 \text{ fb}^{-1}$ . For such a data sample, discovery of heavy Higgs bosons in the  $\ell^+\ell^-\ell^+\ell^-$  modes will be possible for all masses below about  $700$  GeV. For the heaviest masses one would seek confirmation of these four-lepton signals in other channels, as we discuss next. We also expect that GEM’s capabilities at ultrahigh luminosity (see Section 5.6) will permit the discovery of a very heavy Higgs in the four-lepton channel in about one year with a data sample of order  $100 \text{ fb}^{-1}$ .

Figure 30 shows the  $\ell^+\ell^-\ell^+\ell^-$  invariant mass spectra collected in  $10 \text{ fb}^{-1}$  for  $M_H = 200, 400, 600$  and  $800$  GeV superimposed on the background. While the  $800$  GeV peak looks ragged, the calculated statistical significance is  $4.7\sigma$  in  $10 \text{ fb}^{-1}$ . There is also a systematic uncertainty caused by lack of knowledge of the shape of the background. This is discussed at the end of the following subsection.

### 5.2.5. $H \rightarrow ZZ \rightarrow \ell^+\ell^-\nu\bar{\nu}$ Searches for $M_H = 800$ GeV

The branching ratio for  $H \rightarrow ZZ \rightarrow \ell^+\ell^-\nu\bar{\nu}$  is six times that for  $H \rightarrow ZZ \rightarrow \ell^+\ell^-\ell^+\ell^-$ . Since one  $Z$  decays to  $\nu\bar{\nu}$ , the signature is a high- $p_T$   $Z \rightarrow \ell^+\ell^-$  plus missing energy, and the mass of the Higgs boson cannot be directly reconstructed. The total signal cross section is  $32 \text{ fb}$ .

The following backgrounds were considered:

1.  $q\bar{q}/gg \rightarrow ZZ$ ; the cross section is  $73 \text{ fb}$  for  $p_T^Z > 150 \text{ GeV}$ .
2.  $q\bar{q} \rightarrow Zg$  and  $qg \rightarrow Zq$ , with  $Z \rightarrow \ell^+\ell^-$ ; the cross section is  $66 \text{ pb}$  for  $p_T^Z > 150 \text{ GeV}$  before any  $\cancel{E}_T$  cut.
3.  $q\bar{q}, gg \rightarrow t\bar{t}$ , with  $t \rightarrow b\ell\nu$ ; the cross section is  $380 \text{ pb}$  before cuts.

To separate the signal from these backgrounds, events with an  $e^+e^-$  or  $\mu^+\mu^-$  pair were selected as follows:

1.  $|\eta^\ell| < 2.5$  and  $p_T^\ell > 20 \text{ GeV}$  for each lepton.
2. Lepton isolation with  $R = 0.3$  and  $E_T^{\text{cut}} = 5 \text{ GeV}$ .
3. Lepton identification and track matching.

Table 7: Signal and Background (fb) for  $H \rightarrow \ell^+ \ell^- \nu \bar{\nu}$

$e^+e^-\nu\bar{\nu}$ Channel				
	Signal	$ZZ$	$Z + jets$	$t\bar{t}$
$\sigma_H$	16.0	36.7	$3.3 \times 10^4$	$2.0 \times 10^5$
After cuts 1–4	9.5	13.8	$1.2 \times 10^4$	53.5
After cuts 1–5	7.4	4.2	$3.1 \times 10^3$	0.36
After cuts 1–6	6.2	3.2	2.2	0.0
$\mu^+\mu^-\nu\bar{\nu}$ Channel				
	Signal	$ZZ$	$Z + jets$	$t\bar{t}$
After cuts 1–4	6.5	9.4	$8.1 \times 10^3$	36.2
After cuts 1–5	5.0	2.9	$2.1 \times 10^3$	0.24
After cuts 1–6	4.2	2.2	1.5	0.0

4.  $|M_{\ell\ell} - M_Z| < 10 \text{ GeV}$ .
5.  $E_T^Z > 250 \text{ GeV}$ .
6.  $\cancel{E}_T > 250 \text{ GeV}$ .

Cuts 5 and 6 are primarily intended to reject the large  $Z + jets$  background; see Fig. 31. The trigger efficiency for events passing all selection cuts is higher than 99%. Table 7 lists the cross sections after cuts 1–4, 1–5, and 1–6, for the signal and background in the  $e^+e^-\nu\bar{\nu}$  and  $\mu^+\mu^-\nu\bar{\nu}$  channels.

Figure 32 shows the reconstructed transverse mass,  $M_T^2 = 2E_T^Z \cancel{E}_T (1 - \cos \Delta\phi)$ , where  $E_T^Z$  is the transverse energy of the  $Z$  and  $\Delta\phi$  is the azimuthal angle between the direction of the  $Z$ -boson and the  $\cancel{E}_T$ -vector. This distribution is not sensitive to the degradation of the  $\cancel{E}_T$  resolution that results from adding to the calorimeter response a 1% nongaussian tail with twice the normal width (see Section 4.3). There are 105 signal events over a total background of 91 for an integrated luminosity of  $10 \text{ fb}^{-1}$ . Since the signal and background distributions are similarly shaped and the signal to background ratio is only 1.15:1, this cannot be regarded as a convincing discovery channel. A knowledge of the  $ZZ$  continuum background to  $\sim 25\%$  would serve to give a  $5\sigma$  systematic-limited significance. This knowledge of the  $ZZ$  background should be achievable by comparison with  $WZ$  and  $Z + jets$  production. The statistical  $4.7\sigma$  significance of the four-lepton signal is reduced to  $4.2\sigma$  by the same background uncertainty. Combining the  $llll$  and  $ll\nu\nu$  channels with Gaussian statistics gives a  $6.6\sigma$  signal for  $10 \text{ fb}^{-1}$ .

### 5.2.6. $H \rightarrow ZZ \rightarrow \ell^+ \ell^- jj$ Searches for $M_H = 800 \text{ GeV}$

The branching ratio for  $H \rightarrow ZZ \rightarrow \ell^+ \ell^- jj$  for  $\ell = e$  and  $\mu$  is approximately 20 times

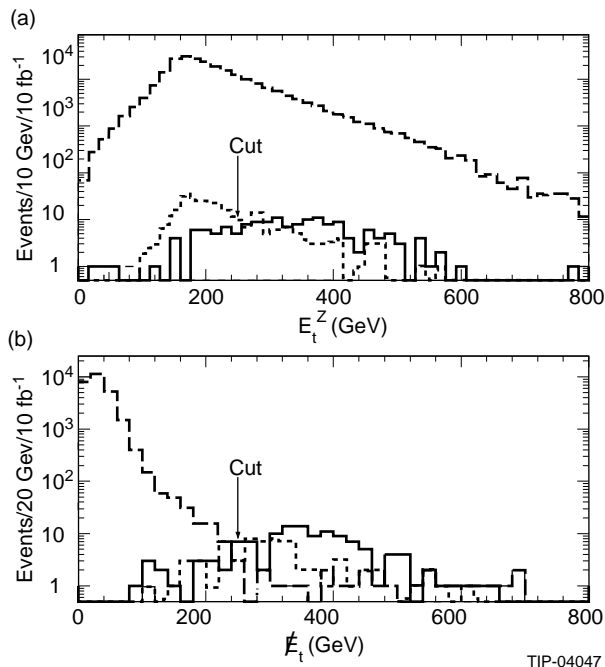


FIG. 31. Distributions for an 800 GeV  $H \rightarrow \ell^+ \ell^- \nu \bar{\nu}$  signal (solid),  $ZZ$  background (dots), and  $Z$  + jets background (dash) for  $10 \text{ fb}^{-1}$ . The  $t\bar{t}$  background is small. (a) Transverse energy of the reconstructed  $Z$ . (b) Missing transverse energy ( $\cancel{E}_T$ ).

higher than that into all the  $\ell^+ \ell^- \ell^+ \ell^-$  modes. For  $M_H = 800 \text{ GeV}$ , the cross section is  $110 \text{ fb}$ . The signal-to-background ratio, however, is much worse than in the four-lepton channel because of the large background from  $Z$  + jets production. In addition, since the width of an 800 GeV Higgs is  $270 \text{ GeV}$ , the signal will be seen only as a broad excess of  $ZZ$  pairs over the background.

The following backgrounds were studied in this analysis:

1.  $ZW$  or  $ZZ$  with one  $Z \rightarrow e^+ e^-$  or  $\mu^+ \mu^-$ .
2.  $Z$  + jets with  $Z \rightarrow e^+ e^-$  or  $\mu^+ \mu^-$ .
3.  $t\bar{t}$  with  $t \rightarrow bW$  and  $W \rightarrow e\nu$  or  $\mu\nu$ .

The irreducible  $ZZ$  background has a production cross section of  $130 \text{ fb}$ , for  $p_T^Z > 200 \text{ GeV}$ . The  $Z$  + jets background has a much larger rate of  $27 \text{ pb}$  for  $p_T^Z > 200 \text{ GeV}$ . The  $Z$ -mass constraint and high  $p_T$  of leptons and jets were used to reduce this background. (The possibility of tagging forward jets and vetoing on central jets to enhance the signal-to-background ratio is discussed below.) The cross section for the  $t\bar{t}$  background with semileptonic decays to  $e^+ e^- + X$  and  $\mu^+ \mu^- + X$  is  $380 \text{ pb}$  before the  $Z$ -mass constraint is imposed. A sample of  $1.5 \times 10^6$  events was generated for this background. It was largely eliminated by  $p_T$  and isolation cuts and the  $Z$ -mass constraint.

Leptons were selected as follows:

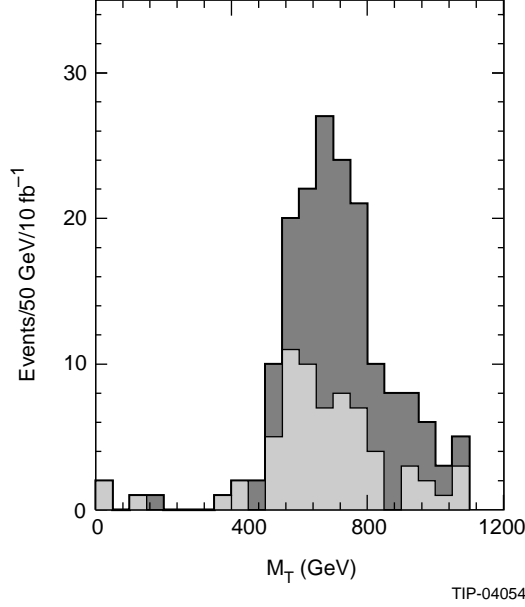


FIG. 32. Transverse mass  $M_T$  of an 800 GeV Higgs signal for  $H \rightarrow ZZ \rightarrow \ell^+ \ell^- \nu \nu$  (black area) and sum of all backgrounds (gray area), obtained for an integrated luminosity of  $10 \text{ fb}^{-1}$ .

1.  $|\eta^\ell| < 2.5$  and  $p_T^\ell > 70 \text{ GeV}$  for each lepton.
2. Lepton isolation with  $R = 0.3$  and  $E_T^{\text{cut}} = 5 \text{ GeV}$ .
3. Lepton identification and track matching.
4.  $|M_{\ell\ell} - M_Z| < 10 \text{ GeV}$ .
5.  $p_T^{\ell\ell} > 230 \text{ GeV}$ .

The hadronically-decaying  $Z$ -boson was reconstructed with the following algorithm:

1. Find all jets at  $|\eta| < 2.5$  using a large clustering cone,  $R = 0.9$ .
2. Find all jets with a small cone,  $R = 0.3$ , and match these narrow jets with those found using the larger cone.
3. Require the highest  $p_T$  jet found with  $R = 0.9$  to have  $p_T > 250 \text{ GeV}$  and to be composed of two jets found with  $R = 0.3$ , each having  $p_T > 80 \text{ GeV}$ .
4. Reconstruct the mass  $M_{jj}$  of the highest- $p_T$  dijet with  $R = 0.9$ , and require that  $|M_{jj} - M_Z| < 15 \text{ GeV}$ .

The trigger efficiency for events passing all these selection cuts is higher than 99%.

Figure 33 shows the reconstructed dijet mass  $M_{jj}$  for the signal and backgrounds, and the dijet mass cut is indicated. Note that the background has been multiplied by 0.2 in this plot. The mass resolution is about 9 GeV. Table 8 shows the cross sections for signal and backgrounds after the lepton and jet cuts for  $600 < M_{\ell\ell jj} < 1000 \text{ GeV}$ .

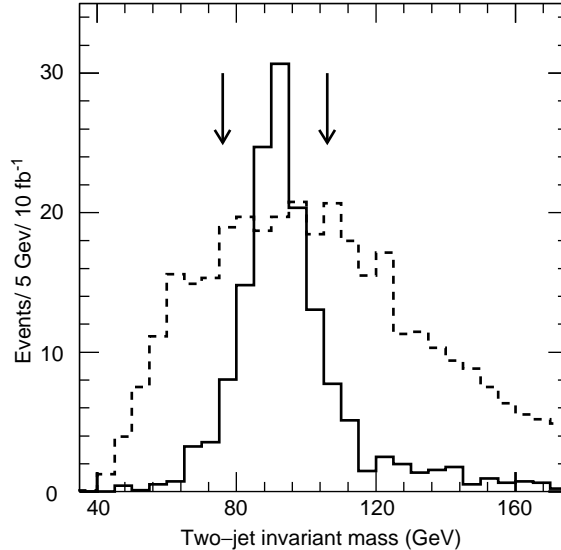


FIG. 33. Dijet invariant mass distribution for  $H \rightarrow ZZ \rightarrow \ell^+\ell^-jj$  for  $M_H = 800$  GeV (solid) and sum of all backgrounds (dashed), obtained for an integrated luminosity of  $10 \text{ fb}^{-1}$ . The background is multiplied by a factor of 0.2. to facilitate comparison of the shapes.

Table 8. Signal and background cross sections (fb) for  $H \rightarrow ZZ \rightarrow \ell^+\ell^-jj$  for  $10 \text{ fb}^{-1}$ . The invariant mass  $M_{\ell\ell jj}$  signal region is 600 to 1000 GeV.

Cut	Higgs	$t\bar{t}$	$Z$ +jets	$ZW/ZZ$
After lepton cuts	41	130	3240	20
After jet cuts	12	0.5	65	1.5
Within $600 < M_{\ell\ell jj} < 1000$	11	0.3	42	0.8

The invariant mass  $M_{\ell\ell jj}$  of the  $Z$ -jet system is shown in Fig. 34. The signal and background events passing all these cuts are 110 and 430 respectively for  $10 \text{ fb}^{-1}$ . The signal and background have a very similar shape, with no recognizable peak in the mass spectrum. Since the signal is 25% of the background, the latter must be known to better than 5% to achieve a  $5\sigma$  significance. Thus, this mode cannot be regarded as a discovery channel for the Higgs.

The possibility of tagging forward jets to enhance the signal-to-background was studied.<sup>63,51</sup> For this, a segmentation of the forward calorimeter of  $\Delta\eta \times \Delta\phi = 0.3 \times 0.3$  was assumed; similar results were obtained with  $0.2 \times 0.2$ . A resolution of  $100\%/\sqrt{E} \oplus 5\%$  was used to smear the hadronic energies. One forward jet was required in  $2.5 < |\eta| < 4.5$  with  $E > 2 \text{ TeV}$  and  $p_T > 50 \text{ GeV}$ . After the  $\ell\ell$  jet jet cuts described above, the signal was reduced to 24 events on a background of 32. Again, the shape of signal and background were similar, so there is no significant advantage in tagging a single forward jet. Requiring two tagged forward jets is expected to reduce the signal and backgrounds to a level

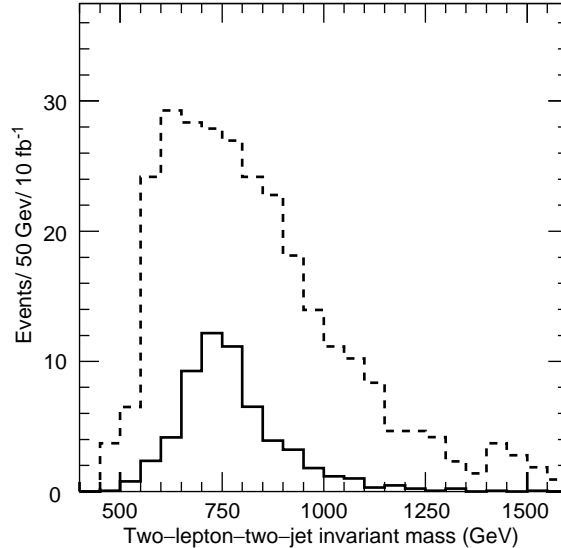


FIG. 34. Invariant mass distribution  $M_{\ell^+\ell^-jj}$  for 800 GeV  $H \rightarrow ZZ \rightarrow \ell^+\ell^-jj$  signal (solid) and sum of all backgrounds (dashed), obtained for an integrated luminosity of  $10 \text{ fb}^{-1}$ .

comparable with the four charged lepton channel and, so, will not be of help. Finally, a central jet veto was found not to be useful after the high- $p_T$  cuts on the jets from  $Z$  decay were imposed.

### 5.3. Heavy Flavor Physics

As we have emphasized, while the characteristic energy of electroweak symmetry breaking lies within reach of multi-TeV hadron colliders such as the SSC and LHC, the scales of flavor symmetry and the interactions that break it are unknown; they may be near 1 TeV or much higher. Nevertheless, searching for the origin of flavor symmetry and its breakdown at hadron colliders is just as important as it is for electroweak symmetry breaking. Given how little is known of this physics, it is essential that detectors be designed to allow for the broadest possible investigations. This can be done only by testing designs against a wide variety of scenarios for flavor physics.

Top-quark physics, in particular, will be an important part of a supercollider's physics program for many reasons. Even if the top quark has been found at the Tevatron Collider,<sup>7</sup> precise measurements of its mass and other properties may not be possible there because of limitations in the detectors and the machine itself. The top quark's apparently very large mass of 175 GeV is our most dramatic example of flavor symmetry breaking. Thus, if other manifestations of flavor physics are accessible at supercollider energies, the top quark will be an important key to finding them. If charged scalar bosons,  $H^\pm$ , exist, then either  $t \rightarrow H^+b$  or  $H^+ \rightarrow t\bar{b}$  is expected to be an important decay mode. Also, many technicolor models contain a color-octet, spin-zero "technieta" boson,  $\eta_T$ , with mass in the range 300–500 GeV. The  $\eta_T$  would be produced via gluon fusion and is expected to decay

into  $\bar{t}t$  pairs.<sup>11,64,65</sup> Its cross section at the LHC may be enormous. At the same time,  $t$ -quark production processes can be serious backgrounds to new physics. An example of this was encountered in Section 5.2, where it was seen that isolated-photon backgrounds arising in  $\bar{t}t$  production were an important background to the  $\bar{t}tH^0 \rightarrow \ell^\pm\gamma\gamma$  signal for production of an intermediate mass Higgs boson. Thus, it is essential to know as much as possible about the rate and other characteristics of  $t$ -quark production. Finally, the fact that  $t$ -production gives a pure sample of  $W$ -bosons, with  $M_W$  and  $m_t$  accurately known, may be useful for calibrating the calorimeters for jet energy measurements.

The work reported in this section was done over a year before the announcement by the CDF Collaboration of its evidence for the top-quark. The top-quark masses considered in this section are 140 GeV (as generally used in this report) and approximately 250 GeV. These bracket fairly well the 175 GeV value reported by CDF. Therefore, we have not felt it necessary to repeat the analyses for the CDF central value. This section discusses the following examples of top physics in the context of the GEM detector:

1. Discovery and measurement of the mass of heavy top quarks ( $m_t \simeq 250$  GeV) pair-produced by  $gg, \bar{q}q \rightarrow \bar{t}t$  and decaying via the standard mode  $t \rightarrow W^+b$ . In this case, one  $t$ -quark gives an isolated electron or muon from  $W$ -decay plus a non-isolated muon from the decay  $b \rightarrow c\mu\bar{\nu}_\mu$ , and the top mass is determined from the invariant mass distribution,  $M_{\ell\mu}$ , of the isolated lepton and the non-isolated muon.<sup>48,66</sup> This study may be viewed as a model of using multi-lepton modes to search for a very heavy quark decaying into a light one plus a  $W$ -boson.
2. Discovery and mass measurement of top quarks in  $\bar{t}t$  production, both with  $m_t = 140$  GeV and with  $m_t = 250$  GeV. Again, the standard  $t \rightarrow W^+b$  decay mode is assumed. Events are tagged by one isolated high- $p_T$  lepton ( $e$  or  $\mu$ ) from decay of one of the  $W$ -bosons and several high- $p_T$  jets. The other  $W$ -boson and its parent  $t$ -quark are observed in their hadronic decay modes.<sup>67</sup>
3. Discovery and study of a charged scalar  $H^+$  produced in the decay of a heavy top quark,  $t \rightarrow H^+b$ . The scalar will be assumed to decay as  $H^+ \rightarrow \tau^+\nu_\tau \rightarrow$  one or three prongs.<sup>68</sup> For this search, one  $t$ -quark is tagged using the standard mode  $t \rightarrow W^+b \rightarrow$  isolated lepton.

### 5.3.1. Heavy Top-Quark Detection and Mass Measurement via the $M_{\ell\mu}$ Distribution

This analysis<sup>66</sup> uses  $\bar{t}t$  events with two leptonic top decays and an additional non-isolated muon from  $b \rightarrow \mu X$ . The top mass is determined from the mass  $M_{\ell\mu}$  of the non-isolated muon and the isolated lepton of the opposite sign. While the  $M_{\ell\mu}$  distribution is broad, this analysis avoids hadronic energy measurements and minimizes the sensitivity to the top production dynamics.

ISAJET 6.36 with the EHLQ-1 distribution functions was used to generate 60K  $\bar{t}t$  events for each of the masses  $m_t = 200, 230, 250, 270$  and 300 GeV. (The  $t$ -quarks

were generated with  $50 \text{ GeV} < p_T < 1000 \text{ GeV}$ , and the appropriate decays were forced.) The signal events are those with one isolated electron and one isolated muon of opposite sign, together with one non-isolated muon of either sign. Choosing isolated leptons of different flavors eliminates backgrounds from  $Z^0 \rightarrow e^+e^-, \mu^+\mu^-$ . The signal cross sections (assuming  $B(W \rightarrow \ell\nu) = B(b \rightarrow \mu^- + X) = 1/9$ ) for  $m_t = 200, 250$  and  $300 \text{ GeV}$  were found to be  $19.9 \text{ pb}, 8.2 \text{ pb}$  and  $4.0 \text{ pb}$ , respectively.

The signal cross sections are much larger than all backgrounds, as discussed below. To optimize the separation between isolated leptons from  $W$ -decay and non-isolated ones from  $b$ -decay, the following cuts were imposed to select isolated electrons:

$$\begin{aligned}
|\eta_e| &< 2.4 \\
\sum_{R=0.2} E_T(\text{EC}) &> 40 \text{ GeV} \\
\sum_{R=0.4} E_T - \sum_{R=0.2} E_T(\text{EC}) &< 10 \text{ GeV} \\
0.8 < E_T(R = 0.2)/p_T(\text{CT}) &< 1.2,
\end{aligned} \tag{5.5}$$

where  $E_T$  is the transverse energy in a cell of the full calorimeter;  $E_T(\text{EC})$  is the transverse energy in EM calorimeter cells;  $p_T(\text{CT})$  is the electron momentum as measured in the tracker. As usual, the sums are over  $\eta - \phi$  cones of radius  $R$ . The cuts for isolated muons were:

$$\begin{aligned}
|\eta_\mu| &< 2.4 \\
p_T &> 40 \text{ GeV} \\
\sum_{R=0.4} E_T - \sum_{R=0.1} E_T &< 2 \text{ GeV}.
\end{aligned} \tag{5.6}$$

Non-isolated muons were required to satisfy:

$$\begin{aligned}
|\eta_\mu| &< 2.4 \\
p_T &> 20 \text{ GeV} \\
\sum_{R=0.4} E_T - \sum_{R=0.1} E_T &> 10 \text{ GeV}.
\end{aligned} \tag{5.7}$$

The choice  $R = 0.2$  for the cone defining the electron energy is not critical because the electron energy measurement does not need to be very precise here. The  $M_{e\mu}$  and  $M_{\mu\mu}$  distributions turn out to be very similar for this choice of isolation parameters and not very sensitive to moderate changes. For the relatively low- $p_T$  muons in the top-quark decays, the muon energy may be corrected simply by adding the average energy loss in the calorimeter for a given momentum and rapidity. For a top mass of  $250 \text{ GeV}$ , the isolation cut (5.6) retained 78% of the muons from  $W$ -decay while rejecting 99% of the muons from  $b$ -decay. The non-isolation cut in (5.7) accepted 89% of  $b \rightarrow \mu + X$  and rejected 91% of  $W \rightarrow \mu\nu_\mu$ .

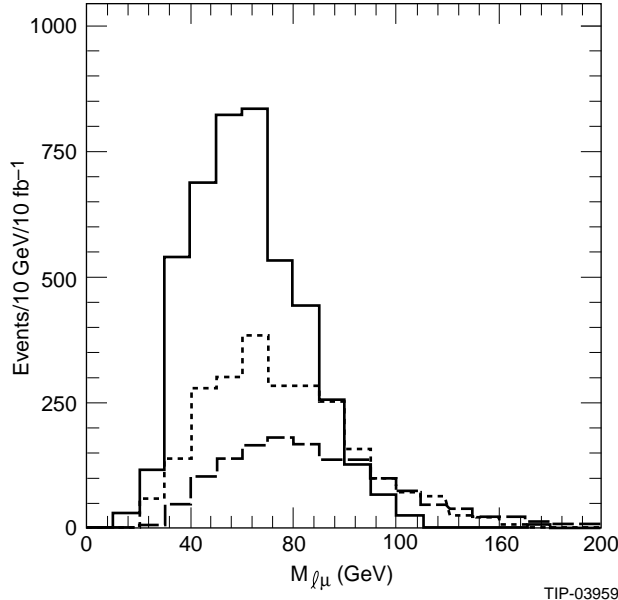


FIG. 35.  $M_{\ell\mu}$  distribution for an isolated lepton and a nonisolated muon of opposite sign for  $m_t = 200$  (solid), 250 (dotted), and 300 GeV (dashed).

There was a 30% contamination of the  $t\bar{t} \rightarrow e_{\text{isol}}^{\pm} \mu_{\text{isol}}^{\mp} + \mu_{\text{non-isol}}$  signal due to non-isolated muons in the decay of  $c$ -quarks which, in turn, came from the decay of the “wrong”  $t$ -quark or from  $g \rightarrow c\bar{c}$ . This background was reduced to the 15% level by selecting events in which the isolated lepton and non-isolated muon of opposite sign are close to each other and, hence, more likely to be from the decay of the same  $t$ -quark. Events were required to satisfy

$$\delta\phi(\ell\mu) < 90^\circ.$$

The acceptance of this cut was found to be 67%, 56% and 49% for  $m_t = 200$ , 250 and 300 GeV. A detailed simulation showed that the reconstruction efficiency was greater than 95% even for non-isolated muons from  $t \rightarrow b \rightarrow \mu$  decays. The overall acceptance ranged from 1.1% for  $m_t = 200$  GeV to 1.8% for  $m_t = 300$  GeV both for the  $t, \bar{t} \rightarrow e_{\text{isol}}^{\pm} \mu_{\text{non-isol}}^{\mp}$  events and for the  $\mu_{\text{isol}}^{\pm} \mu_{\text{non-isol}}^{\mp}$  events. These efficiencies are low because the analysis was designed to obtain a very clean sample. The total number of  $\ell_{\text{isol}}^{\pm} \mu_{\text{non-isol}}^{\mp}$  events expected with an integrated luminosity of  $10 \text{ fb}^{-1}$  is 4500, 2400 and 1400 for  $m_t = 200$ , 250 and 300 GeV.

Backgrounds to the  $t\bar{t} \rightarrow e_{\text{isol}}^{\pm} \mu_{\text{isol}}^{\mp} \mu_{\text{non-isol}}$  signal from production of  $W^{\pm} + \text{jets}$  and  $Z^0 + \text{jets}$  were considered. The most important contributions come from  $b$ -quark jets and  $Z^0 \rightarrow \tau^+\tau^- \rightarrow e^{\pm} + \mu^{\mp} + \cancel{E}_T$ . After the selections described above, the  $W^{\pm} + \text{jets}$  background was found to be less than 9% of the signal for the 250 GeV top quark; the  $Z^0 + \text{jets}$  background was negligible.<sup>66</sup>

The shapes of the  $M_{e\mu}$  and  $M_{\mu\mu}$  distributions are nearly identical. Thus, adding them together to form a  $M_{\ell\mu}$  distribution adds statistical weight to the  $m_t$  determination without

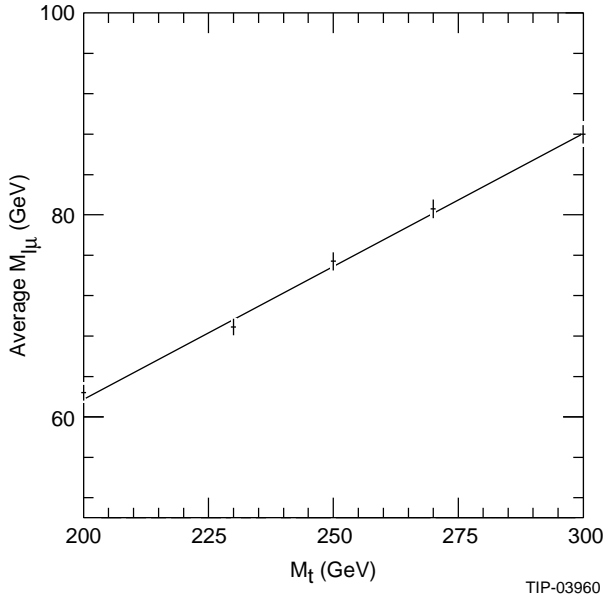


FIG. 36: Mean value of  $M_{\ell\mu}$  vs.  $m_t$ .

introducing significant systematic error. The  $M_{\ell\mu}$  distributions are plotted in Fig. 35 for several values of  $m_t$ . The mean value of  $M_{\ell\mu}$  should vary linearly with  $m_t$  and does, as can be seen from Fig. 36 (also see Ref. 69). A statistical error of 2.3 GeV on the mass of a 250 GeV top quark is expected for  $10 \text{ fb}^{-1}$  of data.

The systematic error in this method of determining  $m_t$  arises from imperfect knowledge of the  $b$ -quark fragmentation function and of the  $p_T$  distribution of the  $t$ -quarks. These affect the momentum distributions of the non-isolated muon and the isolated lepton, respectively. The effect of heavy-quark fragmentation was studied by varying the parameter  $\epsilon$  in the Peterson fragmentation function from its nominal value of  $\epsilon = 0.006$ .<sup>9</sup> The range considered,  $1\sigma = 0.002$ , led to a variation of 2.3 GeV in the mass of a 250 GeV  $t$ -quark. A measure of the systematic error due to the  $p_T(t)$ -distribution was obtained by varying the amount of initial state radiation in  $\bar{t}t$  production. This resulted in a 3.4 GeV change in the mass determined for the 250 GeV  $t$ -quark. Finally, next-to-leading-order QCD corrections to the  $\bar{t}t$  cross section increase the magnitude of the cross section by about 60%, but do not significantly change the shape.<sup>70</sup> Still higher-order corrections are expected to amount to  $\pm 15\%$ . We conclude that, with an integrated luminosity of  $10 \text{ fb}^{-1}$ , it would be possible to use the  $M_{\ell\mu}$  method to determine the mass of a 250 GeV top quark to within an error of  $\pm 2.3 \text{ GeV}$  (statistical) and  $\pm 4.1 \text{ GeV}$  (systematic).

### 5.3.2. Top-Quark Detection and Mass Measurement via the $M_{\text{jij}}$ Distribution

The most direct measurement of the top-quark mass comes from the nonleptonic decay  $t \rightarrow Wb \rightarrow \bar{q}q'b$ , giving three jets. This is also the most precise measurement if systematic uncertainties associated with jet definition and energy measurement are under control.

Furthermore, it is important for flavor physics spectroscopy to observe the top quark in nonleptonic decay modes.

ISAJET was used to generate 300K  $\bar{t}t$  events for  $m_t = 140$  and for 250 GeV.<sup>67</sup> As above, the top quarks were generated with  $50 \text{ GeV} < p_T < 1000 \text{ GeV}$ . Events were selected in which one  $W$  decayed to an electron or muon while the other  $W$  decayed nonleptonically. The physics background to  $\bar{t}t \rightarrow \ell_{\text{isol}}^\pm + \text{jets}$  comes mainly from production of  $W + \text{jets}$ . Since both the signal cross section and the signal/background ratio are much higher than at the Tevatron,<sup>7</sup> it is possible to make cuts that render this background unimportant. Thus, a non-isolated muon tag was not required. The ISAJET cross sections for these events, including  $W$ -boson branching ratios, are 4.1 nb and 0.44 nb for the two values of  $m_t$ . The isolated leptons were required to satisfy the cuts in Eqs.(5.5) and (5.6).

To eliminate combinatorial backgrounds in the multijet mass distributions, the  $t$ -quark and individual jets were forced to be at high  $p_T$  and to be in the hemisphere opposite the isolated lepton. For such events, the three jets from the decays of the  $t$  tend to be close, and a cone of small radius  $R = 0.4$  was therefore used. Individual jets were required to have  $p_T > 30 \text{ GeV}$  (50 GeV) for  $m_t = 140 \text{ GeV}$  (250 GeV). In both cases, jets were required to satisfy  $\delta\phi(\ell \text{ jet}) > 90^\circ$ . Finally, the three highest- $p_T$  jets satisfying these constraints were required to have  $|\vec{p}_T(3 \text{ jets})| > 200 \text{ GeV}$  (300 GeV) for  $m_t = 140 \text{ GeV}$  (250 GeV). The combined geometrical acceptance and efficiency of these cuts was found to be 0.70% and 1.0% for  $m_t = 140$  and 250 GeV. The number of events obtained per  $10 \text{ fb}^{-1}$ , taking into account trigger and reconstruction efficiencies and these acceptances, were 240K and 40K respectively. The  $W + \text{jets}$  background was found to be negligibly small for the 140 GeV case. It contributed 15% to the three-jet mass spectrum for 250 GeV, but this had no important effect on the determination of  $m_t$ .

Consider first the case of  $m_t = 140 \text{ GeV}$ . The  $W \rightarrow 2 \text{ jets}$  and  $t \rightarrow Wb \rightarrow 3 \text{ jets}$  mass distributions,  $M_{jj}$  and  $M_{jjj}$ , are shown in Figs. 37 and 38. Here, the trijet search region was  $110 \text{ GeV} < M_{jjj} < 170 \text{ GeV}$ , and at least one dijet pair was required to satisfy  $|M_{jj} - M_W| < 20 \text{ GeV}$ . All dijet pairs passing the cuts appear in Fig. 37 (a). The fitted  $W$ -mass peak is at 75.8 GeV in this figure, and the resolution is 13.9 GeV. The large combinatorial background is a consequence of the kinematics: for  $m_t = 140 \text{ GeV}$  and  $M_W = 80 \text{ GeV}$ , the three jets tend to be roughly equidistant in  $\eta - \phi$  space. The background comes from picking up the  $b$ -jet from the same or, less frequently, the other  $t$ -quark decay. The signal-to-noise ratio in the  $W$ -peak region is about 2:1.

This signal-to-noise can be improved considerably by requiring that one of the jets passing the above cuts be tagged as a  $b$  jet by the tracker. Figure 37 (b) shows the  $M_{jj}$  distribution for events with an identified  $b$  jet which is then excluded from the dijet mass. The  $b$ -tag efficiency for this plot was assumed to be 20%. The  $W$  signal-to-noise ratio is improved to 3.9:1. The fitted  $W$  mass in this plot is at 76.9 GeV with a resolution of 8.4 GeV. We emphasize that this  $b$  tag is not required for determining  $m_t$ . This is seen in

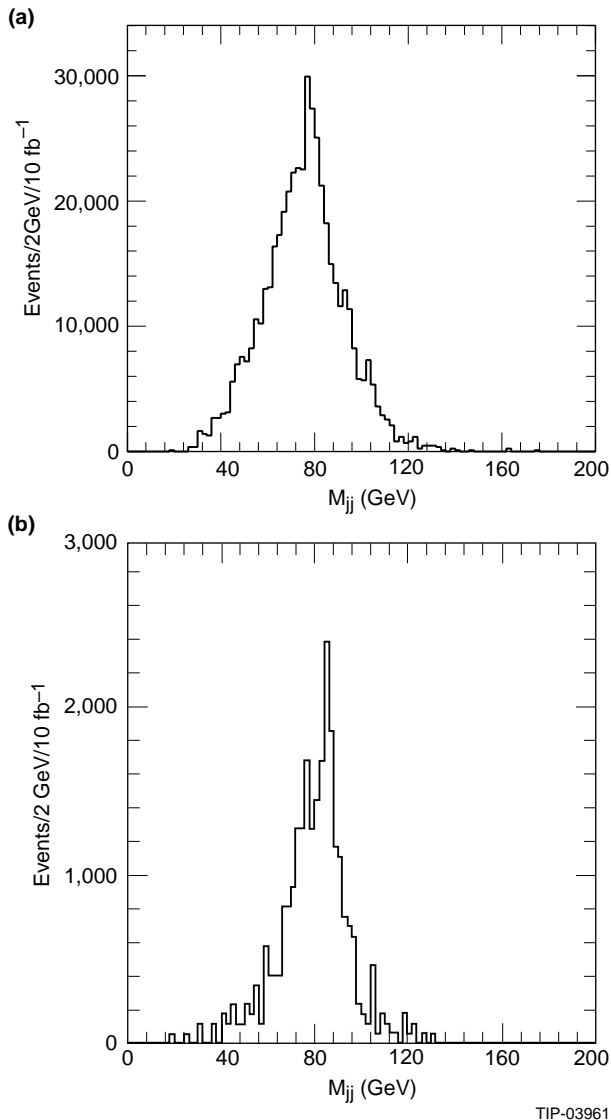


FIG. 37. Dijet mass distribution in  $t\bar{t}$  events with  $m_t = 140$  GeV. (a) No  $b$ -tagging was assumed. (b)  $b$ -tagging was assumed with 20% efficiency.

Fig. 38, where the top-quark peak appears clearly above little combinatorial background. The mass was determined to be 138.2 GeV with a resolution of 8.1 GeV.

For  $m_t = 250$  GeV, the dijet and trijet mass distributions are shown in Figs. 39 and 40. The search region was  $200 \text{ GeV} < M_{jjj} < 300 \text{ GeV}$ . As above, at least one dijet was required to have invariant mass within 20 GeV of  $M_W$  and the invariant mass of the two closest jets was plotted. There was no need for a  $b$ -tag to sharpen the dijet mass distribution, since for such a heavy top-quark the two jets from the  $W$  are closer to each other than either is to the  $b$  jet. Thus, the combinatorial background under the  $W$ -peak is much smaller if one selects the closest two jets. The fitted  $W$  mass was found to be 79.8 GeV, with a resolution of 7.1 GeV. The top-quark mass was determined to be

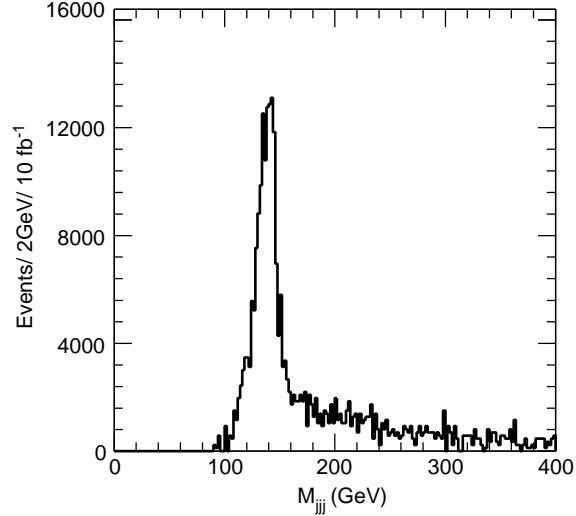


FIG. 38: Trijet mass distribution in  $t\bar{t}$  events with  $m_t = 140$  GeV, without  $b$ -tagging.

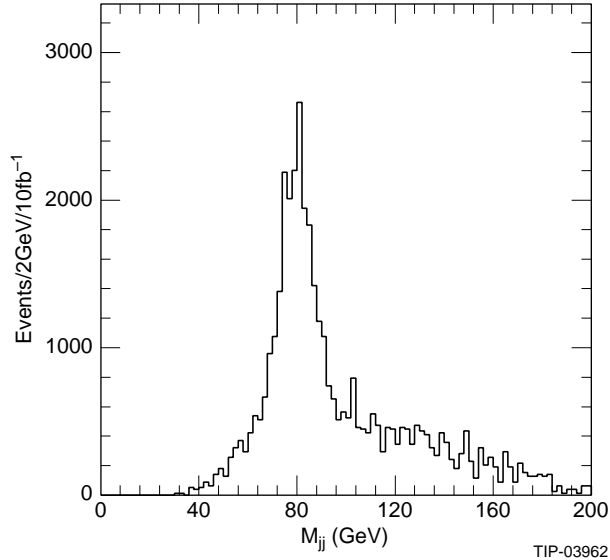


FIG. 39: Dijet mass distribution in  $t\bar{t}$  events with  $m_t = 250$  GeV.

247.4 GeV with a resolution of 14.7 GeV.

The statistical uncertainty on the top-quark mass for  $10 \text{ fb}^{-1}$  of data is approximately 0.03 GeV (0.11 GeV) for  $m_t = 140$  GeV (250 GeV). Systematics dominate the error in this  $m_t$  measurement. The largest effect is the uncertainty in the jet energy measurement. More detailed studies of the calorimeter — beam tests as well as simulations — will be required to yield adequate correction functions. It will be helpful that the  $t \rightarrow Wb$  process is self-calibrating: The position and width of the  $W$  peak will help calibrate the energies of jets in  $t$ -decay and determine the systematic uncertainty in  $m_t$ .

The top quark will be a signal of flavor physics. One example is the  $\eta_T$ , a spin-zero

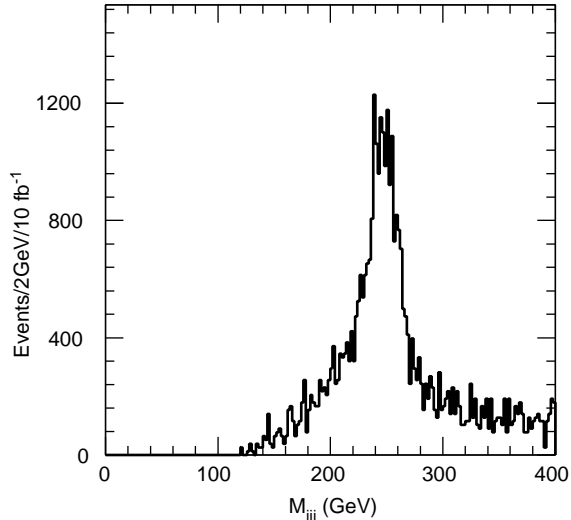


FIG. 40: Trijet mass distribution in  $t\bar{t}$  events with  $m_t = 250$  GeV.

color-octet boson occurring in many technicolor models.<sup>11,64</sup> In modern models,<sup>19</sup> the  $\eta_T$  is expected to have a mass in the range 300 – 500 GeV.<sup>71,65</sup> It is produced in  $pp$  collisions via gluon fusion with a cross section of order 1–50 nb, depending on its mass, the number of technicolors, and other model-dependent factors. It is expected to decay predominantly to  $t\bar{t}$  with a width of order 10–100 GeV, again model-dependent.

In a search for the  $\eta_T$ , one would tag  $t\bar{t}$  production in the  $\ell_{\text{isol}}^\pm + \text{jets}$  mode and look for an enhancement in the  $t\bar{t}$  invariant mass distribution. This invariant mass can be determined up to a quadratic ambiguity by assuming that the missing- $E_T$  is due to  $W^\pm \rightarrow \ell^\pm \nu_\ell$ . The resolution on this invariant mass for  $M_{t\bar{t}} \simeq 400$  GeV is about 15 GeV *plus* the contribution from the  $\cancel{E}_T$  resolution. For a 20 GeV wide  $\eta_T$ , and assuming that the  $M_{t\bar{t}}$  resolution is 30 GeV, the  $\eta_T$  appears as an enhancement 75 GeV wide. The underlying  $t\bar{t}$  cross section in such a region is about 3 nb for  $m_t = 140$  GeV and  $M_{\eta_T} = 300\text{--}500$  GeV. There should be no difficulty discovering the  $\eta_T$  over such a background.

### 5.3.3. Discovery of a Charged Scalar in the Decay of a Heavy Top Quark

Charged color-singlet scalar bosons,  $H^\pm$ , occur in multi-Higgs-doublet models, in all supersymmetric extensions of the Standard Model and, typically, as technipions in models of dynamical electroweak symmetry breaking. Generally, their couplings are Higgs-like. That is,  $H^\pm$  tend to decay to the heaviest fermion pairs kinematically accessible and they often must be in the same generation. Since  $H^\pm$  are color-singlets, they are copiously produced only if there is a heavier quark which can decay into them.

We study discovery of an  $H^\pm$  in the decay products of a heavy top quark. The masses  $m_t = 250$  GeV and  $M_{H^+} = 150$  GeV were used for the discussion that follows. At the end, results for other mass combinations will be described. It was assumed that both  $t \rightarrow W^+b$  and  $t \rightarrow H^+b$  decays are allowed. The charged scalar was assumed to decay into  $c\bar{s}$  and

$\tau^+\nu_\tau$ . Only the decay mode  $H^+ \rightarrow \tau^+\nu_\tau$  is considered here,<sup>68</sup> since for  $H^+ \rightarrow c\bar{s}$ , it should be straightforward to discover the  $H^+$  and measure its mass using the same technique as described for the study of  $t \rightarrow W^+b \rightarrow 3\text{jets}$  in the previous section.

The various branching ratios for  $t$  and  $H^+$  decay are model-dependent. In the absence of experimental support for any particular model, it is appropriate to assume only that  $B(t \rightarrow W^+b) + B(t \rightarrow H^+b) = 1$  and  $B(H^+ \rightarrow c\bar{s}) + B(H^+ \rightarrow \tau^+\nu_\tau) = 1$ , and to study the reach of the detector for  $H^\pm$  as a function of the branching ratios. For comparison with other simulations,<sup>72,73</sup> we also present results in terms of the two-Higgs-doublet model occurring in the minimal supersymmetric standard model (MSSM).<sup>52</sup>

The presence of  $t \rightarrow H^+b$ , followed by  $H^+ \rightarrow \tau^+\nu_\tau$ , is signalled by a breakdown of lepton universality expected if only  $t \rightarrow W^+b$  were allowed (also see Refs. 72 and 73). In addition to the  $\pi^+\nu_\tau$  decay mode used as a  $\tau$ -tag in those references, all hadronic  $\tau$ -decay modes were used here.

ISAJET 6.50 was used to generate 15K each of  $t\bar{t} \rightarrow W^+W^-b\bar{b}$  and  $t\bar{t} \rightarrow WH^\pm b\bar{b}$  events. The ISAJET decay table was updated to include all major  $\tau$  decay modes. Hadronic modes account for 64.5% of all decays while the  $\pi^+$  mode is only 12%. Signal events were selected by requiring an isolated electron or muon and a tau candidate. The criteria for an isolated  $\mu^\pm$  were taken to be:

$$\begin{aligned} |\eta_\mu| &< 2.4 \\ p_T &> 20 \text{ GeV} \\ \sum_{R=0.4} E_T - \sum_{R=0.1} E_T &< 2 \text{ GeV} \end{aligned} \tag{5.8}$$

Muons were required to be fully reconstructed according to the efficiency parameterized in `gemfast`. For an isolated  $e^\pm$  the criteria used were

$$\begin{aligned} |\eta_e| &< 2.4 \\ \sum_{R=0.3} E_T &> 50 \text{ GeV} \\ \sum_{R=0.2} E_T(\text{EC}) &> 40 \text{ GeV} \\ \sum_{R=0.4} E_T - \sum_{R=0.2} E_T(\text{EC}) &< 10 \text{ GeV} \\ 0.8 &< E_T(R=0.2)/p_T(\text{CT}) < 2.0. \end{aligned} \tag{5.9}$$

For analysis of the  $\tau$ -lepton's two-body decays, it is important to account properly for the polarization it has in  $W^\pm$  and  $H^\pm$  decays. The decay  $W^\pm \rightarrow \tau^\pm\nu_\tau$  conserves chirality (the same as helicity for a high-energy  $\tau$ ), while  $H^\pm \rightarrow \tau^\pm\nu_\tau$  maximally violates it. Then, for example, the  $\pi^+$  occurring in  $\tau^+ \rightarrow \pi^+\bar{\nu}_\tau$  tends to follow the  $H^+$  direction

of motion and so has higher  $p_T$  than  $\pi^+$  from  $W^+ \rightarrow \tau^+ \nu_\tau$  decays. This effect is enhanced here because  $M_{H^+}$  is larger than  $M_W$ . The polarization correlations were implemented in ISAJET for two-body  $\tau$  decays. The  $\tau$ -polarization effects are small for the three-prong decays and require no special simulation.<sup>74</sup>

Isolated  $\tau$  candidates were selected by requiring:

$$\begin{aligned}
|\eta_\tau| &< 2.4 \\
N_{\text{ch}} &= 1 \text{ or } 3 \\
\sum_{R=0.3} E_T &> 50 \text{ GeV} \\
\delta\phi(\ell \tau) &> 100^\circ \\
\sum_{R=0.4} E_T - \sum_{R=0.2} E_T &< 10 \text{ GeV}
\end{aligned} \tag{5.10}$$

For the charge multiplicity ( $N_{\text{ch}}$ ) cut, tracks were required to have  $p_T > 1 \text{ GeV}$  and to lie within a cone of  $R = 0.1$  around the calorimeter jet axis. The leading track in this cone was required to have  $p_T > 15 \text{ GeV}$ . Electrons from  $\tau$  decays were not included in the  $\tau$  sample if they passed the isolated  $e$  criteria in Eq.(5.9). Muons from  $\tau$ -decays are predominantly isolated and are thus rejected by the absence of significant activity in the calorimeter. The central tracker was not used to tag  $\tau$  leptons by their displaced vertices. If it were, it would further enhance the significance of the nonuniversality signal.

In addition, we required a  $b$  jet tagged by the central tracker. The  $b$ -jet criteria were  $|\eta_b| < 2.4$ ,  $\delta\phi(\ell b) < 100^\circ$ , and scalar  $E_T > 30 \text{ GeV}$ . A tagging efficiency  $\epsilon(b\text{-tag}) = 20\%$  was assumed in this study. Alternatively,  $b$  jets could be tagged by a non-isolated muon, but this would decrease the signal significances somewhat.<sup>68</sup>

The number of standard deviations  $N_\sigma$  by which the number of  $\tau$  events exceeds the expectation from lepton universality is

$$N_\sigma = \frac{N(WH^\pm \rightarrow \ell_{\text{isol}}\tau)}{\sqrt{N(WW \rightarrow \ell_{\text{isol}}\tau) + N(WH^\pm \rightarrow \ell_{\text{isol}}\tau)}}. \tag{5.11}$$

Here, the event numbers are given by

$$\begin{aligned}
N(WW \rightarrow \ell_{\text{isol}}\tau) &= 2N_{\bar{t}t} B^2(t \rightarrow W^+b) \\
&\times B(W \rightarrow \ell\nu_\ell) B(W \rightarrow \tau\nu_\tau) B(\tau \rightarrow \text{hadrons}) \\
&\times \epsilon(W \rightarrow \ell) \epsilon(W \rightarrow \tau) \epsilon(b\text{-tag}) \epsilon(t\text{-tag}) \epsilon(t\text{-trigger});
\end{aligned} \tag{5.12}$$

$$\begin{aligned}
N(WH^\pm \rightarrow \ell_{\text{isol}}\tau) &= 2N_{\bar{t}t} B(t \rightarrow W^+b) B(t \rightarrow H^+b) \\
&\times B(W \rightarrow \ell\nu_\ell) B(H^+ \rightarrow \tau\nu_\tau) B(\tau \rightarrow \text{hadrons}) \\
&\times \epsilon(W \rightarrow \ell) \epsilon(H^+ \rightarrow \tau) \epsilon(b\text{-tag}) \epsilon(t\text{-tag}) \epsilon(t\text{-trigger}).
\end{aligned}$$

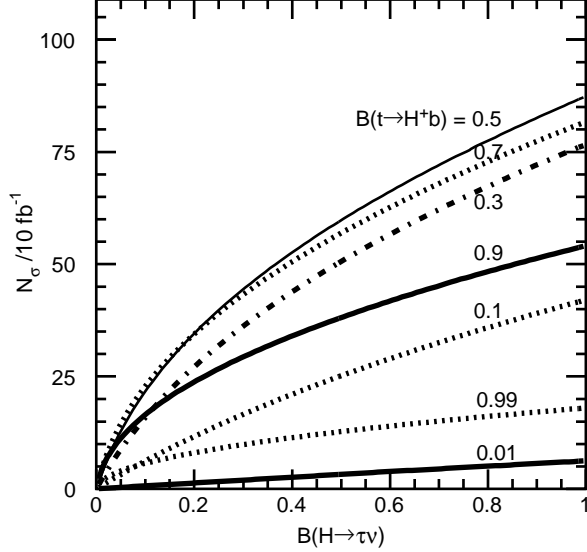


FIG. 41. Significance of the  $t \rightarrow H^+ b$ ,  $H^+ \rightarrow \tau^+ \nu_\tau$  signal vs.  $B(H^+ \rightarrow \tau^+ \nu_\tau)$  for various  $B(t \rightarrow H^+ b)$ . Here,  $m_t = 250$  GeV and  $M_{H^+} = 150$  GeV.

For a 250 GeV top quark, the number of events produced with an integrated luminosity of  $10 \text{ fb}^{-1}$  is  $N_{tt} = 1.5 \times 10^7$ . The efficiencies  $\epsilon(W \rightarrow \tau)$  and  $\epsilon(H^+ \rightarrow \tau)$  are the ratios of the numbers of true  $\tau$ -leptons passing the above cuts to the number generated, including  $\tau \rightarrow e$  events misidentified as hadronic  $\tau$ -decays. For  $m_t = 250$  GeV and  $M_{H^+} = 150$  GeV, these efficiencies were found to be  $\epsilon(W \rightarrow \tau) = 9.8\%$  and  $\epsilon(H^+ \rightarrow \tau) = 14.7\%$ . The efficiency for finding  $W \rightarrow \ell \nu_\ell$  events was 36% for electrons and 45% for muons. The average value  $\epsilon(W \rightarrow \ell) = 40\%$  was used. The top-tagging efficiency,  $\epsilon(t\text{-tag}) = 69\%$ , is the fraction of top events remaining after the tau-selections. The efficiency for triggering on top quarks at Level 1 was found to be 93%.<sup>68</sup>

The backgrounds to the  $\bar{t}t \rightarrow W^\mp H^\pm \rightarrow \ell^\mp + \tau^\pm + X$  signal come from (1)  $t\bar{t} \rightarrow WWb\bar{b}$  and  $WH^\pm b\bar{b}$  events in which  $W^\pm$  and  $H^\pm$  decay to jets which fake a  $\tau$ ; (2)  $W + \bar{Q}Q$  events with  $Q = c, b$ ; and (3)  $\bar{b}b$  production. To study the first background, 40K two-jet events were generated with  $p_T$  in the range 50 – 1000 GeV. All jets found by **gemfast** with  $E_T > 25$  GeV were subjected to the  $\tau$ -selection criteria above. A rejection factor of  $\mathcal{R}(\tau/\text{jet}) = 0.0027$  was found. Since there are two to three jets in the hemisphere opposite the isolated lepton, this background amounts to 8.4% of the  $\bar{t}t \rightarrow WW \rightarrow \ell_{\text{isol}} + \tau$  signal and  $1.4\% \times (1 - B(H^+ \rightarrow \tau^+ \nu_\tau))/B(H^+ \rightarrow \tau^+ \nu_\tau)$  of the  $\bar{t}t \rightarrow WH \rightarrow \ell_{\text{isol}} + \tau$  signal. Including these backgrounds reduces  $N_\sigma$  by 3%. The other backgrounds have been shown to reduce  $N_\sigma$  by less than 3%.<sup>72,73,68</sup>

The significance for  $10 \text{ fb}^{-1}$  is plotted against  $B(H^+ \rightarrow \tau^+ \nu_\tau)$  in Fig. 41 for  $B(t \rightarrow H^+ b) = 0.01 - 0.99$ . Backgrounds are not included in these plots because they are so small. A signal ( $N_\sigma > 5$ ) for the  $t \rightarrow H^+ \rightarrow \tau^+$  decay channel can be discovered if  $B(t \rightarrow H^+ b) \gtrsim 0.02$  and  $B(H^+ \rightarrow \tau^+ \nu_\tau) \gtrsim 0.05$ .

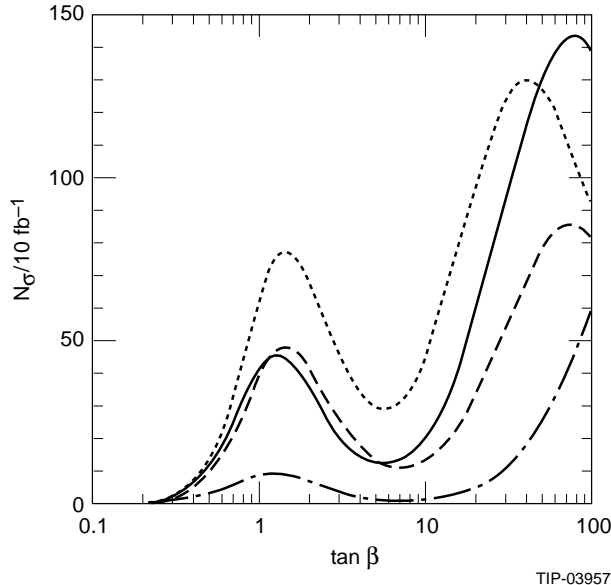


FIG. 42. Significance of the  $t \rightarrow H^+b$ ,  $H^+ \rightarrow \tau^+\nu_\tau$  signal vs.  $\tan\beta$  for various  $m_t = 250$  GeV and  $M_{H^+} = 225$  GeV (dash-dotted); 250 and 150 GeV (dotted); 150 and 125 GeV (solid); 150 and 100 GeV (dashed).

We have also computed  $N_\sigma$  for the two-Higgs-doublet model used in the MSSM. In this model,  $B(t \rightarrow H^+b)$  and  $B(H^+ \rightarrow \tau^+\nu_\tau)$  are determined by a single parameter,  $\tan\beta$ , the ratio of the vacuum expectation values of the two Higgs doublets. The significances were determined for four cases:  $(m_t, M_{H^+}) = (250, 225)$ ,  $(250, 150)$ ,  $(150, 125)$ , and  $(150, 100)$  to facilitate comparison with Ref. 72. The significances expected in GEM are shown in Fig. 42. For all but the heaviest mass combination, GEM is able to detect a  $5\sigma$  enhancement in  $\tau$  production for  $\tan\beta > 0.4$ . For  $(m_t, M_{H^+}) = (250, 225)$ , the discovery level covers the range  $0.7 < \tan\beta < 2.0$  and  $\tan\beta > 20$ . By tagging the  $\tau$  lepton in all its hadronic modes instead of just  $\tau \rightarrow \pi\nu_\tau$ , the significances have been increased by a factor of 2.3–5.

#### 5.4. Jet Physics at Large Transverse Momentum

Although GEM emphasized precision measurement of photons and leptons up to the highest SSC luminosities, the accurate identification and measurement of jets is also important. The search for a high mass Higgs boson (Section 5.2) and heavy flavor physics (Section 5.3) are two examples of new physics requiring accurate understanding and measurement of jets. Hadronic jets can also be important backgrounds to new physics; the search for  $H^0 \rightarrow \gamma\gamma$  is an example of this. The errors in jet measurements introduced by analysis effects, such as jet definition and clustering algorithms, and by instrumental effects, such as detector resolution,  $e/h$  for the calorimeters, and cracks and dead spaces, must be carefully studied and kept under control. This section discusses the main issues involved in measuring the high- $p_T$  jet cross section accurately. The search for signs of quark substructure in deviations from QCD of the jet cross section forms the context for

this discussion.

If quarks and leptons are composite, with structure at the scale  $\Lambda$ , the most visible manifestation at subprocess energies  $\sqrt{\hat{s}} \ll \Lambda$  is the presence of four-fermion contact interactions,  $\mathcal{L}_\Lambda$ , involving the composite quarks and leptons.<sup>76</sup> These interactions induce terms in the cross section for dijet and dilepton production that are of order  $\pi\hat{s}/\Lambda^4$ , leading to significant excesses at “low”  $\hat{s}$ . It is known from experiments at  $e^+e^-$  and hadron colliders that  $\Lambda \gtrsim 1 - 2 \text{ TeV}$ , above the scale of electroweak symmetry breaking.<sup>9,77</sup> Thus,  $\mathcal{L}_\Lambda$  must be  $SU(3) \otimes SU(2) \otimes U(1)$  invariant, and the composite quark and lepton fields appearing in it are electroweak, not mass, eigenstates. This raises the possibility that unacceptably large flavor-changing neutral currents will appear in the contact interactions. The most stringent limit on such interactions comes from the allowed magnitude of new effects in the neutral kaon system. If  $|\Delta S| = 2$  contact interactions exist, they must have  $\Lambda \gtrsim 500 \text{ TeV}$ , well above the reach of the SSC. For the discussion of contact interactions accessible at the SSC, therefore, we shall assume that  $\mathcal{L}_\Lambda$  is symmetric under interchanges of the three generations of quarks and leptons.

Quark substructure shows up directly as an excess of jets at high  $p_T$  or  $\sqrt{\hat{s}}$ . In this section the contact interaction

$$\mathcal{L}_{\text{qq}} = -\frac{4\pi}{2\Lambda^2} \bar{Q}_{La} \gamma^\mu Q_{La} \bar{Q}_{Lb} \gamma_\mu Q_{Lb} \quad (5.13)$$

is used as a model to modify QCD jet production. Here,  $Q_{La} = (u_a, d_a)_L$  are left-handed quark fields and  $a, b = 1, 2, 3$  label the generations. This model for the four-quark contact interaction is essentially the one discussed in Ref. 11 except that all quarks are taken to be composite. PYTHIA 5.6 was used to generate the jet events for QCD and the quark substructure signal.<sup>78</sup> Several different choices of parton distribution functions (PDFs) were used and results compared: EHLQ Set 1,<sup>11</sup> the CTEQ Set 1L,<sup>54</sup> and Morfin-Tung Set 2.<sup>79</sup> The signal region lies above  $E_T = 4 \text{ TeV}$  for the jets. The study described here was made for an integrated luminosity of  $10 \text{ fb}^{-1}$ . We shall show that GEM could reach a substructure scale of about  $25 \text{ TeV}$  with this data sample.

The most important issue in searching for quark substructure is to be certain that an observed excess of high- $E_T$  jets is not an artifact of the detector nor of the analysis. The jet cross section must be normalized to the QCD expectation at lower  $E_T$  to reduce uncertainties due to luminosity (approximately 3% at the Fermilab Tevatron<sup>7</sup>). Since the cross section for jets at the lowest transverse energies is not well-known theoretically, the normalization region used is the middle of the jet  $E_T$  spectrum. Finally, a scheme must be developed that corrects for the calorimeter’s lack of compensation.

For this study signal events were generated with total scalar transverse energy,  $\sum E_T \gtrsim 9 \text{ TeV}$  and the normalization sample was generated with  $\sum E_T > 4.8 \text{ TeV}$ . The only kinematic cut imposed on jets is  $|\eta| < 1.1$ . This enhances the roughly isotropic signal relative to the forward-backward peaked QCD background. More than one jet can be

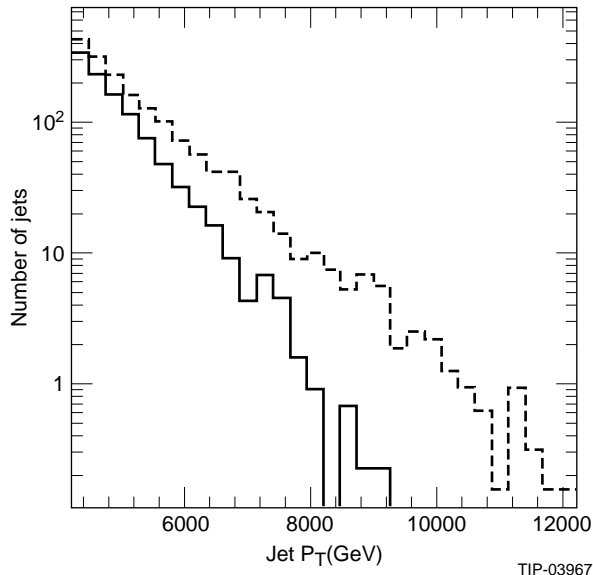


FIG. 43. Inclusive jet  $E_T$  spectrum for substructure at the scale  $\Lambda = 25$  TeV (dashed) and for QCD (solid).

taken from a single event. For these central high- $E_T$  jets, the triggering efficiency is close to 100%. The discovery criterion adopted for this analysis is an excess of 100 events in an  $E_T$ -region in which the observed cross section is twice as large as the QCD expectation.

Jet clustering was done with a fixed-cone algorithm using a large cone,  $R = 0.9$ . The large clustering radius was chosen to reduce energy loss out of the clustering cone. This cone algorithm was found to be efficient and insensitive to detector variations and to have good angular resolution.<sup>75</sup> If the jet-cone radius was decreased to 0.7, the main effect was to shift the energy scale of the jet- $E_T$  spectrum downward by 1.2%. This shift should be calculable in perturbation theory.

A full experimental analysis would have to include the development of a jet energy correction function and an unsmearing procedure for the inclusive jet- $E_T$  spectrum. The correction function must include the effects of the underlying event, showers spreading outside the clustering cone, and detector noise, inefficiencies and nonlinearities. Most of these corrections are reasonably well-understood and tend not to be important for very high- $E_T$  jets. The most important problem is to determine the jet energy scale. Jets whose  $E_T$  is mismeasured upward easily produce a false compositeness signal. The jet energy scale for the calorimeter would be established using test beam and collider data and the energy scale correction would depend on, among other parameters, the jet rapidity and the fraction of electromagnetic energy observed in a jet.

The reach in  $\Lambda$  is limited by incomplete knowledge of the parton distributions and of the jet energy resolution and scale. A number of jet energy reconstruction schemes, particularly weighting algorithms which attempt to boost the hadronic part of a shower, have been used to improve jet energy resolution and linearity.<sup>42,43</sup> We have estimated

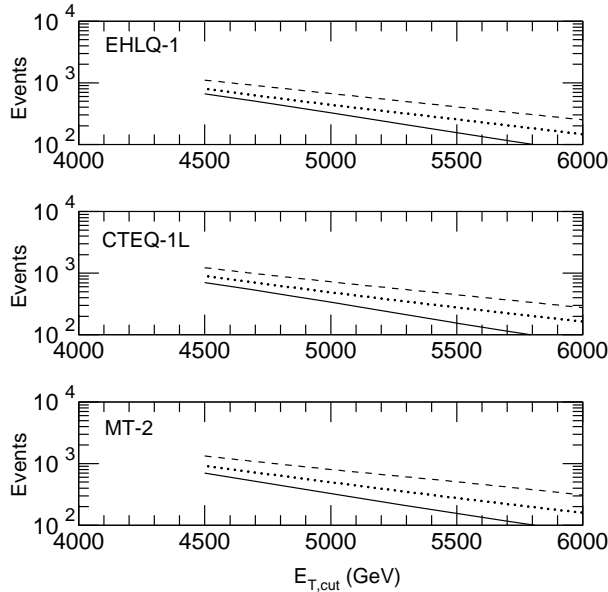


FIG. 44. Number of jets expected with  $10 \text{ fb}^{-1}$  with  $E_T > E_T^{\text{cut}}$ , for various parton distributions. The solid line is QCD (no substructure), dotted line is  $\Lambda = 30 \text{ TeV}$  and dashed line is  $\Lambda = 25 \text{ TeV}$ .

the systematic effects due to nongaussian tails in the energy response and to nonlinearity arising from lack of compensation in the calorimetry. Nongaussian tails were modeled in **gemfast** by adding a second Gaussian of 1% the amplitude and three times the width of the normal Gaussian energy resolution, as described in Section 4.3. To estimate the uncertainty due to parton distributions we compared the rates of the CTEQ-1L, EHLQ-1 and MT-2 distribution functions.

The inclusive cross sections for jets with  $|\eta| < 1.1$ , using the CTEQ-1L distribution functions, are shown in Fig. 43 for  $\Lambda = 25$  and QCD ( $\Lambda = \infty$ ). Fig. 44 shows the number of jets expected in  $10 \text{ fb}^{-1}$  with  $E_T > E_T^{\text{cut}}$ . It is clear that a quark substructure signal at the scale  $\Lambda = 25 \text{ TeV}$  could be discovered easily in this integrated luminosity with a detector whose calorimeter is as linear as the one modeled here. The variation in jet rates obtained using the CTEQ-1L, EHLQ-1 and MT-2 distributions is indicated in Fig. 44. The differences are small compared to the signal and produce a 10 – 20% variation in the observable  $\Lambda$  according to our discovery criterion.

Nonlinearity in the charged pion response was modeled using a GEANT simulation of the GEM detector incorporating the expected  $e/h$  values for each calorimeter. Figure 45 shows the charged pion response, averaged over  $|\eta| < 1.1$ , as a function of energy. The relative response has been set to 1.0 at 200 GeV. The solid curve is the average response obtained using energy-independent weights for each calorimeter layer; the dashed curve shows the response with energy-dependent weighting. The extrapolation to high energies

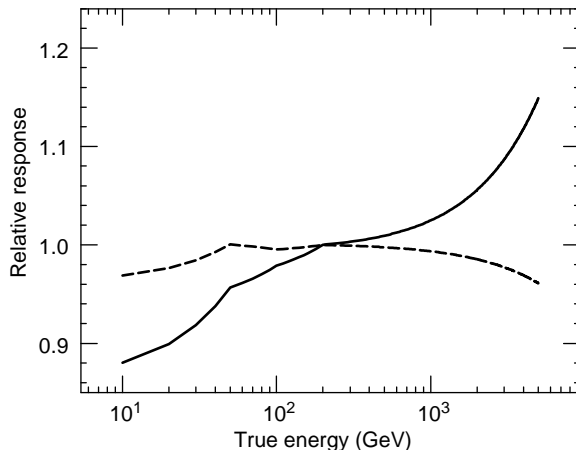


FIG. 45. Calorimeter response to single pions relative to that at 200 GeV, using energy-independent weights (solid curve) and energy-dependent weights (dotted curve).

Table 10. Number of jets expected with  $10 \text{ fb}^{-1}$  using different energy-weighting schemes as described in the text, and the CTEQ-1L parton distributions.

$E_T^{\text{cut}}(\text{GeV})$	4500	5000	5500	6000
Perfect Calorimeter				
$\Lambda = \infty$	704	339	155	74
25 TeV	1226	724	447	276
Energy-independent Weights				
$\Lambda = \infty$	718	349	167	79
25 TeV	1257	739	468	286
Energy-dependent Weights				
$\Lambda = \infty$	676	321	148	70
25 TeV	1189	701	435	267

shown here gives noticeable errors in both cases, but mimics the extrapolation from test beam energies that will have to be carried out when calibrating the real detector.

The effect of the nonlinearity in the two weighting schemes is illustrated in Table 10. The CTEQ-1L distribution functions were used here. As expected from Fig. 45, the energy-independent weighting scheme tends to increase the measured  $E_T$  of the jets, while the energy-dependent scheme reduces jet- $E_T$ . The effects are small, of order 5% and the scale  $\Lambda = 25 \text{ TeV}$  is still easily within reach for a data sample of  $10 \text{ fb}^{-1}$ .

Finally, we can estimate the reach in the quark compositeness scale  $\Lambda$  attainable with a data sample of  $100 \text{ fb}^{-1}$ . We anticipate no special difficulties for high- $E_T$  jet measurement associated with operations at  $\mathcal{L} \simeq 10^{34} \text{ cm}^{-2} \text{ s}^{-1}$ . Thus, the reach in  $\Lambda$  can be determined from the fact that the subprocess cross section goes as  $\hat{s}/\Lambda^4$ . This yields  $\Lambda \simeq 45 \text{ TeV}$ , a

factor of 40 greater than the limit set by existing hadron collider data.

## 5.5. Supersymmetry

Supersymmetry (SUSY) is theoretically attractive because it eliminates the quadratic divergences in the Higgs sector and so allows light elementary Higgs bosons to occur naturally. Its study also provides a good testing ground for many aspects of GEM, including missing energy, jets and leptons. The minimal supersymmetric standard model<sup>52</sup> has two Higgs doublets and superpartners (denoted by a tilde) for all normal particles. In particular there are four neutralinos,  $\tilde{\chi}_i^0$ , which are linear combinations of the partners of the photon,  $Z$ , and neutral Higgs bosons, and two pairs of charginos  $\tilde{\chi}_i^\pm$ . There is a conserved  $R$  parity carried by all superparticles, so they must always be produced in pairs and decay to the lightest supersymmetric particle, which is absolutely stable. We shall assume that this lightest particle is the lightest neutralino  $\tilde{\chi}_1^0$ . If SUSY is broken at the electroweak scale, the masses of all of these particles should be less than about 1 TeV.

In this section we shall discuss only searches for gluino and squark production. Neutralino, chargino, and slepton production are all important parts of the search for supersymmetry but have smaller cross sections. While MSSM Higgs bosons have rather different production cross sections and decay modes than Standard Model ones, the methods of searching for them are generally similar. Figure 46 shows the regions of MSSM parameter space in which GEM would be able to detect one or more of the neutral Higgs bosons using the  $\gamma\gamma$  and  $\ell^+\ell^-\ell^+\ell^-$  decay channels. The  $\tau^+\tau^-$  decay modes are not shown but appear to offer potential.<sup>80</sup>

### 5.5.1. $\cancel{E}_T$ Signature for Gluinos and Squarks

Since the lightest supersymmetric particle  $\tilde{\chi}_1^0$  is neutral and interacts weakly with matter, it escapes from the detector. Thus, one of the basic signatures for SUSY is missing transverse energy,  $\cancel{E}_T$ , plus multiple jets. A stringent test for GEM's missing energy resolution is to be able to detect, in this mode, gluinos and squarks with masses as light as 300 GeV. This is near the limit expected from the Tevatron and is also the mass range expected in some SUSY grand unified models.<sup>81,82</sup> The MSSM typically produces cascade decays from one supersymmetric particle to another. The events can have many jets and leptons, and the missing energy from the final lightest supersymmetric particle  $\tilde{\chi}_1^0$  can be small compared to the parent mass. A typical decay sequence for a relatively light squark and gluino with  $M_{\tilde{q}} > M_{\tilde{g}}$  might be

$$\begin{aligned}\tilde{u}_L &\rightarrow \tilde{g}u, \\ \tilde{g} &\rightarrow \tilde{\chi}_1^+ \bar{u}d, \\ \tilde{\chi}_1^+ &\rightarrow \tilde{\chi}_1^0 e^+ \nu.\end{aligned}\tag{5.14}$$

Decay chains can be even more complex for heavier masses. All of these possible decays are included in the version of ISAJET<sup>83</sup> used for this analysis.<sup>84</sup>

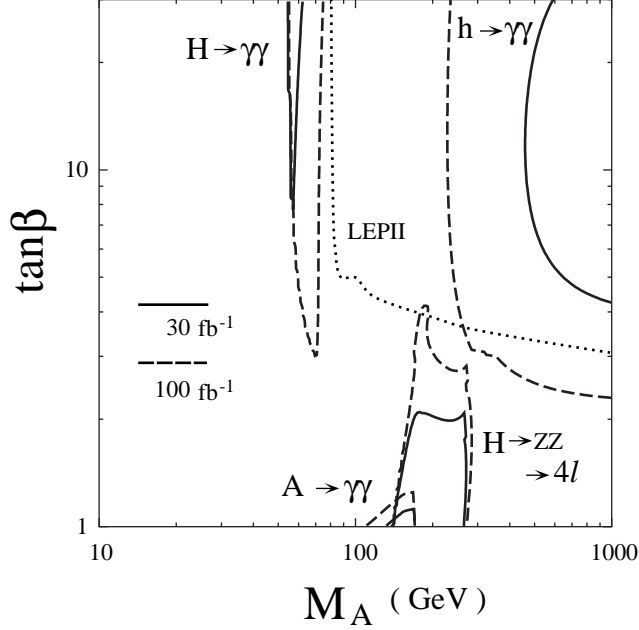


FIG. 46. Regions of the  $(M_A, \tan \beta)$  plane in which GEM could discover the neutral Higgs bosons of the MSSM at the  $5\sigma$  significance level, in the  $\gamma\gamma$  and  $\ell^+\ell^-\ell^+\ell^-$  decay channels, with integrated luminosities of  $30 \text{ fb}^{-1}$  and  $100 \text{ fb}^{-1}$ . Also shown is the region covered by LEP II at  $\sqrt{s} = 190 \text{ GeV}$  with an integrated luminosity of  $500 \text{ fb}^{-1}$ .

Table 9. Choices of MSSM parameters for the three cases considered. These were chosen to have different event topologies and to span the whole mass range. All the squarks and all the sleptons are taken to be degenerate for simplicity. All masses are in GeV. See Ref. 52 for the notation.

Parameter	Case I	Case II	Case III
$M_{\tilde{g}}$	300	350	2000
$M_{\tilde{q}}$	600	325	2500
$M_{\tilde{\ell}}$	500	200	1500
$M_A$	300	300	300
$\mu$	-300	-300	-1000
$\tan \beta$	2	2	2

There are a number of other parameters in the MSSM besides the gluino and squark masses, and it is beyond the scope of this study to explore the MSSM parameter space completely. Instead, the representative choices listed in Table 9 have been considered. Case I has a light gluino and a heavier squark; it is generally similar to the models of Ref. 81 and to the case considered in previous GEM studies.<sup>48</sup> Case II has a squark slightly lighter than the gluino and is generally similar to the models of Ref. 82. Since  $\tilde{g} \rightarrow \tilde{q}q$  dominates for  $M_{\tilde{g}} > M_{\tilde{q}}$ , the signatures in this case are similar to those for squark pair production. One might think that this case would be more difficult to detect because

the events contain just two hard jets from  $\tilde{q} \rightarrow \tilde{\chi}_1^0 q$ . It is actually easier, because the branching ratios for  $\tilde{q}_L \rightarrow \tilde{\chi}_1^\pm q$  and  $\tilde{q}_L \rightarrow \tilde{\chi}_2^0 q$  turn out to be large and to provide multijet signatures, and the dominant decay  $\tilde{q}_R \rightarrow \tilde{\chi}_1^0 q$  gives a harder  $\cancel{E}_T$  distribution. Finally, Case III has all the masses pushed close to the upper limit for SUSY to be related to the electroweak scale. It tests the ability of GEM to cover the top of the plausible mass range for weak-scale supersymmetry.

For the three cases, samples of 70K, 25K, and 35K, respectively, of gluino and squark signal events were generated with a version of ISAJET containing all the MSSM decay modes.<sup>83</sup> The total production cross sections for all combinations of gluinos and squarks are

$$\begin{aligned}
 \text{Case I:} & \quad \sigma = 8.27 \text{ nb}, \\
 \text{Case II:} & \quad \sigma = 7.60 \text{ nb}, \\
 \text{Case III:} & \quad \sigma = 0.81 \text{ pb}.
 \end{aligned}
 \tag{5.15}$$

The Monte Carlo statistics are therefore small compared to those obtained in  $10 \text{ fb}^{-1}$  for the first two cases but comparable in the third. This is reflected in the error bars on the plots shown below.

The signal events are characterized by multiple jets and large missing energy. For the lower masses in Cases I and II the dominant Standard Model physics background comes from heavy flavors decaying into neutrinos, and the dominant detector-induced background comes from mismeasuring QCD jets. A total of 1.5M QCD jets of all types in ten  $p_T$  ranges covering  $50 < p_T < 3200 \text{ GeV}$  was generated with ISAJET to determine both kinds of backgrounds. For the high masses in Case III, the backgrounds from  $W \rightarrow \ell\nu$  and  $Z \rightarrow \nu\bar{\nu}$  are also significant. A total of 40K  $W \rightarrow \ell\nu$  and 80K  $Z \rightarrow \nu\bar{\nu}$  events was generated covering the same  $p_T$  range.

The detector response to all events was simulated with `gemfast`. The missing energy was calculated using the single-particle  $p_T$  resolution of the forward calorimeter determined from GEANT plus an additional 1% nongaussian tail three times as wide as the main peak, as described in Section 4.3. The effect of this nongaussian tail is small compared to the effects of angular resolution in the forward calorimeter and of the hole for the beam pipe, so its exact parameterization is not crucial.

In the inclusive  $\cancel{E}_T$  cross section, the Standard Model physics background is larger than the signal. Furthermore, the detector-induced background from mismeasured jets in the forward region is several times larger than the real neutrino background, even for an ideal calorimeter covering  $\eta < 5.5$ .<sup>85</sup> First consider the lower-mass Cases I and II. Since gluinos and squarks are centrally produced with  $p_T \sim M_{\tilde{g}}$ , they give multiple jets and “round” events in addition to  $\cancel{E}_T$ . Jets with  $p_T > 75 \text{ GeV}$  were found using the `gemfast` fixed cone algorithm with  $R = 0.7$ . The minimum number of jets,  $N_{\text{jet}}$ , was varied between two and five. To identify round events, the sphericity in the transverse momentum plane,  $S_T$ , was calculated by summing all calorimeter cells with  $E_T > 0.5 \text{ GeV}$  and  $|\eta| < 3$ . A

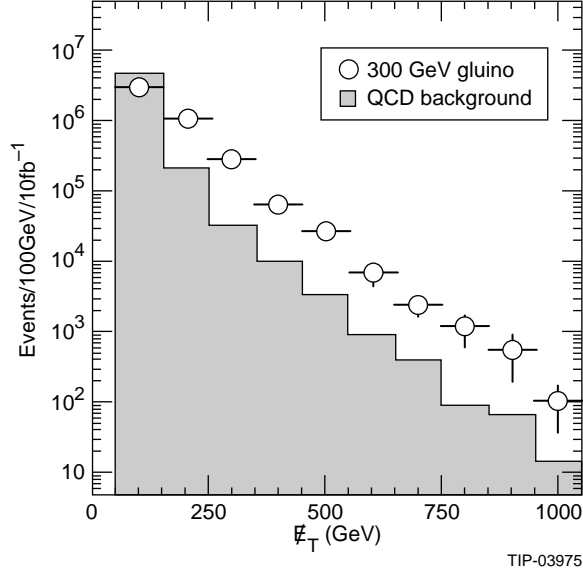


FIG. 47.  $\cancel{E}_T$  signal for Case I MSSM parameters defined in Table 9 (open circles) and for QCD background (histogram) after requiring at least 5 jets with  $p_T > 75$  GeV and the sphericity and lepton veto cuts described in the text.

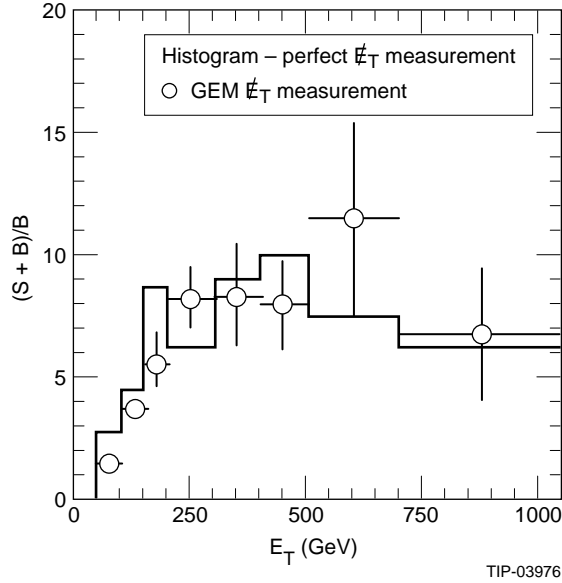


FIG. 48. Open circles: Ratio of signal and background curves from Fig. 47. Histogram: The same ratio for a perfect  $\cancel{E}_T$  measurement.

cut on  $S_T > 0.2$  provided good separation of signal and background. After these cuts the signal to background ratio  $S/B$  for  $\cancel{E}_T \sim 250$  GeV was about 3 for Case I and about 5 for Case II. The larger  $S/B$  for Case II reflects the harder  $\cancel{E}_T$  spectrum from  $\tilde{q}_R$  decays mentioned earlier.

Semileptonic decays of gluinos and squarks are important; see Section 5.3.2 below.

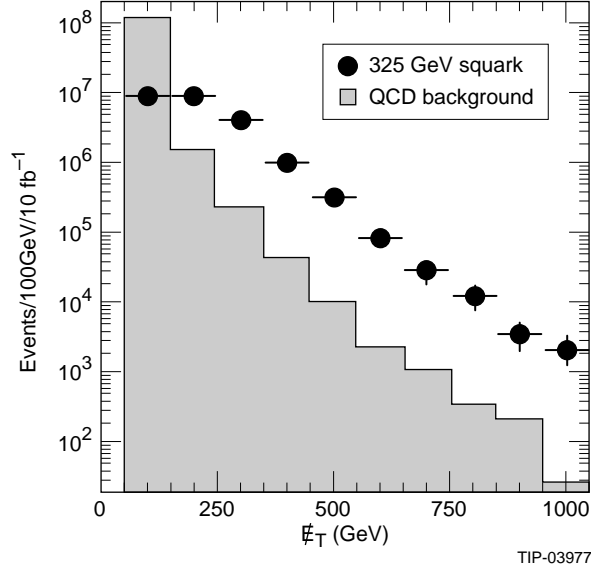


FIG. 49.  $\cancel{E}_T$  signal for Case II MSSM parameters defined in Table 9 (solid circles) and for QCD background (histogram) after requiring at least 2 jets with  $p_T > 75$  GeV and making the sphericity and lepton veto cuts described in the text.

However, a lepton veto further improves the  $S/B$  for the  $\cancel{E}_T$  distribution by rejecting  $t\bar{t}$  and other Standard Model backgrounds. Events were vetoed if they contained a muon or an isolated electron. An electron was identified as an isolated electromagnetic cluster in the calorimeter with  $p_T > 20$  GeV and  $|\eta| < 2.5$ , matched to a single track in the central tracker with a loose matching constraint,

$$|E/p - 1| < \max(0.5, 3\frac{\Delta p}{p}). \quad (5.16)$$

Isolated muons with  $p_T > 20$  GeV and  $|\eta| < 2.5$  were identified using the standard `gemfast` muon reconstruction. The efficiency of the lepton identification is not crucial for this analysis; even if it were perfect, there still would be background from  $\tau$ -decays of  $b$  and  $t$  quarks.

The signal and background  $\cancel{E}_T$  distributions for Case I with at least five jets and the sphericity and lepton veto cuts described above are shown in Fig. 47. The  $(S+B)/B$  ratio, shown in Fig. 48, reaches about 8 for  $\cancel{E}_T = 250$  GeV. Figure 48 also shows the  $(S+B)/B$  ratio obtained using  $\cancel{E}_T$  calculated from the the missing  $\nu$  and  $\tilde{\chi}_1^0$  momenta, with the rest of the analysis unchanged. While the GEM calorimeter performance increases the background at low  $\cancel{E}_T$ , it is about as good as that of a perfect detector in the region for which the ratio is large.

Figure 49 shows the signal and background for Case II, requiring at least two jets with  $p_T > 75$  GeV and the same sphericity and lepton veto cuts. For this case the direct decay  $\tilde{q}_R \rightarrow \tilde{\chi}_1^0 q$  dominates and leads to a significantly harder  $\cancel{E}_T$  spectrum and to lower jet multiplicity. The  $(S+B)/B$  ratio is even larger in this case. Figure 50 plots the signals for

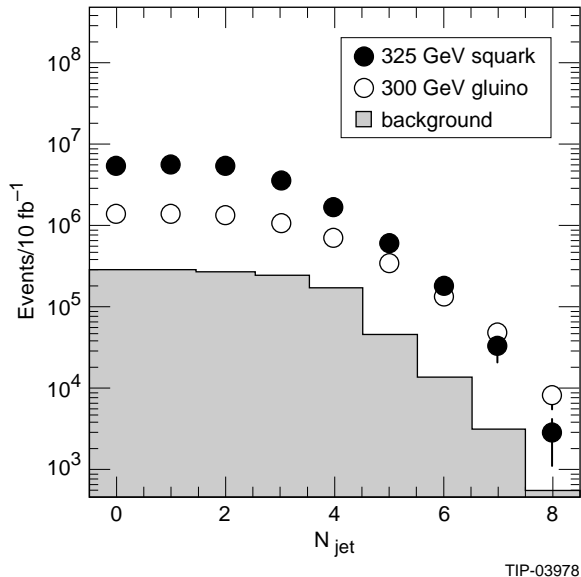


FIG. 50. Event numbers with  $\cancel{E}_T > 250$  GeV and the sphericity and lepton veto cuts described in the text vs. the minimum number  $N_{\text{jet}}$  of jets with  $p_T > 75$  GeV. Open circles: Case I signal. Solid circles: Case II signal. Histogram: QCD background. Case II has more events with low jet multiplicity because  $\tilde{q}_R \rightarrow \tilde{\chi}_1^0 q$  dominates.

Cases I and II and the Standard Model background for  $\cancel{E}_T > 250$  GeV and  $S_T > 0.2$  vs. the minimum number,  $N_{\text{jet}}$ , of jets with  $p_T > 75$  GeV. Both signals and backgrounds are constant for  $N_{\text{jet}} \leq 2$  because it is impossible to have a large sphericity with only one jet. The signal falls off faster with increasing  $N_{\text{jet}}$  for Case II than for Case I because  $\tilde{q}_R \rightarrow \tilde{\chi}_1^0 q$  is dominant and gives a large rate for two jets plus  $\cancel{E}_T$ . Thus, the  $N_{\text{jet}}$  dependence provides a handle to distinguish among models.

Given the large number of signal events, the statistical significance of the signals is not an issue. The  $t$ ,  $W$  and  $Z$  backgrounds can be checked using isolated lepton samples; the  $b$  and  $c$  backgrounds can be checked using muons in jets. The  $\cancel{E}_T$  resolution of the detector can be studied using inclusive data on QCD jets and on  $\gamma + \text{jets}$  events. Given all these constraints, the background should be reliably known, so observation of a signal 5–10 times that expected from the Standard Model should be very convincing. The difficult problem of extracting the masses and other model parameters is briefly discussed in Section 5.3.3.

For heavy gluino and squark masses such as those in Case III,  $\cancel{E}_T$  is so large that the  $\cancel{E}_T$  resolution is not important. Figure 51 shows the signal and background  $\cancel{E}_T$  distributions for Case III with at least four jets having  $p_T > 300$  GeV and with the sphericity and lepton veto cuts identical to those for lighter masses. Heavy flavor backgrounds, detector-induced backgrounds from mismeasured QCD jets, and  $W$  and  $Z$  backgrounds are included. The QCD background dominates for low  $\cancel{E}_T$  but falls more rapidly than the  $W$  and  $Z$  backgrounds, and so all must be considered. Since several hundred signal events survive these cuts with large  $S/B$ , it is evident that with an integrated luminosity of  $10 \text{ fb}^{-1}$  GEM

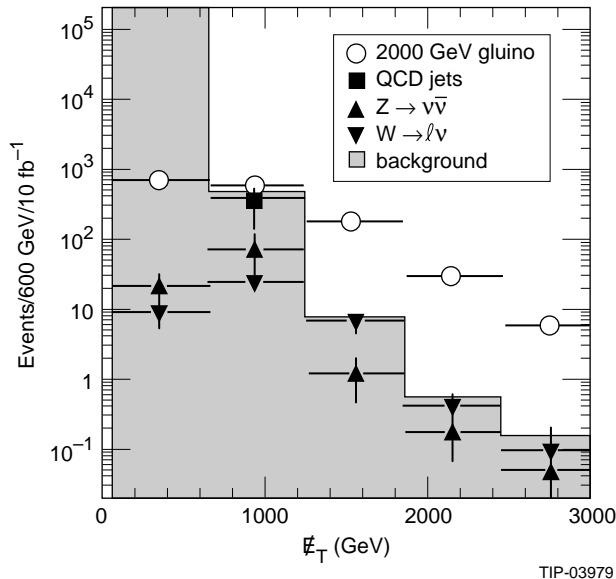


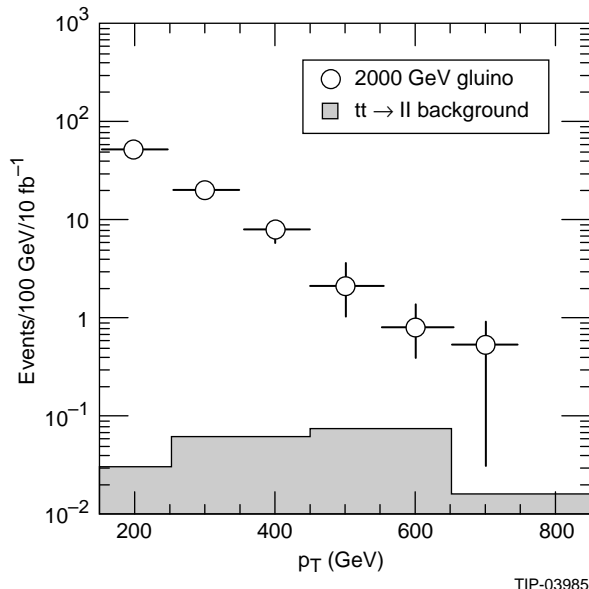
FIG. 51.  $\cancel{E}_T$  signal for Case III MSSM parameters defined in Table 9 after requiring at least 4 jets with  $p_T > 300$  GeV and making the sphericity and lepton veto cuts described in the text. Open circles: Signal. Solid squares: QCD background. Triangles:  $W \rightarrow \ell\nu$  and  $Z \rightarrow \nu\bar{\nu}$  backgrounds. Histogram: Sum of all backgrounds.

could discover SUSY in this channel up to masses of order 2 TeV, about the upper limit if SUSY is related to electroweak symmetry breaking.

### 5.5.2. Leptonic Signatures

In addition to the  $\cancel{E}_T$  plus multijet signatures described above, there are many other signatures for supersymmetry, including a number involving two or more leptons.<sup>86</sup> In particular, since the gluino is a self-conjugate Majorana fermion,  $\tilde{g}\tilde{g}$  and  $\tilde{g}\tilde{q}$  pairs can give isolated  $\ell^\pm\ell^\pm$  pairs. Observing such like-sign pairs is essential for establishing the Majorana nature of any gluino signal. It also helps in separating gluinos and squarks. The dominant standard model  $\ell^\pm\ell^\pm$  background is expected to be from  $t\bar{t}$  events in which either a  $b \rightarrow \ell X$  lepton appears isolated or an isolated lepton sign is wrongly determined. These backgrounds, calculated previously in Ref. 86, are found to be negligible. For light gluinos, such as those in Cases I and II, the cross sections are so large that it is sufficient to use only the  $\mu^\pm\mu^\pm$  channel, for which the lepton signs are very well determined in GEM. Therefore, only the issue of measuring the signs of electrons from Case III is addressed here.

The same sample of Case III signal events described in the previous subsection was used for this analysis. While it is possible to enhance the leptonic sample by forcing a particular decay chain, e.g.  $\tilde{g} \rightarrow \tilde{\chi}_1^\pm q\bar{q}'$ ,  $\tilde{\chi}_1^\pm \rightarrow \tilde{\chi}_1^0 \ell^\pm \nu$ , there are many such chains possible, no one of which obviously dominates. It was therefore decided to use the inclusive sample. For the background, only  $t\bar{t}$  events, which are expected to dominate, were considered. A total sample of 30K  $t\bar{t}$  events in ten bins with  $50 < p_T < 3200$  GeV were generated, forcing



TIP-03985

FIG. 52.  $p_T$  distributions for the highest- $p_T$  isolated lepton in dilepton events containing two isolated like-sign leptons. Open circles: Signal events generated with Case III MSSM parameters. Histogram:  $t\bar{t}$  background from mismeasured electrons in the GEM central tracker.

the decays  $t \rightarrow e^+ \nu_e b$  and  $\bar{t} \rightarrow \mu^- \bar{\nu}_\mu \bar{b}$ . This sample was used to determine the principal detector-induced background, that from misidentification of  $e^\pm$  signs in the central tracker. From this, the total  $\ell^\pm \ell^\pm$  background was determined.

Electrons and muons with  $p_T > 50$  GeV and  $|\eta| < 2.5$  were identified using the relatively loose cuts described in the previous subsection. These cuts, optimized for background rejection rather than for signal detection, appear to be adequate to identify this signal. At least two such leptons were required satisfying the isolation criterion

$$\sum'_{R=0.2} E_T < 0.1 p_{T\ell} + 5 \text{ GeV}. \quad (5.17)$$

Here, the prime on the sum indicates that the lepton itself is not included. This cut effectively rejects<sup>86</sup> the background from  $t \rightarrow \ell^+ \nu b$  and  $\bar{t} \rightarrow \bar{\ell} X$ ,  $\bar{b} \rightarrow \ell^+ X$ . In addition a missing energy  $\cancel{E}_T > 500$  GeV and a transverse sphericity  $S_T > 0.2$  were required. After these cuts, the total dilepton rates for the signal and for the  $t\bar{t}$  background were comparable, so a very large rejection of unlike-sign pairs is not needed.

Figure 52 shows the transverse momentum distribution of the highest  $p_T$  lepton in like-sign dilepton events satisfying the above cuts. The lepton spectrum is soft relative to the gluino mass because the leptons arise from cascade decays. Figure 52 also shows the  $t\bar{t} \rightarrow \ell^+ \nu b \ell^- \bar{\nu} \bar{b}$  background in which an electron sign is mismeasured by the GEM central tracker. The probability of mismeasurement was determined using the `gemfast` parameterization of the central tracker electron resolution, including the tail from bremsstrahlung, as described

in Section 4.2. Muon signs are assumed perfectly determined, an excellent approximation at these momenta. Since the cuts not dependent on the electron sign reduce the background to the order of the signal, and since most of the signal leptons have  $p_T < 600$  GeV, for which the central tracker determines signs with 95% reliability, it is not surprising that the background is small compared to the signal. The signal comprises several tens of events per  $10 \text{ fb}^{-1}$  when both electrons and muons are combined. It would be uncomfortably small if one had to rely on only the  $\mu^\pm \mu^\pm$  signal, which is a factor of four smaller.

### 5.5.3. SUSY Parameter Determination

In the MSSM there are at least eight mass parameters ( $M_{\tilde{g}}, M_{\tilde{q}}, M_{\tilde{t}_L}, M_{\tilde{t}_R}, M_{\tilde{\ell}_L}, M_{\tilde{\ell}_R}, M_{\tilde{\nu}_L}$ , and  $M_A$ ), two additional parameters related to the Higgs sector ( $\mu$  and  $\tan \beta$ ), and still more parameters related to  $\tilde{t}$  decay. Nonminimal SUSY models have even more parameters. Since all supersymmetric particles in the MSSM ultimately decay into the  $\tilde{\chi}_1^0$ , which is invisible, it is not possible to reconstruct any masses directly.

The approximate mass scale can be inferred from the  $\cancel{E}_T$  scale at which the signal deviates from the standard model background, as can be seen by comparing Figs. 47, 49, and 51. The mean  $\cancel{E}_T$  for the distribution of the excess of events can be calculated very accurately for low masses because of the high statistics. However, the relationship of this mean to the masses is model dependent. For example, the missing energy is lower and the jet multiplicity is higher if  $M_{\tilde{q}} > M_{\tilde{g}}$  than if  $M_{\tilde{g}} > M_{\tilde{q}}$ .

A large number of possible signatures may be used to determine the parameters. These include the  $\cancel{E}_T$  cross section with multiple leptons,<sup>86</sup> multilepton cross sections arising from production of  $\tilde{\chi}_1^\pm \tilde{\chi}_2^0 \rightarrow 3\ell$  and similar channels, and the observed cross sections or limits for  $h, H \rightarrow \gamma\gamma$ ;  $h, H \rightarrow 4\ell$ ; and  $t \rightarrow H^+b$ . The tools to simulate these signatures have recently been developed,<sup>83</sup> and the methods to determine all of the MSSM parameters from these signatures are being studied. However, it is clear from the previous two subsections that a detector such as GEM, with reasonable calorimetry out to  $\eta \simeq 5.5$  and tracking capabilities for charged leptons, is capable of observing clean samples of events in the relevant channels.

## 5.6. High Mass Physics at Ultrahigh Luminosity

While the studies presented above show that, at the SSC design energy of 40 TeV, the standard integrated luminosity of  $10 \text{ fb}^{-1}$  is sufficient for a wide range of interesting physics, there remain many potential new physics signals which require an integrated luminosity of order  $100 \text{ fb}^{-1}$ . Practically speaking, this requires extended running at  $\mathcal{L} \simeq 10^{34} \text{ cm}^{-2} \text{ s}^{-1}$ . These new physics opportunities are almost all at very high mass scales, with effective cross sections of order  $1 - 10 \text{ fb}$ . Examples include multi-TeV, weakly coupled  $Z'$  and  $W'$  bosons, quark-lepton substructure, and very massive technirho vector bosons. In these and most other examples, the new physics is signalled by an excess of well-isolated leptons at high  $p_T$ . Robust and accurate measurement of such leptons was a primary design goal of GEM, as it is for the LHC detectors.

This section demonstrates the capacity of GEM at ultrahigh luminosity for precision measurements of the masses, widths and chiral couplings of 4 TeV  $Z'$  bosons via  $e^+e^-$  and  $\mu^+\mu^-$  final states and for the discovery and study of quark-lepton substructure at the scale  $\Lambda = 25$  TeV in Drell-Yan production of high-mass dimuons. For both, we show that the GEM design permits distinguishing different models with a data sample of  $100 \text{ fb}^{-1}$ . We also find that the reach of the GEM detector is  $M_{Z'} \simeq 8$  TeV for new gauge bosons and  $\Lambda = 30 - 35$  TeV for quark-lepton substructure. Finally, we briefly describe approaches to studying high-mass  $W'^{\pm} \rightarrow \ell^{\pm}\nu_{\ell}$  and quark-lepton substructure in  $\bar{q}q' \rightarrow \mu^{\pm}\nu_{\mu}$ . We believe these are interesting because they effectively allow high-mass studies even when there is a neutrino and even when there is no well defined subsystem invariant mass.<sup>87</sup>

The isolated high-energy lepton signals of these and most other new physics processes are relatively free of physics backgrounds. For example, a rejection factor of  $\mathcal{R}(e/\text{jet})$  of  $\mathcal{O}(10^{-4})$  reduces the jet backgrounds to  $Z' \rightarrow e^+e^-$  to the level of a few percent. Straightforward isolation cuts on muons completely remove the main physics backgrounds to  $\bar{q}q \rightarrow \mu^+\mu^-$ . The most stringent requirements will be reliable operation of the trigger and detector and pattern recognition at such high luminosities.

### 5.6.1. Precision Studies of New Heavy $Z'$ Gauge Bosons

Extensions of the standard electroweak gauge group,  $SU(2) \otimes U(1)$ , involve additional neutral gauge bosons  $Z'$  and sometimes charged  $W'^{\pm}$  vector bosons. In the models of interest, the new weak bosons couple to quarks and leptons with strength of  $\mathcal{O}(e)$ . In one year of running at  $\mathcal{L} = 10^{33} \text{ cm}^{-2} \text{ s}^{-1}$ , one could observe  $M_{Z'} \simeq 4 - 6$  TeV, with 10  $Z' \rightarrow e^+e^-$  events in a narrow  $M_{e^+e^-}$  range where none are expected.<sup>11</sup> If such a boson were found, high-statistics studies would be needed to determine its nature. This subsection considers a 4 TeV  $Z'$  boson. For this mass, hundreds of events would be detected per year at ultrahigh luminosity. Since the couplings of such  $Z'$  bosons must be flavor-conserving, they may be detected in both  $Z' \rightarrow e^+e^-$  and  $Z' \rightarrow \mu^+\mu^-$  modes. Very precise measurements of the  $Z'$  mass and width can be made via the  $e^+e^-$  decay. As we shall describe below, the chiral nature of the  $Z'$  couplings to quarks and leptons can be investigated in the  $\mu^+\mu^-$  mode by measuring the distribution in the angle  $\theta$  between the outgoing  $\mu^-$  and the incoming quark.

The goal of the studies presented here is to determine GEM's ability to distinguish two different  $Z'$  models by the bosons' widths and angular distributions. The two models considered were:

1. A left-right model, in which  $SU(2)_L \otimes SU(2)_R \otimes U(1)$  breaks down to  $SU(2)_L \otimes U(1)$ . The  $SU(2)_R$  coupling constant was taken to be the same as the  $SU(2)_L$  one. The extra  $Z$ -boson of this model is called  $Z_1$  below.
2. A model in which the grand unification group  $SO(10)$  breaks down to  $SU(5) \otimes U(1)$ , then to  $SU(2)_L \otimes U(1)$ . Such a model may have an extra  $Z' \equiv Z_2$  well below the

unification scale.

The left- and right-handed couplings to quarks and leptons in the two models are given by

$$\begin{aligned}
g_{uL} &= \beta, & g_{uR} &= \beta + \gamma; \\
g_{dL} &= \beta, & g_{dR} &= \beta - \gamma; \\
g_{\nu L} &= -3\beta, & g_{\nu R} &= -3\beta + \gamma; \\
g_{\ell L} &= -3\beta, & g_{\ell R} &= -3\beta - \gamma.
\end{aligned}
\tag{5.18}$$

The parameters  $\beta$  and  $\gamma$  are

$$\begin{aligned}
\beta &= 0.0528, & \gamma &= -0.3630 && \text{(Model 1)} \\
\beta &= 0.0979, & \gamma &= -0.1958 && \text{(Model 2)}.
\end{aligned}
\tag{5.19}$$

In calculating the  $Z'$  decay widths, it is assumed that there are three generations of quarks and leptons and that right-handed neutrinos exist and are much lighter than  $M_{Z'}$ . If there are no other significant decay modes, the widths are given by

$$\Gamma(Z' \rightarrow f_i \bar{f}_i) = \frac{2\alpha M_{Z'} C_i}{3 \sin^2 2\theta_W} (g_{iL}^2 + g_{iR}^2),
\tag{5.20}$$

where  $C_i = 3$  for quarks and 1 for leptons. The full widths in the two models are  $\Gamma(Z_1) = 105 \text{ GeV}$  and  $\Gamma(Z_2) = 67.7 \text{ GeV}$ .

### $Z' \rightarrow e^+e^-$

PYTHIA 5.6 was used to generate 3000 events for each of the two  $Z'$  models, including full  $\gamma/Z/Z'$  interference.<sup>88</sup> Pileup at  $\mathcal{L} = 10^{34} \text{ cm}^{-2} \text{ s}^{-1}$  was simulated by merging with the hard scattering process a set of minimum bias events. The latter were Poisson-distributed, with a mean number of 16 events per beam crossing. The total signal cross sections for  $3.75 \text{ TeV} < M_{e^+e^-} < 4.25 \text{ TeV}$  are 5.44 fb for Model 1 and 4.54 fb for Model 2. No rapidity cut was imposed on the generated events.

All tracks found by the central tracker (which, at  $10^{34} \text{ cm}^{-2} \text{ s}^{-1}$ , has its inner silicon layers removed, leaving 8 planes of tracking) were processed and a most likely  $Z'$  vertex was found using momentum-weighted  $z$  locations. Then the  $5 \times 5$  towers in the EM calorimeter were examined. Electron candidate towers were required to satisfy the following criteria:

1.  $|\eta| < 2.46$  so as to be within the tracker's coverage. Electrons falling in the transition region between barrel and endcap ( $1.01 < |\eta| < 1.16$ ) were excluded because their energies are not as precisely measured. The geometrical acceptance of the detector for the  $Z' \rightarrow e^+e^-$  events is 78%.
2.  $E_T > 250 \text{ GeV}$  in a  $5 \times 5$  tower in the EC; 99.4% of the events with  $|\eta| < 2.46$  passed this cut.

3. Transverse energy leakage into the  $3 \times 3$  HC tower behind the  $5 \times 5$  EC tower less than 5% of the energy in the EC tower; 99.2% of the remaining events passed this selection. If a high energy EC cluster was isolated at this level, any energy in the first layer of the HC behind the cluster was added to the EC energy to improve the resolution.
4. A charged track candidate with  $p_T > 1 \text{ GeV}$  must be within  $R = 0.0632$  ( $\Delta\eta = 0.06 \times \Delta\phi = 0.02$ ) of the centroid of the EC tower. Essentially all electron candidates passed this cut. Much tighter track restrictions will be imposed below to reduce jet backgrounds.
5. A calorimetric isolation cut of

$$\sum_{R=0.55} E_T < 1.15 \sum_{5 \times 5} E_T(\text{EC}). \quad (5.21)$$

was applied. This accepted 99.6% of the signal events.

The trigger efficiency for these events is close to 100%. Thus, GEM would collect 415  $Z_1 \rightarrow e^+e^-$  and 350  $Z_2 \rightarrow e^+e^-$  events per  $100 \text{ fb}^{-1}$  run.

Backgrounds to the  $Z' \rightarrow e^+e^-$  signal come from misidentifying jets as electrons in QCD jet production and in  $pp \rightarrow W + \text{jets}$  with  $W \rightarrow e\nu$ . They may also come from isolated, high-mass  $e^+e^-$  pairs from  $\bar{t}t$  production. The cross section for QCD jets with  $|\eta| < 2.46$  and invariant mass  $M_{jj} = 4000 \pm 250 \text{ GeV}$  is 704 pb. The corresponding cross section for  $W + \text{jets} \rightarrow e + \text{jets}$  is about 25 fb. The rate for  $\bar{t}t \rightarrow e^+e^- + X$  with generated  $M_{\bar{t}t} > 3.5 \text{ TeV}$  and  $p_T(t, \bar{t}) > 100 \text{ GeV}$  is 20.4 fb, for  $m_t = 140 \text{ GeV}$ .

To be considered as background electron candidates, jets had to have  $E_T > 200 \text{ GeV}$ , one or two charged tracks in a cone of  $\Delta\eta \times \Delta\phi = 0.09 \times 0.03$  about the jet direction, and at least one charged track with  $p_T > 50 \text{ GeV}$ . This reduced a generated sample of 120K jets to 9360 (in 8890 events). These were then subjected to the cuts used to select electron candidates and 26 jets passed. This implies a jet rejection factor of  $\mathcal{R}(e/\text{jet}) \simeq 2.9 \times 10^{-4}$  at the 95% confidence level. The surviving dijet rate is 0.06 fb, less than 2% of the accepted signal rate. The  $W + \text{jet}$  background is negligible. After the isolation cut, the  $\bar{t}t \rightarrow e^+e^- + X$  background is completely eliminated by requiring  $M_{e^+e^-} > 3.5 \text{ TeV}$ . (See the discussion below of the  $\bar{t}t \rightarrow \mu^+\mu^- + X$  background to  $Z' \rightarrow \mu^+\mu^-$ .) When the requirement of exactly one *reconstructed* track with  $p_T > 50 \text{ GeV}$  was applied to the  $Z'$  candidates, 83% of the events passed, for a net acceptance of 64%.

The  $e^+e^-$  mass resolution depends on the resolutions in both the electron energy and angle (see Eq. (5.3)). In the EC energy resolution, only the constant term matters for a 4 TeV  $Z'$ . For the GEM baseline, this is 0.4%. (Any bremsstrahlung from the passage of the very high energy electrons through the CT material enters the same  $5 \times 5$  EC tower which defines the electron shower and so does not affect the resolution.) For the high energies of interest here, the  $e^+$  and  $e^-$  directions can be determined to an accuracy of about

2.4 mrad using the longitudinal segmentation in the EC. This gives  $\Delta\theta = 3.4$  mrad. The angular resolution can be significantly improved by using the tracker. The vertex location found using the two highest- $E_T$  electrons has a resolution of 1.5 mm, while the EC hit location has a resolution of 0.25 mm for such high energy showers. The resulting angular resolution is  $\Delta\theta = 1.5$  mrad. Then, since the typical opening angle between the electrons is greater than  $60^\circ$ ,  $\Delta M_{e^+e^-} \simeq 0.003 \times M_{Z'}$ , dominated by the EC energy resolution. This is appreciably less than  $\Gamma_{Z'}/2.35$  for the two models under consideration. Indeed, models in which the  $Z'$  width was artificially made as small as 25 GeV were considered and the width was shown to be resolvable.<sup>88</sup>

Several luminosity-dependent effects were considered that might affect the  $M_{e^+e^-}$  resolution.<sup>88</sup> Pileup noise in the calorimeters is unimportant. The effect of pileup tracks on the performance of the tracker for the purpose of vertex determination was included.

Figures 53 and 54 show the  $M_{e^+e^-}$  distributions for the two  $Z'$  models as generated by PYTHIA and as reconstructed by **gemfast**. The data in these figures correspond to about  $200 \text{ fb}^{-1}$ . These distributions are fit very well by a Lorentzian. The reconstructed masses determined from this fit are within 2 GeV of the generated 4 TeV. The reconstructed widths are  $\Gamma_{Z_1} = 123.0 \pm 5.2 \text{ GeV}$  and  $\Gamma_{Z_2} = 88.5 \pm 4.3 \text{ GeV}$ . These are to be compared with the generated widths of  $116.4 \pm 5.0 \text{ GeV}$  for  $Z_1$  and  $80.9 \pm 3.9 \text{ GeV}$  for  $Z_2$ .<sup>89</sup> Within errors, the generated and reconstructed widths differ by an amount that corresponds to the detector resolution estimated above. This was verified for the artificially narrow  $Z'$  models. While the error in  $\Gamma_{Z'}$  will be dominated by statistics, the main error in  $M_{Z'}$  will be systematic, arising from possible nonlinearity in the EM energy scale in the TeV region.

Finally, we estimated the reach of the GEM detector in  $M_{Z'}$  for a 40 TeV  $pp$  collider with integrated luminosity  $100 \text{ fb}^{-1}$ . Assuming that ten detected  $Z' \rightarrow e^+e^-$  events are sufficient for discovery (there is no background after cuts), the reach was found to be about 8 TeV for both models considered. The reach for other models may be more or less by 1 – 2 TeV. This high mass, then, was used to set the upper end of the dynamic range of the GEM electromagnetic calorimeter.

### $Z' \rightarrow \mu^+\mu^-$

The chiral couplings of  $Z'$  bosons to quarks and leptons determine the lepton angular distribution. Thus, the  $\cos\theta$  distribution ( $\theta$  is the angle between the incoming quark and outgoing  $\mu^-$ ) can help distinguish alternative models. The angles and charges of high energy muons can be measured reliably even at ultrahigh luminosity. We imposed the criterion that muon charges must be known with at least  $2.5\sigma$  significance. At least 99% of the signal events that passed the isolation and invariant mass cuts described below have the charges of both muons determined. Events with one mismeasured sign were rejected. The probability of two mismeasured signs is  $\mathcal{O}(10^{-4})$  and no such events are expected in a data sample of  $100 \text{ fb}^{-1}$ .

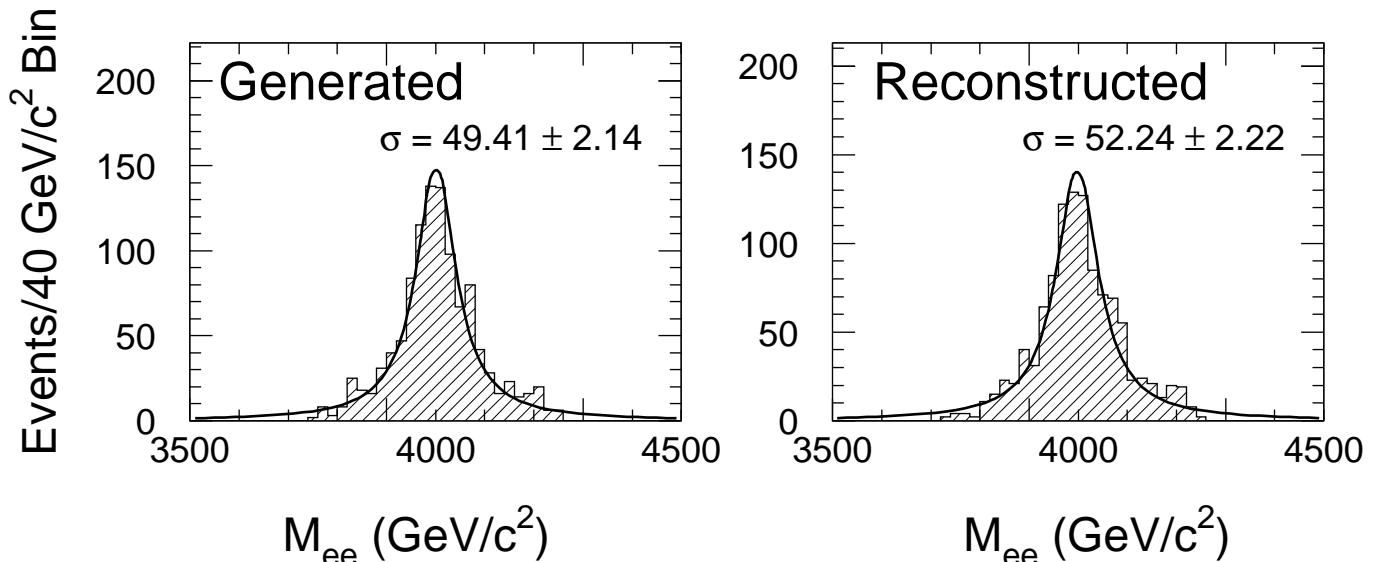


FIG. 53. The  $M_{e^+e^-}$  distribution for a 4 TeV mass  $Z'$  of Model 1 as described in the text. Shown are the generated mass distribution (all events within acceptance) and the reconstructed distribution (passing geometric and calorimetric cuts 1–5). The number of events corresponds to  $200 \text{ fb}^{-1}$ .

To measure the  $\cos \theta$  distribution, one must determine, in addition to the muons' charges and directions, the direction of the incoming quark in the lab. The procedure usually followed in these studies has been to determine the (valence) quark direction by requiring that the  $Z'$  be produced at large rapidity,  $\eta_{Z'} \gtrsim 1$ .<sup>90</sup> Only about 20% of the heavy  $Z' \rightarrow \mu^+\mu^-$  events would pass this cut. We found it better to use all the events and plot the distribution in

$$\cos \theta^* = \text{sgn}(\eta_B) \tanh \left( \frac{\eta_{\mu^-} - \eta_{\mu^+}}{2} \right). \quad (5.22)$$

where  $\eta_B = \frac{1}{2}(\eta_{\mu^-} + \eta_{\mu^+})$  is the boost rapidity of the  $\mu^+\mu^-$  center-of-mass frame.<sup>47,48,91</sup> For  $\sqrt{\hat{s}} > 2 \text{ TeV}$ , the quark distribution is so much harder than the antiquark distribution that  $\text{sgn}(\eta_B)$  determines the correct quark direction at least 75% of the time. Then  $\theta^* \approx \theta$ , since the  $p_T$  of the c.m. system is generally much less than  $\sqrt{\hat{s}}$ .

PYTHIA 5.6 was used to generate 1000 events of  $Z' \rightarrow \mu^+\mu^-$  with  $|M_{\mu^+\mu^-} - M_{Z'}| < 250 \text{ GeV}$  for each of the two models described in the previous subsection. The cross sections in this simulation were found to be  $\sigma(Z_1 \rightarrow \mu^+\mu^-) = 5.86 \text{ fb}$  and  $\sigma(Z_2 \rightarrow \mu^+\mu^-) = 4.49 \text{ fb}$ . The geometrical acceptance of the muon system for all events was found to be 63% for both models; for muons with  $|\eta| < 2.46$ , it is about 70%. For these muons, the trigger

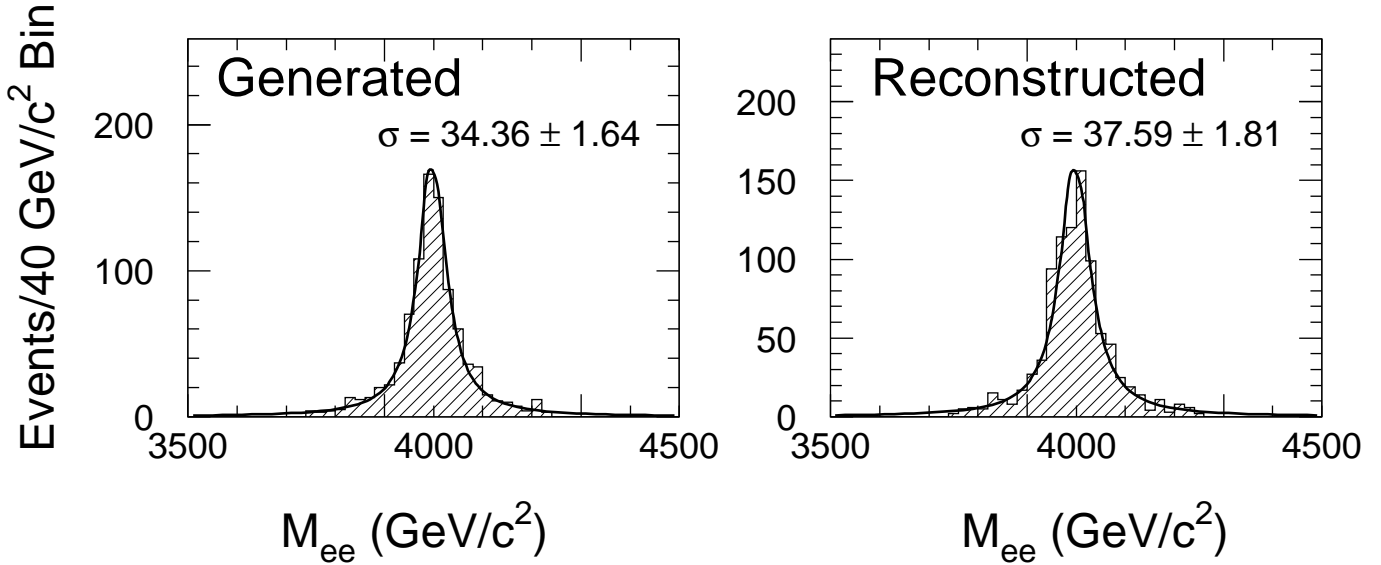


FIG. 54. The  $M_{e^+e^-}$  distribution for a 4 TeV mass  $Z'$  of Model 2 as described in the text. Shown are the generated mass distribution (all events within acceptance) and the reconstructed distribution (passing geometric and calorimetric cuts 1–5). The number of events corresponds to  $200 \text{ fb}^{-1}$ .

was highly efficient. Thus, before any additional losses, a data sample of  $100 \text{ fb}^{-1}$  yields 375  $Z_1 \rightarrow \mu^+\mu^-$  and 285  $Z_2 \rightarrow \mu^+\mu^-$  events. A study of the muon system's geometrical acceptance for these  $Z'$  events was carried out using a full GEANT simulation, with results essentially identical to those obtained here with `gemfast`.

The only physics backgrounds to the  $Z'$  signal are continuum Drell-Yan production and  $t\bar{t} \rightarrow \mu^+\mu^- + X$ . After momentum smearing is included, the signal region used for angular distribution studies was taken to be  $3.2 \text{ TeV} < M_{\mu^+\mu^-} < 4.8 \text{ TeV}$ . The Drell-Yan background was studied by generating 4000  $\gamma/Z/Z'$  events with  $M_{\mu^+\mu^-} > 1.5 \text{ TeV}$ . Drell-Yan production contributed six background events to the signal region.

The  $t\bar{t} \rightarrow \mu^+\mu^- + X$  background was studied by generating 200K events with generated  $M_{t\bar{t}} > 1.4 \text{ TeV}$  and  $p_T(t, \bar{t}) > 100 \text{ GeV}$ . The rate for this background is 1.4 pb, so the sample corresponds to  $140 \text{ fb}^{-1}$ . (Other potential backgrounds, such as  $tW$  and  $WW$  production have very much smaller rates.) Detector response to events having  $M_{\mu^+\mu^-} > 1 \text{ TeV}$  and  $|\eta_\mu| < 2.6$  at the generator level was simulated with `gemfast`. There were 2900 such events (for  $100 \text{ fb}^{-1}$ ), of which 2700 passed the geometrical acceptance simulated in `gemfast`. This is higher than the geometrical acceptance for  $Z' \rightarrow \mu^+\mu^-$  events because most of the muons from  $t$ -decay follow their parent's direction, which is fairly close to the beam, i.e.,

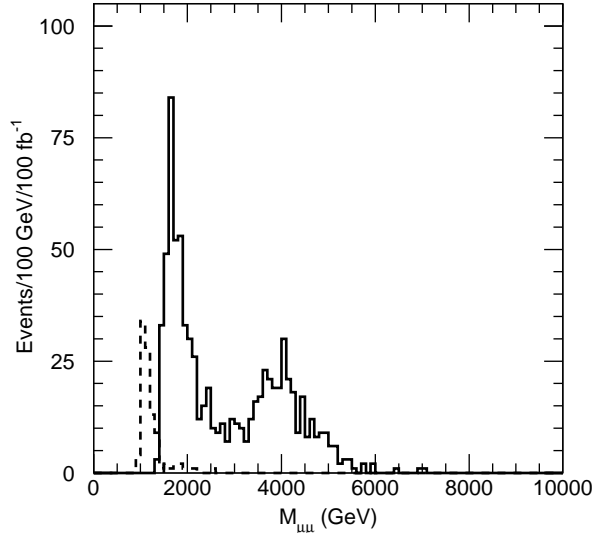


FIG. 55. The  $M_{\mu^+\mu^-}$  distribution for the Drell-Yan continuum and  $Z_2 \rightarrow \mu^+\mu^-$ . The  $t\bar{t} \rightarrow \mu^+\mu^- + X$  background before the invariant mass cut is also shown (dashed).

away from the dead region near  $\eta = 0$ . Since these muons are usually accompanied by hadronic debris, the background can be removed by a combination of isolation and  $M_{\mu^+\mu^-}$  cuts.

An isolation cut using a large cone

$$\sum_{R=0.7} E_T < 0.1 p_T(\mu) \quad (5.23)$$

was made. Here, the sum is over energy in the full calorimeter and  $p_T(\mu)$  is the muon momentum corrected for energy loss in the calorimeter. This cut rejects 96.5% of the  $t\bar{t}$  background while retaining 94% of the  $Z'$  events. All these events had identified muon charges. Finally, a cut on the measured dimuon mass of  $M_{\mu^+\mu^-} > 3.2 \text{ TeV}$  left no  $t\bar{t}$  background events.

A separate GEANT simulation showed that the rate of mismeasured low- $p_T$  muons (e.g., ones with their tracks straightened by scattering) is small compared to the real high- $p_T$  muon rate. Therefore, the probability of getting two mismeasured high- $p_T$  muons with  $p_T$  balanced to within 300 GeV is wholly negligible.

A potentially serious loss to the  $Z' \rightarrow \mu^+\mu^-$  signal comes from muon-scattering debris that sprays into the muon system, degrading the reconstruction efficiency. This usually affects the first superlayer of the muon system. The average reconstruction efficiency for the high-energy  $Z'$  muons was found to be 85% per muon. the reconstruction efficiency for  $Z' \rightarrow \mu^+\mu^-$  events was raised to 96% by accepting events with at least one well-reconstructed muon plus one muon with sufficient hits in two unaffected superlayers to determine its angle.<sup>92</sup> Since the  $p_T$  of the poorly-reconstructed muon is expected to match

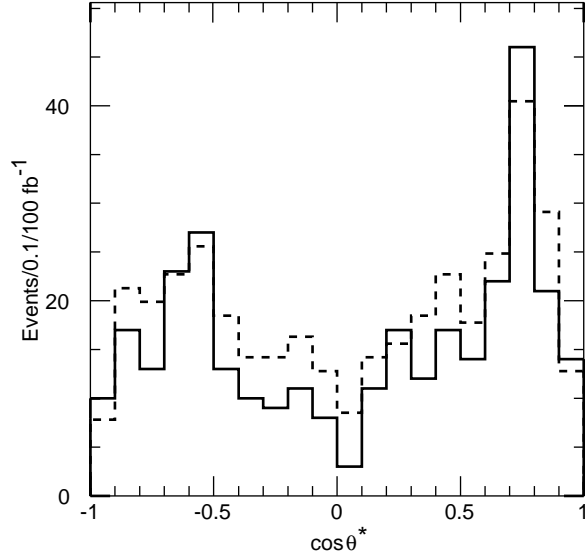


FIG. 56. Generated (dashed) and reconstructed (solid)  $\cos\theta^*$  distributions for  $Z_1 \rightarrow \mu^+\mu^-$  events passing signal selections.

that of the well-reconstructed one to within 300 GeV, its momentum can be determined with sufficient accuracy. If necessary to do so, it is reasonable to assume that the charge of the bad muon is opposite that of the good muon.

In summary, the overall acceptance of the signal (including all produced events) is 60%. There are 350  $Z_1$  and 270  $Z_2 \rightarrow \mu^+\mu^-$  events detected by GEM with  $100\text{fb}^{-1}$  of data. The Drell-Yan dimuon spectrum for the  $Z_2$  model is shown in Fig. 55, which shows all events that had generated invariant mass greater than 1.5 TeV and passed all cuts. For comparison, the distribution of dimuon events from the  $\bar{t}t$  background that passed the isolation cut is also shown. The Drell-Yan spectra for the two models were fit with an exponential plus a Gaussian to determine the masses of the  $Z'$  enhancements. These were found to be  $M_{Z_1} = 4036 \pm 40$  GeV and  $M_{Z_2} = 3968 \pm 65$  GeV. The errors are purely statistical.

The measured  $\cos\theta^*$  distributions for Models 1 and 2 are shown in Figs. 56 and 57. Events in the mass range 3.2–4.8 TeV were used for this analysis. There are 319  $Z_1$  and 257  $Z_2$  events in this sample; the missing events were lost due to momentum smearing. As noted above, only six Drell-Yan background events contaminate this sample. For comparison, the PYTHIA-generated distributions, corresponding to a perfect detector with GEM's  $\eta$ -coverage, are shown in these figures. The agreement between theoretical expectation and simulated measurement is quite good. The forward-backward asymmetry is defined as

$$A_{FB} = \frac{N(\cos\theta^* > 0) - N(\cos\theta^* < 0)}{N(\cos\theta^* > 0) + N(\cos\theta^* < 0)}. \quad (5.24)$$

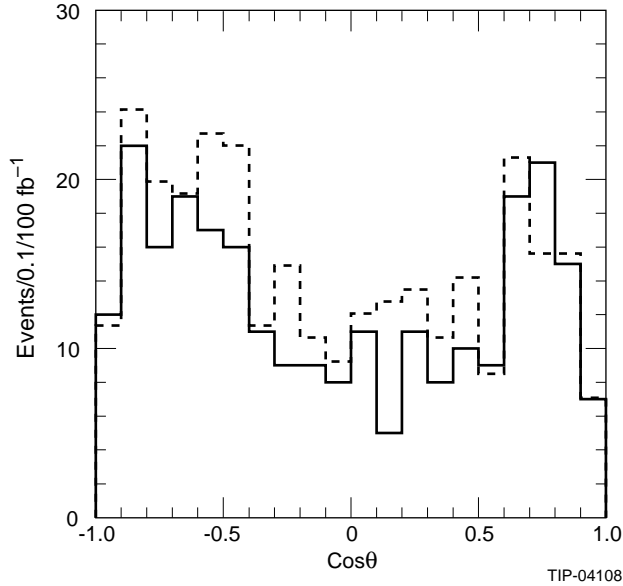


FIG. 57. Generated (dashed) and Reconstructed (solid)  $\cos \theta^*$  distributions for  $Z_2 \rightarrow \mu^+ \mu^-$  events passing signal selections.

The results for the two models are

$$\begin{aligned}
 A_{FB}(Z_1) &= 0.113 \pm 0.056 \quad (\text{GEM}) \\
 &= 0.083 \pm 0.051 \quad (\text{PYTHIA}) \\
 A_{FB}(Z_2) &= -0.090 \pm 0.062 \quad (\text{GEM}) \\
 &= -0.115 \pm 0.058 \quad (\text{PYTHIA})
 \end{aligned}
 \tag{5.25}$$

The PYTHIA and `gemfast` asymmetries agree well within the statistical errors and the central values of the two models are separated by about  $3.5\sigma$ .

### 5.6.2. Studies of Quark-Lepton Substructure in Drell-Yan Processes

The greatest model-independent sensitivity to quark-lepton substructure is obtained by measuring the highest possible dilepton and dijet masses. If a signal is found, the inherent precision of lepton measurement at high energies will make the Drell-Yan process a much more incisive tool than high- $E_T$  jet production for studying substructure. However, as with the  $Z'$ , hundreds of events at very large energies will be required. The contact interactions induced by quark-lepton substructure must be flavor-symmetric if the substructure scale  $\Lambda \lesssim 500$  TeV. Thus, the Drell-Yan processes  $pp \rightarrow \ell^+ \ell^-$  and  $\ell^\pm \nu_\ell$  will have equal cross sections for electrons and muons. Signals in  $pp \rightarrow \mu^+ \mu^-$  are considered here. While it is important to observe the substructure signal in  $pp \rightarrow e^+ e^-$  as well, the  $e^+ e^-$  spectrum cannot help distinguish between models because a difference in rate can be compensated for by a change in  $\Lambda$ . A brief discussion of substructure studies in the  $\mu^\pm \nu_\mu$  channel is presented in Section 5.6.3.

Quark-lepton substructure modifies dimuon production in two ways: an excess of events at high  $M_{\mu^+\mu^-} = \sqrt{\hat{s}}$ <sup>11</sup> and a deviation in the angular distribution of the outgoing  $\mu^-$  relative to the incoming quark.<sup>93</sup> We consider two different chiral forms for the contact interaction  $\mathcal{L}_\Lambda$  arising from substructure at  $\Lambda = 25$  TeV, well beyond that which can be studied at a 40 TeV hadron collider with  $10^{33}$  cm<sup>-2</sup> s<sup>-1</sup>. The goal in this study is to distinguish these two models by their muon angular distribution.

In the first model, only left-handed quarks and leptons are composite and the contact interaction is assumed to be the product of two weak-isoscalar currents (the ‘‘ISO’’ model):

$$\mathcal{L}_{\text{ISO}} = -\frac{4\pi}{\Lambda^2} \bar{Q}_{La} \gamma^\mu Q_{La} \bar{L}_{Lb} \gamma_\mu L_{Lb} , \quad (5.26)$$

where  $Q_{La} = (u_a, d_a)_L$  and  $L_{La} = (\nu_a, \ell_a)_L$  are left-handed quark and lepton fields and  $a, b = 1, 2, 3$  label generations. This interaction, together with the standard Drell-Yan processes, produces the subprocess cross section

$$\frac{d\hat{\sigma}(q_i \bar{q}_i \rightarrow \ell^- \ell^+)}{d(\cos \theta)} = \frac{\pi \alpha^2}{24 \hat{s}} \left[ A_i(\hat{s}) (1 + \cos \theta)^2 + B_i(\hat{s}) (1 - \cos \theta)^2 \right]. \quad (5.27)$$

The functions  $A_i$  and  $B_i$  are given by

$$\begin{aligned} A_i(\hat{s}) = & \left[ \frac{\hat{s}}{\alpha \Lambda^2} + \mathcal{Q}_i + \frac{4}{\sin^2 2\theta_W} (T_{3i} - \mathcal{Q}_i \sin^2 \theta_W) \left( \frac{1}{2} - \sin^2 \theta_W \right) \left( \frac{\hat{s}}{\hat{s} - M_Z^2} \right) \right]^2 \\ & + \left[ \mathcal{Q}_i + \mathcal{Q}_i \tan^2 \theta_W \left( \frac{\hat{s}}{\hat{s} - M_Z^2} \right) \right]^2 ; \end{aligned} \quad (5.28)$$

$$\begin{aligned} B_i(\hat{s}) = & \left[ \mathcal{Q}_i - \frac{1}{\cos^2 \theta_W} (T_{3i} - \mathcal{Q}_i \sin^2 \theta_W) \left( \frac{\hat{s}}{\hat{s} - M_Z^2} \right) \right]^2 \\ & + \left[ \mathcal{Q}_i - \frac{1}{\cos^2 \theta_W} \mathcal{Q}_i \left( \frac{1}{2} - \sin^2 \theta_W \right) \left( \frac{\hat{s}}{\hat{s} - M_Z^2} \right) \right]^2 . \end{aligned}$$

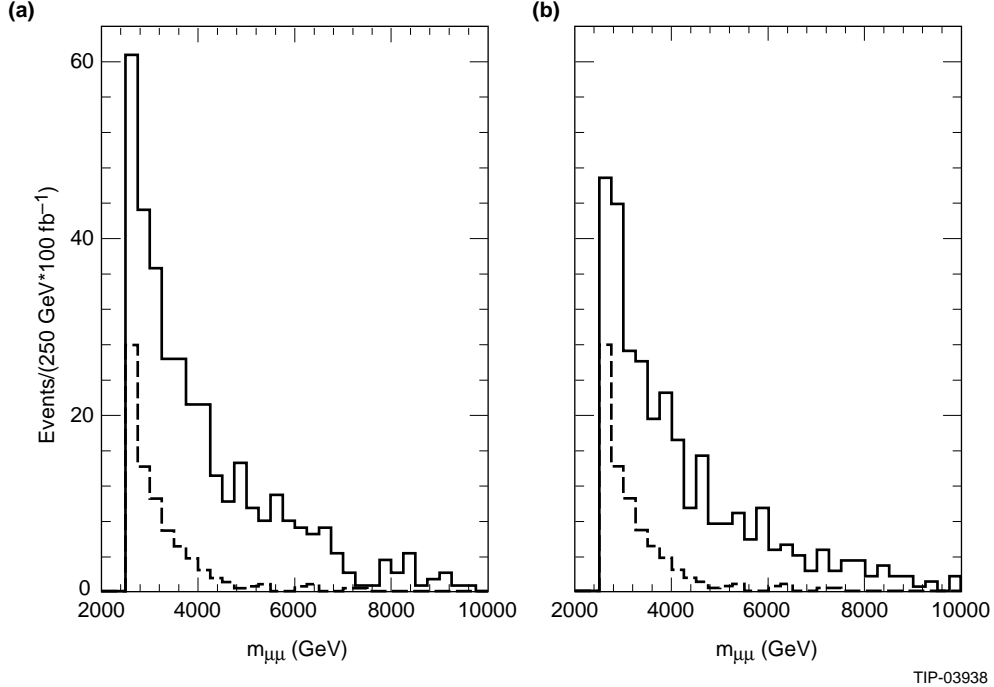
Here,  $\sin^2 \theta_W \cong 0.23$ ,  $(T_{3i}, \mathcal{Q}_i) = (\frac{1}{2}, \frac{2}{3})$  for  $q_i = u_i$  and  $(-\frac{1}{2}, -\frac{1}{3})$  for  $q_i = d_i$ . At high energies,  $\hat{s} > \alpha \Lambda^2$ ,  $A_i(\hat{s}) \simeq (\hat{s}/\alpha \Lambda^2)^2$  and the angular distribution of  $\ell^-$  relative to  $q_i$  is approximately  $(1 + \cos \theta)^2$ .

In the second model the contact interaction is helicity nonconserving (the ‘‘HNC’’ model):

$$\mathcal{L}_{\text{HNC}} = -\frac{4\pi}{\Lambda^2} \epsilon_{ij} \bar{Q}_{Lia} u_{Ra} \bar{L}_{Ljb} \ell_{Rb} + \text{h. c.} , \quad (5.29)$$

where  $i, j = 1, 2$  label indices in an electroweak doublet and  $\epsilon_{12} = -\epsilon_{21} = 1$ . This interaction, while theoretically unlikely, is studied here because it generates an angular distribution that becomes isotropic at large  $\hat{s}$ . The interaction  $\mathcal{L}_{\text{HNC}}$  affects  $u_i \bar{u}_i \rightarrow \ell^- \ell^+$  only:

$$\frac{d\hat{\sigma}(u_i \bar{u}_i \rightarrow \ell^- \ell^+)}{d(\cos \theta)} = \frac{\pi \alpha^2}{24 \hat{s}} \left[ A_u(\hat{s}) (1 + \cos \theta)^2 + B_u(\hat{s}) (1 - \cos \theta)^2 \right] + \frac{\pi \hat{s}}{12 \Lambda^4} . \quad (5.30)$$



TIP-03938

Fig. 58. The  $M_{\mu^+\mu^-}$  distributions for the ISO (a) and HNC (b) substructure models defined in the text. The lower dashed histogram is the standard Drell-Yan distribution.

The contributions of  $\mathcal{L}_{\text{HNC}}$  and  $\gamma/Z^0$  do not interfere because their chiral structures are different.

PYTHIA 5.5 was used to generate 1500 events each of standard Drell-Yan (DY) and DY modified with the ISO and HNC contact interactions with  $\Lambda = 25 \text{ TeV}$ . The muons were required to have generated  $M_{\mu^+\mu^-} > 2 \text{ TeV}$ . The cross sections for events in which both muons have  $|\eta| < 2.46$  are 2.83 fb, 9.44 fb and 7.88 fb for the DY, ISO and HNC cases. Detector response to events was simulated using `gemfast` with Gaussian pileup for  $\mathcal{L} = 10^{34} \text{ cm}^{-2} \text{ s}^{-1}$ . The acceptance was 70% for events with both muons in  $|\eta| < 2.46$ , consistent with the acceptance of  $Z' \rightarrow \mu^+\mu^-$  events. Of these, 99.5% of the standard DY events had the charges of both muons determined. This dropped to 96% for the ISO and HNC models, reflecting the excess of high-energy muons generated by the contact interactions.

The discussion of backgrounds and muon reconstruction is essentially the same as in the analysis of  $Z' \rightarrow \mu^+\mu^-$ . The isolation criterion defined in Eq.(5.23) and the invariant mass cut  $M_{\mu^+\mu^-} > 2.5 \text{ TeV}$  eliminated the physics backgrounds. The acceptance of these two cuts for signal events passing previous selections was 41% for the DY events, 60% for the ISO events, and 66% for HNC. The higher acceptance in the ISO and HNC cases is due to the excess of high-mass dimuons. Retaining those events in which at least the momentum of one muon and the angle of the other are well-measured, the net reconstruction efficiency was found to be 95% for the DY and ISO cases and 92% for the HNC model.

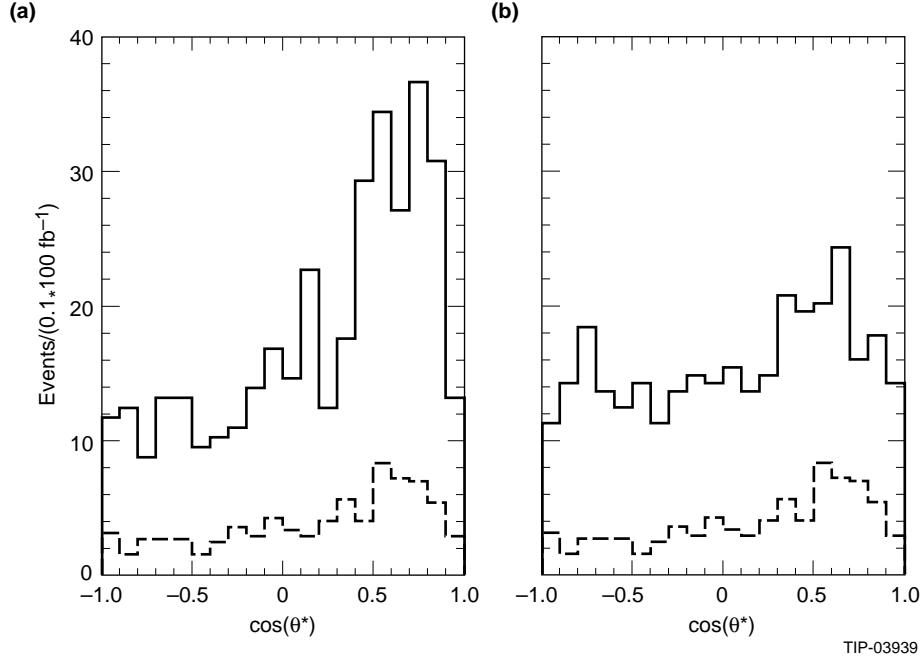


Fig. 59. The  $\cos\theta^*$  distributions for the ISO (a) and HNC (b) substructure models defined in the text. The lower dashed histogram is the standard Drell-Yan distribution.

The net acceptances and number of events per  $100\text{ fb}^{-1}$  are 23% and 80 events for DY, 33% and 360 events for ISO, and 35% and 315 events for HNC. Figure 58 shows the  $M_{\mu^+\mu^-}$  distributions for the ISO and HNC models detected in GEM per  $100\text{ fb}^{-1}$ . Also shown are the underlying DY mass distributions. The muon angular distributions were determined as in the  $Z'$  case. The  $\cos\theta^*$  distribution for the  $\mu^-$  in the ISO model, compared to DY, is shown in Fig. 59 (a) and for the HNC model in Fig. 59 (b). The DY background was not subtracted from the substructure-model distributions in these figures. The tendency for a  $(1 + \cos\theta^*)^2$  distribution in the ISO model and a flat one in the HNC model is clear and the two models are very well separated. The forward-backward asymmetries are

$$\begin{aligned}
 A_{FB}(\text{DY}) &= 0.295 \pm 0.108 \\
 A_{FB}(\text{ISO}) &= 0.328 \pm 0.050 \\
 A_{FB}(\text{HNC}) &= 0.122 \pm 0.056.
 \end{aligned}
 \tag{5.31}$$

The errors are statistical only. Since the HNC and Drell-Yan contributions do not interfere, the Drell-Yan contribution to the asymmetry can be subtracted. This gives  $A_{FB}(\text{HNC}) = 0.065 \pm 0.065$ , consistent with an isotropic distribution.

Finally, we estimate the reach in substructure scale  $\Lambda$  that could be attained with a data sample of  $100\text{ fb}^{-1}$  at  $\sqrt{s} = 40\text{ TeV}$ . We define the reach to be that value of  $\Lambda$  which gives  $5\sigma$  over the Drell-Yan expectation, approximately 125 events. Then, since the subprocess cross sections above go as  $\hat{s}/\Lambda^4$ , it is possible to determine the reach by scaling the numbers of events found above. The reach of a 40 TeV  $pp$  collider estimated in this way is 30 – 35 TeV.

### 5.6.3. High Mass and Luminosity Physics Studies of $\ell^\pm\nu_\ell$ Modes

The range of physics that can be studied at ultrahigh luminosity can be greatly extended by searching for isolated, high- $p_T$  leptons accompanied by large  $\cancel{E}_T \simeq p_T$ . Extensions of the standard gauge group generally involve  $W'$  as well as  $Z'$  bosons. Their mass and couplings can be determined in high-statistics studies of  $W'^\pm \rightarrow e^\pm\nu_e$  and  $\mu^\pm\nu_\mu$ , respectively. With  $\mathcal{L} = 10^{34} \text{ cm}^{-2} \text{ s}^{-1}$  at a 40 TeV collider, it should be possible to carry out high-statistics studies up to  $M_{W'} \simeq 5 \text{ TeV}$  and to reach as high as 10 TeV. If contact interactions reflecting an underlying quark-lepton substructure exist, they may involve terms of the form  $\bar{u}d\bar{\ell}\nu$  and its conjugate. Much can be learned about the chiral coupling of such interactions by comparing the rapidity distributions of the outgoing  $\mu^+$  and  $\mu^-$ . High-statistics studies should again be possible up to  $\Lambda \simeq 25 \text{ TeV}$ . This section contains a brief description of the measurements that can be made at  $\mathcal{L} = 10^{34} \text{ cm}^{-2} \text{ s}^{-1}$  if this new physics exists.

Precise determination of the mass of a  $W'$ -boson should be possible by measuring the  $p_T$  distribution of the electron in  $pp \rightarrow W' \rightarrow e\nu_e$ . The main issue is how well the Jacobian peak determines  $M_{W'}$ . For high  $M_{W'}$ , there are no significant physics backgrounds. For example, the background jet +  $Z^0$  where the jet fakes an electron and  $Z^0 \rightarrow (\rightarrow \bar{\nu}\nu)$ , is removed by the jet rejection  $\mathcal{R}(e/\text{jet}) \simeq 3 \times 10^{-4}$ . The detector-related issues are much the same as in the  $Z' \rightarrow e^+e^-$  study, except that high precision is not as important here as the resolution on  $\cancel{E}_T \gtrsim 1 \text{ TeV}$ .

Information on the  $W'$  couplings to quarks and leptons can be obtained by measuring the angular ( $\theta$ ) distribution in  $W'^\pm \rightarrow \mu^\pm\nu_\mu$  decay. The  $\theta$ -distribution of  $\mu^-$  relative to the incoming  $d$ -quark will be the same as that of  $\mu^+$  relative to the incoming  $\bar{d}$ . Thus, increased statistics can be obtained by adding data from both modes. These angular distributions provide the only way in  $pp$  colliders to detect the presence of right-handed neutrinos in the decay of  $W'$  bosons. To measure them, one proceeds as follows: (1) Select events with  $p_T(\mu)$  “near” the Jacobian peak found in  $W' \rightarrow e\nu_e$  and having balancing  $\cancel{E}_T$ . This enhances the signal relative to any Drell-Yan continuum or other background. (2) Measure the muon rapidity  $\eta_\mu$ . (3) Determine the neutrino rapidity,  $\eta_\nu$ , by reconstructing the  $W'$ . For this, assume  $\vec{p}_T(\nu) = -\vec{p}_T(\mu)$ . As noted, this is a good approximation for multi-TeV  $W'$  bosons since  $p_T(W') \lesssim 200 \text{ GeV}$  about 70% of the time for  $M_{W'} \gtrsim 2 \text{ TeV}$ . The neutrino 4-momentum and  $\eta_\nu$  are determined up to a quadratic ambiguity by imposing the  $W'$  mass constraint. One can either select the value that minimizes  $\eta_{W'} = \eta_B$  or accept each event twice. The analysis of the muon angular ( $\cos\theta^*$ ) distribution can now be carried exactly as was done for  $Z'$  and  $\bar{q}q \rightarrow \mu^+\mu^-$ . Requiring good hits in all three muon superlayers, the fake high- $p_T$  background to the  $W' \rightarrow \mu + \cancel{E}_T$  signal was found to be negligible.

Contact interactions of the form  $\bar{u}d\bar{\ell}\nu$  give an excess of muons at high- $p_T$ . Even though the parton c.m. frame cannot be found in this case, it is still possible to obtain information on the chiral nature of the contact interaction by comparing the rapidity distributions,  $|\eta_{\mu^+}|$

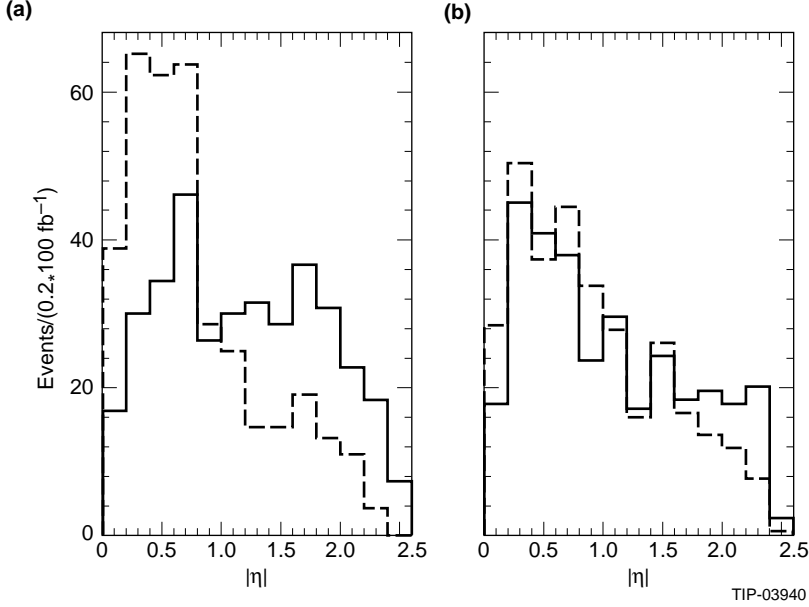


Fig. 60.  $|\eta_{\mu^-}|$  (solid) and  $|\eta_{\mu^+}|$  (dashed) distributions for the ISO (a) and HNC (b) compositeness models defined in the text.

and  $|\eta_{\mu^-}|$  of muons with  $p_T \gtrsim 1.5$  TeV. If, for example, the angular distribution between the incoming  $d$ -quark and the outgoing  $\mu^-$  is  $(1 + \cos\theta)^2$  in the parton c.m. frame, then  $|\eta_{\mu^-}|$  is pushed to larger values because the  $d$ -quark is harder than the  $\bar{u}$ -quark and the  $\mu^-$  tends to be produced forward. Correspondingly, the  $|\eta_{\mu^+}|$  distribution is squeezed to smaller values. If the angular distribution is flat, as in the HNC model, the two rapidity distributions will be identical. These features are illustrated for the ISO and HNC models in Figs. 60. These plots were made for the surviving dimuon event samples of Section 5.6.2. The two models are well separated by the muons' rapidity distributions. If quarks and leptons are composite structures, with a characteristic interaction scale in reach of hadron supercolliders, it is clear that measurements of the angular distributions in both  $\mu^+\mu^-$  and  $\mu^\pm\nu$  channels will be important for pinning down the chiral structure of the contact interaction.

## 6. CONCLUSIONS

In this article we have presented simulations of the GEM detector’s response for a selection of electroweak, flavor, and new gauge-interaction physics processes. The physics examples studied were chosen for their ability to help quantify GEM’s capabilities for new physics and to aid in the detector’s design and optimization, as well as for their intrinsic physics interest. While the examples form a fairly broad range of new physics within and beyond the standard model, they certainly do not represent a full survey of the interesting possibilities.

The principal tool used for these studies was the GEANT-based parameterization of the GEM detector known as `gemfast`. Although there were a few instances when there was no efficient substitute for full GEANT simulations of the response of limited portions of the detector — most notably in the calorimeter studies of jet backgrounds to  $H^0 \rightarrow \gamma\gamma$  — the `gemfast` package was essential for our being able to carry out as broad a range of detailed simulations as we did in a fairly limited amount of time. We firmly believe it is necessary that the range of physics topics studied be as broad as possible. So long as the physics of the TeV-energy regime remains obscure, detectors built to explore it must have the capability to find whatever is going on within reach of their colliders. Thus, we believe that other large collider detector collaborations will profit from the development of similar tools for their large-scale simulation studies.

Had the GEM project proceeded, further studies, both in depth and in breadth, would have been performed and an improved set of tools for modeling the detector developed. These in turn would have further influenced the evolution of the experiment. This iteration between design and physics simulation is an essential part of the creation of any modern detector. The simulations which were carried out guided the design of GEM and influenced a number of major technical choices. Examples are:

- The requirements for the energy resolution of the electromagnetic calorimeter — both for the stochastic ( $\sim 7\%/\sqrt{E}$ ) and the constant ( $\leq 0.4\%$ ) terms — were set by the discovery potential for  $H^0 \rightarrow \gamma\gamma$ ,  $H^0 \rightarrow ZZ^* \rightarrow e^+e^-e^+e^-$ , and  $Z' \rightarrow e^+e^-$ .
- The pointing capability and angular resolution of the electromagnetic calorimeter ( $((40 - 50 \text{ mrad})/\sqrt{E(\text{GeV})} + 0.5 \text{ mrad})$ ) were also motivated by the need to cleanly identify and measure  $H^0 \rightarrow \gamma\gamma$  and  $Z' \rightarrow e^+e^-$ . The pointing ability of the calorimeter complements the central tracker’s determination of the event vertex, making robust GEM’s precise invariant mass resolution for particles decaying into photons and electrons.
- The segmentations of the calorimeter systems were dictated by the need to measure EM processes with high precision and the need to reject hadronic backgrounds. The calorimeter and the tracker combine to provide clean isolation for photons, electrons and muons.

- The precise momentum resolution of the muon system is needed to detect  $Z' \rightarrow \mu^+\mu^-$  and  $H^0 \rightarrow ZZ^* \rightarrow \mu^+\mu^-\mu^+\mu^-$  decays with high efficiency.
- The resolution of the compact central tracker permits the complementary search for supersymmetry in the  $\tilde{g}\tilde{g} \rightarrow \ell^\pm\ell^\pm + X$  channel.
- The rapidity coverage of the forward calorimeters, extending to  $|\eta| \simeq 5.0$ , was dictated by the need to suppress backgrounds to the  $\cancel{E}_T$  signatures for  $H^0 \rightarrow \ell^+\ell^-\bar{\nu}\nu$  decays and for supersymmetry signals.
- An adequate shielding system was designed to suppress neutron and photon backgrounds in the muon chambers, even at  $\mathcal{L} \simeq 10^{34} \text{ cm}^{-2} \text{ s}^{-1}$ .

While the simulation process was by no means complete, the results presented here demonstrate that GEM could have done outstanding physics at the SSC. We can only hope that others will have the opportunity to explore this physics elsewhere.

## ACKNOWLEDGMENTS

The results summarized here represent the hard work of a large and dedicated group of our GEM colleagues: Melynda Brooks, Jim Brau, Rob Carey, Peter Dingus, Yuri Efremenko, Yuri Fisyak, Geoff Forden, Ray Frey, Mitch Golden, Yuri Kamyshkov, Mikhail Leltchouk, Hong Ma, Ken McFarlane, Shawn McKee, Roger McNeil, Geoff Mills, Mohammad Mohammadi, Steve Mrenna, Harvey Newman, Fred Olness, Sasha Savin, Irwin Sheer, Sergei Shevchenko, Xiaorong Shi, Mike Shupe, Kostya Shmakov, Liz Simmons, Jenny Thomas, Henk Uijterwaal, Sasha Vanyashin, Torre Wenaus, David Worrick, Hiro Yamamoto, Chiaki Yanagisawa, Yanlin Ye, Bing Zhou, and Ren-yuan Zhu. We also acknowledge the contributions to the experiment made by the whole GEM collaboration under the leadership of the spokesmen, Barry Barish and Bill Willis. Finally, we would like to thank Holly Durden and the SSCL technical staff for their help in the preparation of the GEM *Technical Design Report*, from which many of the plots presented here are drawn.

K.D.L. was supported in part by the U.S. Department of Energy under Grant No. DE-FG02-91ER40676 and by the Texas National Research Laboratory Commission under Grant Nos. RGFY91-B6, RGFY92-B6, and RGFY93-278. F.E.P. was supported in part by the U.S. Department of Energy under Contract DE-AC02-76CH00016. T.S. was supported in part the U.S. Department of Energy under Contract DE-FG05-92ER40722. T.S. also thanks the Outstanding Junior Investigator program of DOE and the SSC Fellowship program of Texas National Research Laboratory Commission. Fermilab is operated by the Universities Research Association Inc. for the U.S. Department of Energy.

## REFERENCES

1. S. L. Glashow, Nucl. Phys. **22**, 579 (1961);  
S. Weinberg, Phys. Rev. Lett. **19**, 1264 (1967);  
A. Salam, in Proceedings of the 8th Nobel Symposium on Elementary Particle Theory, Relativistic Groups and Analyticity, edited by N. Svartholm (Almqvist and Wiksells, Stockholm, 1968), p. 367;  
H. Fritzsch, M. Gell-Mann, H. Leutwyler, Phys. Lett. **47B**, 365, (1973);  
D. Gross and F. Wilczek, Phys. Rev. Lett. **30**, 1343 (1973);  
H. D. Politzer, Phys. Rev. Lett. **30**, 1346 (1973).
2. R. Cahn and G. Goldhaber, *The Experimental Foundations of Particle Physics*, (Cambridge University Press, 1989)
3. J. J. Aubert, et al., Phys. Rev. Lett. **33**, 1404 (1974);  
J. E. Augustin, et al., Phys. Rev. Lett. **33**, 1406 (1974);  
G. Goldhaber, et al., Phys. Rev. Lett. **37**, 255 (1976).
4. M. L. Perl et al., Phys. Rev. Lett. **35**, 1489 (1975);  
S. W. Herb et al., Phys. Rev. Lett. **39**, 252 (1977)
5. G. Arnison, et al., Phys. Lett. **122B**, 103 (1983);  
M. Banner, et al., Phys. Lett. **122B**, 476 (1983);  
P. Bagnaia, et al., Phys. Lett. **129B**, 130 (1983).
6. For a recent review, see P. Langacker, M. -X. Luo and A. K. Mann, Rev. Mod. Phys. **64**, 87 (1992).
7. F. Abe, et al., The CDF Collaboration, Phys. Rev. Lett. **73**, 225 (1994); Phys. Rev. **D50**, 2966, (1994).  
At the time much of this work was done, the experimental bound was  $m_t > 95$  GeV.
8. There is little doubt that  $\nu_\tau$  exists and that it and the  $\tau^-$  form a standard lepton doublet. The 95% limit on its mass is  $m_{\nu_\tau} < 35$  MeV. See Ref. 9.
9. Particle Data Group, K. Hikasa et al., Phys. Rev. **D50**, No. 3-I (1994).
10. P. W. Anderson, Phys. Rev. **110**, 827 (1958); *ibid.*, **130**, 439 (1963);  
Y. Nambu, Phys. Rev. **117**, 648 (1959);  
J. Schwinger, Phys. Rev. **125**, 397 (1962);  
P. Higgs, Phys. Rev. Lett. **12**, 132 (1964);  
F. Englert and R. Brout, Phys. Rev. Lett. **13**, 321 (1964);  
G. S. Guralnik, C. R. Hagen and T. W. B. Kibble, Phys. Rev. Lett. **13**, 585 (1964).
11. E. Eichten, I. Hinchliffe, K. Lane and C. Quigg, Rev. Mod. Phys. **56**, 579 (1984).
12. K. G. Wilson, unpublished; quoted in L. Susskind, Phys. Rev. **D20**, 2619 (1979);  
G. 'tHooft, in *Recent Developments in Gauge Theories*, edited by G. 'tHooft, et al. (Plenum, New York, 1980).

13. S. Dimopoulos and H. Georgi, Nucl. Phys. **B193**, 153 (1981);  
A.H. Chamseddine, R. Arnowitt and P. Nath, Phys. Rev. Lett. **49**, 970 (1982);  
L. J. Hall, J. Lykken and S. Weinberg, Phys. Rev. **D27**, 2359 (1983).
14. For reviews of supersymmetry and its phenomenology, see H. E. Haber and G. L. Kane,  
Phys. Rept. **117**, 75 (1985);  
S. Dawson, E. Eichten and C. Quigg, Phys. Rev. **D31**, 1581 (1985).
15. See, for example, R. Dashen and H. Neuberger, Phys. Rev. Lett. **50**, 1897 (1983);  
J. Kuti, L. Lin and Y. Shen, Phys. Rev. Lett. **61**, 678 (1988);  
A. Hasenfratz, et al. Phys. Lett. **B199**, 531 (1987);  
G. Bhanot and K. Bitar, Phys. Rev. Lett. **61**, 798 (1988).
16. This is not a pressing issue in the popular “minimal supersymmetric standard model”  
because the Higgs masses are relatively low and, so, the cutoff  $\Lambda$  may be very high  
indeed.
17. S. Weinberg, Phys. Rev. **D13**, 974 (1976); *ibid* **D19**, 1277 (1979);  
L. Susskind, Phys. Rev. **D20**, 2619 (1979);  
S. Dimopoulos and L. Susskind, Nucl. Phys. **B155**, 237 (1979);  
E. Eichten and K. Lane, Phys. Lett. **90B**, 125 (1980).
18. E. Eichten and K. Lane in Ref. 17;  
J. Ellis, M. Gaillard, D. Nanopoulos and P. Sikivie, Nucl. Phys. **B182**, 529 (1981).
19. B. Holdom, Phys. Rev. **D24**, 1441 (1981); Phys. Lett. **B150**, 301 (1985);  
T. Appelquist, D. Karabali and L. C. R. Wijewardhana, Phys. Rev. Lett. **57**, 957  
(1986);  
T. Appelquist and L. C. R. Wijewardhana, Phys. Rev. **D36**, 568 (1987) ;  
K. Yamawaki, M. Bando and K. Matumoto, Phys. Rev. Lett. **56**, 1335 (1986) ;  
T. Akiba and T. Yanagida, Phys. Lett. **B169**, 432 (1986).
20. T. Appelquist, T. Takeuchi, M. B. Einhorn, L. C. R. Wijewardhana, Phys. Lett. **B220**,  
223 (1989); T. Takeuchi, Phys. Rev. **D40**, 2697 (1989) ;  
V. A. Miransky and K. Yamawaki, Mod. Phys. Lett. **A4**, 129 (1989) ;  
R. S. Chivukula, A. G. Cohen and K. Lane, Nucl. Phys. **B343**, 554 ( 1990).
21. See G. 'tHooft in Ref. 12.
22. GEM Collaboration, *Technical Design Report*, SSCL-SR-1219(1993).
23. J. Bagger, et al., FERMILAB-PUB-93-040-T, June 1993.
24. R. Brun et al., GEANT Users' Guide, CERN/DD/78/2; GEANT2 Users' Guide,  
CERN/DD/EE/83/1; GEANT3 Users' Guide, CERN/DD/EE/84-1, Rev. 1987;  
K. Lassila, CERN/CN/91/13.
25. T. A. Gabriel, et al., ORNL/TM-5619, 1977, ORNL/TM-11185 (1983); also IEEE  
Trans. Nuc. Sci. **36**, 14 (1989).

26. G. Marchesini, et al., *Comput. Phys. Commun.* **67**, 465 (1992).
27. F. E. Paige and S. D. Protopopescu, BNL-38774 (1986).
28. H. -U. Bengtsson and T. Sjostrand, *Comp. Phys. Commun.* **46**, 43 (1987).
29. G. Altarelli and G. Parisi, *Nucl. Phys.* **B126**, 298 (1977).
30. By F. A. Berends, H. Kuijf, B. Tausk, and W. T. Giele, *Nucl. Phys.* **B357**, 32 (1991).
31. I. Hinchliffe, LBL-34372, (1993).
32. H. Fesefeldt, PITHA-86/05 (1986)
33. K. Hanssger, et al., KMU-HEP-80-07 (Leipzig U., 1980); K. Hanssger and J. Ranft, *Comp. Phys. Commun.* **39**, 37 (1986).
34. P. Aarnio, et al., FLUKA Users' Guide, CERN-TIS-RP-168 (1986), CERN-TIS-RP-190 (1987).
35. C. Zeitnitz and T. A. Gabriel, 'The GEANT-CALOR Interface,' in *Proc. of 3rd Int. Conf. on Calorimetry for High Energy Physics*, Corpus Christi, 1992.
36. S. N. Cramer, *Applications Guide to the MORSE Monte Carlo code*, ORNL/TM-9355, 1985.
37. W. R. Nelson, et al., *The EGS4 Code System*, SLAC-265 (1985).
38. Yu. Fisyak, K. McFarlane and L. Roberts *SIGEM — Full GEANT Simulation for the GEM Detector*, GEM-TN-92-162 (1992).
39. I. Sheer, *GEMGEN — A Generic Monte Carlo Generator Interface Package*, GEM TN-93-379 (March 1993).
40. G. Grindhammer, et al., *Proc. of the Workshop on Calorimetry for the Supercollider*, Tuscaloosa, AL, 1989, p.151, SLAC-PUB-5072, 1989 and *Nucl. Inst. and Meth.* **A290**, 469 (1990).
41. A. Vanyashin, GEM TN-93-375 (1993).
42. K. Borras, et al., The H1 Calorimeter Group, *Study of Software Compensation for Single Particles and Jets in the H1 Calorimeter*, Contributed paper to the XXV International Conference on High Energy Physics, Singapore, 1990.
43. Yu. Efremenko, et al., *Simulation Studies for GEM Scintillating Barrel Design*, GEM TN-93-349 (1993).
44. M. Shupe, private communication.
45. T. Wenaus, *A Detailed Simulation and Performance Parameterization of the GEM Muon Detector*, GEM TN-93-297 (April 1993).
46. *An Expression of Interest to Construct a Major SSC Detector*, SSC EOI-0020 (July 1, 1991).

47. *GEM Letter of Intent*, The GEM Collaboration, GEM TN-92-49, SSCL-SR-1184 (November 30, 1991).
48. *GEM Responses to the December 1991 PAC Report*, GEM TN-92-131, (July 8, 1992).
49. See, for example, L3 Collaboration, *Z. Phys.* **C57**, 355 (1993).
50. *ECFA Aachen Workshop on LEP 200*, CERN 87-08, June 1987; and *LEP 200 Workshop*, CERN, September 1992.
51. S. Mrenna, et al., GEM TN-93-373.
52. For reviews, see H. E. Haber and G. L. Kane, *Phys. Rept.* **117**, 75 (1985); S. Dawson, E. Eichten and C. Quigg, *Phys. Rev.* **D31**, 1581 (1985).
53. P. N. Harriman, A. D. Martin, R. G. Roberts and W. J. Stirling, *Phys. Rev.* **D42**, 798 (1990) and *Phys. Lett.* **B243**, 421 (1990).
54. J. Botts, et al., MSUHEP-92-27, Fermilab-Pub-92/371, FSU-HEP-92-1225 and ISU-NP-92-17 (1992).
55. H. Yamamoto, GEM TN-93-374.
56. W. E. Cleland and A. V. Vanyashin, GEM TN-93-376, (April, 1993).
57. H. Ma and M. Leltchouk, GEM TN-92-257 (December, 1992); GEM TN-93-356 (April, 1993).
58. R. Y. Zhu and H. Yamamoto, GEM TN 92-126 (July, 1992).
59. S. Dawson, *Nucl. Phys.* **B359**, 283 (1991);  
A. Djouadi, M. Spira, and P. Zerwas, *Phys. Lett.* **264B**, 440 (1991);  
S. Dawson and R. Kauffman, *Phys. Rev. Lett.* **68**, 2273 (1992);  
R. Kauffman, *Phys. Rev.* **D45**, 1512 (1992);  
C. P. Yuan, *Phys. Lett.* **283B**, 395 (1992);  
D. Graudenz, M. Spira, and P. Zerwas, *Phys. Rev. Lett.* **70**, 1372 (1993).
60. B. Bailey, J. Owens and J. Ohnemus, *Phys. Rev.* **D46**, 2018 (1992).
61. W.J. Marciano and F. Paige, BNL Preprint, BNL-45805;  
J. F. Gunion, et al., SDC report, SDC-91-00057;  
R. Kleiss, et al., *Phys. Lett.* **B253**, 269 (1991);  
Z. Kunszt, et al., *Phys. Lett.* **B271**, 247 (1991).
62. J. J. van der Bij and E. W. N. Glover, *Phys. Lett.* **B206**, 701 (1988) ;  
E. W. N. Glover and J. J. van der Bij, *Nucl. Phys.* **B321**, 561 (1989).
63. S. Schevchenko, Private communication.
64. S. Dimopoulos, *Nucl. Phys.* **B168**, 69 (1980);  
T. Appelquist and G. Triantaphyllou, *Phys. Rev. Lett.* **69**, 2750 (1992).

65. E. Eichten and K. Lane, Phys. Lett. **327B**, 129 (1994).
66. C. Yanagisawa, *Top-quark Detection in the Multileptons Mode with the GEM Detector*, GEM TN—93—371 (1993).
67. C. Yanagisawa, *Top-quark Detection in the Multijets Mode with the GEM Detector*, GEM TN—93—372 (1993).
68. M. Mohammadi and D. Skrzyniarz, GEM TN—93—363 (1993).
69. K. Lane, *Top-Quark Production and Flavor Physics — The Talk*, to appear in the Proceedings of the 27th International Conference on High Energy Physics, Glasgow, 20-27th July 1994; Boston University Preprint BUHEP—94—25 (1994).
70. P. Nason, S. Dawson and R. K. Ellis, Nucl. Phys. **B303**, 607 (1988);  
W. Beenakker, H. Kuijf, W. L. van Neerven and J. Smith, Phys. Rev. **D40**, 54 (1989);  
E. Laenen, J. Smith and W. L. van Neerven, Nucl. Phys. **B369**, 543 (1992);  
FERMILAB—Pub—93/270—T;  
K. Ellis, *Top-Quark Production Rates in the Standard Model*, invited talk in Session Pa—18 given of the 27th International Conference on High Energy Physics, Glasgow, 20—27th July 1994.
71. K. Lane and M. V. Ramana, Phys. Rev. **D44**, 2678 (1991).
72. Solenoidal Detector Collaboration Technical Design Report, SDC—92—201, SSCL—SR—1215 (1992).
73. R. M. Barnett, R. Cruz, J. F. Gunion and B. Hubbard, Phys. Rev. **D47**, 1048 (1993).
74. M. Mohammadi, Ph. D. Thesis, University of Wisconsin (1987), unpublished.
75. R. Carey, *Jet Studies with the GEM Detector*, GEM—TN—93—377 (1993).
76. E. J. Eichten, K. D. Lane and M. E. Peskin, Phys. Rev. Lett. **50**, 811 (1983).
77. F. Abe et al., The CDF Collaboration, Phys. Rev. Lett. **68**, 1104 (1992); Fermilab—PUB—91/231—E.
78. We are greatly indebted to T. Sjostrand for embedding the quark and lepton composition routines in PYTHIA and for continued help on the event simulations.
79. J. Morfin and W. -K. Tung, Fermilab—Pub—90/74, (1990).
80. S. Mrenna, GEM—TN—501 (1993)
81. R. Arnowitt and P. Nath, Phys. Rev. Lett. **69**, 725 (1992).
82. R. Ross and R. Roberts, Nucl. Phys. **B377**, 571, 1992.
83. H. Baer, F. E. Paige, S. D. Protopopescu and X. Tata, FSU—HEP—930329. Production and decay of  $\tilde{t}$  is not yet included.
84. F. E. Paige and A. Vanyashin, GEM TN—93—376 (1993).

85. F. E. Paige and A. Vanyashin, GEM TN-92-70 (1992).
86. H. Baer, X. Tata and J. Woodside, Phys. Rev. **D45**, 142 (1992).
87. QCD radiative corrections have not been taken into account in these studies. They are likely to increase the Drell-Yan signal rates. Since all the physics backgrounds are very small after event selections are made, higher-order corrections to them are not expected to change our conclusions. The EHLQ-1 distribution functions were used for all simulations in this section.
88. S. McKee and E. H. Simmons,  $Z' \rightarrow e^+e^-$  studies at  $10^{34} \text{ cm}^{-2} \text{ s}^{-1}$  with the GEM Detector, GEM PN-93-6 (1993).
89. The discrepancy between the theoretical widths determined from Eq.(5.20) and those from fitting the PYTHIA distributions corresponds to about a 0.5% Gaussian noise term that we have not yet understood. Since PYTHIA and `gemfast` widths agree within the expected detector resolution, this is not a matter of immediate concern.
90. P. Langacker, R. Robinett and J. Rosner, Proceedings of the 1984 Summer Study on the Design and Utilization of the Superconducting Super Collider, R. Donaldson and J. G. Morfin, editors; 812 (1984)
91. M. Mohammadi and W. Orrick,  $Z' \rightarrow \mu^+\mu^-$  at Ultrahigh Luminosity with the GEM Detector, GEM TN-93-364 (1993).
92. T. Wenaus, *A Reconstruction Program for the GEM Muon Detector*, GEM TN-93-388 (1993).
93. R. S. Chivukula and L. Randall, Phys. Lett. **202B**, 429 (1988).

This figure "fig1-1.png" is available in "png" format from:

<http://arxiv.org/ps/hep-ph/9412280v1>

This figure "fig2-1.png" is available in "png" format from:

<http://arxiv.org/ps/hep-ph/9412280v1>

This figure "fig3-1.png" is available in "png" format from:

<http://arxiv.org/ps/hep-ph/9412280v1>

This figure "fig4-1.png" is available in "png" format from:

<http://arxiv.org/ps/hep-ph/9412280v1>

